ON THE DYNAMICS

OF

MONSOON DISTURBANCES

by

JAGADISH SHUKLA

SUBMITTED IN PARTIAL FULFILLMENT OF THE

REQUIREMENTS FOR THE DEGREE OF DOCTOR OF SCIENCE

at the

MASSACHUSETTS INSTITUTE OF TECHNOLOGY

January 1976

Signature of Author__________________________________

Department of Meteorology, January 1976

Certified by__________________________________

Thesis Supervisor

Accepted by__________________________________

Chairman, Departmental Committee on Graduate Students

ON THE DYNAMICS OF MONSOON DISTURBANCES

by

Jagadish Shukla

Submitted to the Department of Meteorology on
12 January, 1976, in partial fulfillment of the
requirements for the degree of Doctor of Science

ABSTRACT

The dynamics of the disturbances due to the instabilities of horizontally and vertically shearing mean monsoon flow have been studied. The necessary conditions for internal jet instability are satisfied, and a barotropic-baroclinic instability analysis of the observed zonal flow has shown that the fastest growing modes are mainly due to the barotropic instability of the upper level flow. The amplitude of the most unstable mode is confined to the barotropically unstable upper tropospheric levels and the primary energy conversion is from the zonal kinetic energy to the eddy kinetic energy. This may explain the occurrence of observed westward moving waves at 200 mb.

In an attempt to explain the formation of the monsoon depressions, the role of the CISK mechanism in conjunction with barotropic-baroclinic instability has been explored.

Instability analysis of vertically shearing zonal flows with prescribed vertical distribution functions for cumulus heating has shown that the horizontal scale, phase speed and structure of the most unstable mode depends upon the choice of the vertical heating distribution function. The horizontal scale of the most unstable mode is larger for those distribution functions that provide heating to the larger vertical depths of the atmosphere.

Instability analysis with the quasi-equilibrium assumption (QEA) of Arakawa and Schubert for parameterization of moist convection has shown that in a quiescent atmosphere the growth rate is a maximum for a perturbation of intermediate scale. The vertically integrated net heating is a maximum for the fastest growing mode. It has been shown that a two-layer model is not adequate for study of CISK with QEA parameterization of moist convection. For a two-layer model, the growth rates are infinite for the perturbations whose horizontal scales are proportional to the Rossby radius of deformation. In the presence of vertical shear, the cloud mass flux, as determined by QEA, becomes inversely proportional to the wavelength of the perturbation and the maximum growth rate occurs for the smallest scales.

A combined CISK-barotropic-baroclinic instability analysis of the observed monsoon flow has been performed using the quasi-equilibrium assumption for the parameterization of moist convection. The structure and energetics of the computed linear perturbations are in good agreement with the structure and energetics of the observed monsoon depressions. The results of this study suggest that CISK may provide the primary driving mechanism for the growth of monsoon depressions.

Thesis Supervisor: Jule G. Charney
Title: Professor of Meteorology

THIS THESIS IS DEDICATED TO THE FOND MEMORY OF MY FATHER,

PANDIT CHANDRASHEKHAR SHUKLA.

ACKNOWLEDGEMENTS

I wish to express my gratitude to Professor Jule G. Charney for his guidance and valuable suggestions throughout the course of this study.

I am also grateful to Professor A. Arakawa for several valuable discussions on his scheme for cumulus parameterization.

I wish to thank Professor H. Stommel for his encouragement and interest in monsoon research.

My sincere thanks to Professor E. Lorenz for the benefit of several useful discussions.

Special thanks are due to Professor N.A. Phillips, with whom I had the opportunity to work during Professor Charney's sabbatical leave.

Several valuable conversations with Professor Eugenia K. de Rivas, Professor R.S. Lindzen, Dr. E. Sarachik and Dr. E. Schneider are gratefully acknowledged.

Many thanks to Dr. A. Bass for his suggestions for improving the syntax of the text and to Mr. V. Krishnamurthy for his general helpfulness.

Thanks are extended to Miss Isabelle Kole for her excellent drafting of the diagrams and to Miss Sandy Congleton for her excellent typing.

Finally, I wish to thank all the friendly people who made the 14th floor such a pleasant place.

TABLE OF CONTENTS

LIST OF FIGURES

Figure | Page

CHAPTER 1. INTRODUCTION

The general circulation of the atmosphere may be imagined as axisymmetric and consisting of a thermally direct Hadley cell in the tropics, a thermally indirect mechanically-driven Ferrell cell in the middle latitudes, and a direct cell in polar regions. This idealized model, with added large-scale baroclinically unstable eddies transporting momentum from tropics to middle latitudes (say, across 30°N), helps to explain the maintenance of the non-decelerating westerlies in middle latitudes. In reality, the Hadley cell is far from being symmetric at any time during the year; westerly winds over the equator are not uncommon. The presence of orographic barriers of varying height and the distribution of land and sea introduce asymmetric mechanical and thermal forcing into the atmosphere. The complexity of the circulation is further compounded by seasonal variations in the distribution of solar heating, which differs in its influence over land and sea. The seasonal fluctuations are more prominent in the eastern hemisphere, as compared to the western hemisphere, due to the preponderance of land area. This is especially so over the Asiatic land mass which contains the highest and most extensive plateau of the world, the Tibetan plateau (general elevation, 4-5 km, and an area of more than one million square km). It is observed that during northern winters a large anticyclone persists over north Asia, and its central area lies over Mongolia and adjoining Siberia where the highest surface pressure observed anywhere on the globe exists (Ananthakrishnan and Ramakrishnan, 1963). The prevailing northeasterly winds in the lower troposphere over India and adjoining areas during winter are referred to as the northeasterly monsoon, or the winter monsoon. It is also observed that during the northern summer an extensive low-pressure area persists between north Africa and east China, and its central area lies over west Pakistan, where the lowest mean surface pressure observed anywhere on the globe exists during June-September. The southeasterly trade winds of the southern hemisphere, which cross the equator under the influence of this thermal forcing due to asymmetric continentality, and turn into southwesterly currents, are referred to as the southwest monsoon. (In its generic sense, the word 'monsoon' was derived from an Arabic word meaning 'season'.) The corresponding season of rainfall over China is referred to as Mei-yu and over Japan as Baiu.

Figure 1.1 shows the cross-sections of mean monthly zonal wind speed and potential temperature for the month of July along 85°E from 20°S to 40°N. The vertical structure of the mean circulation is characterized by lower tropospheric westerlies, which attain a maximum speed of about 15-20 knots at about 850 mb, and upper tropospheric easterlies, which attain a maximum speed of 40-60 knots at about 150 mb. The vertical shear is easterly (the meridional temperature gradient from south to north is negative), and the transition from lower level westerlies to upper level easterlies occurs at about 500 mb. The mean circulation is also characterized by appreciable horizontal shear. At 850 mb, the strongest westerlies occur at 10°N and are flanked by weaker easterlies in the foothills of the Himalayas and relatively stronger easterlies south of the equator.

Figure 1.2 shows the cross-sections of zonal wind and potential temperature along 73°E and 100°E. It may be seen that the vertical struc-

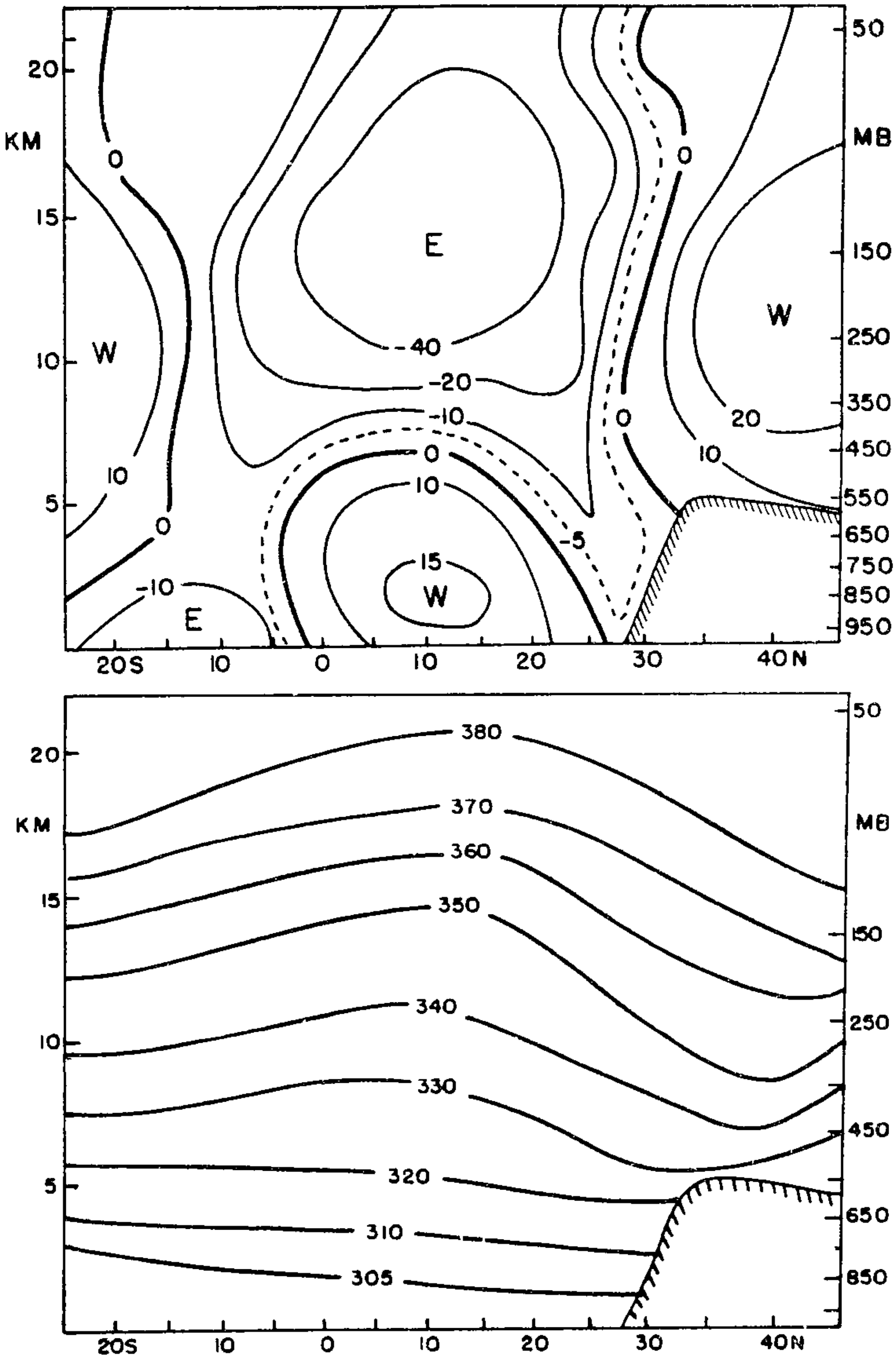

Figure 1.1 Cross-section along 85E for the observed mean July values of (a) zonal wind (knots) and (b) potential temperature (°K).

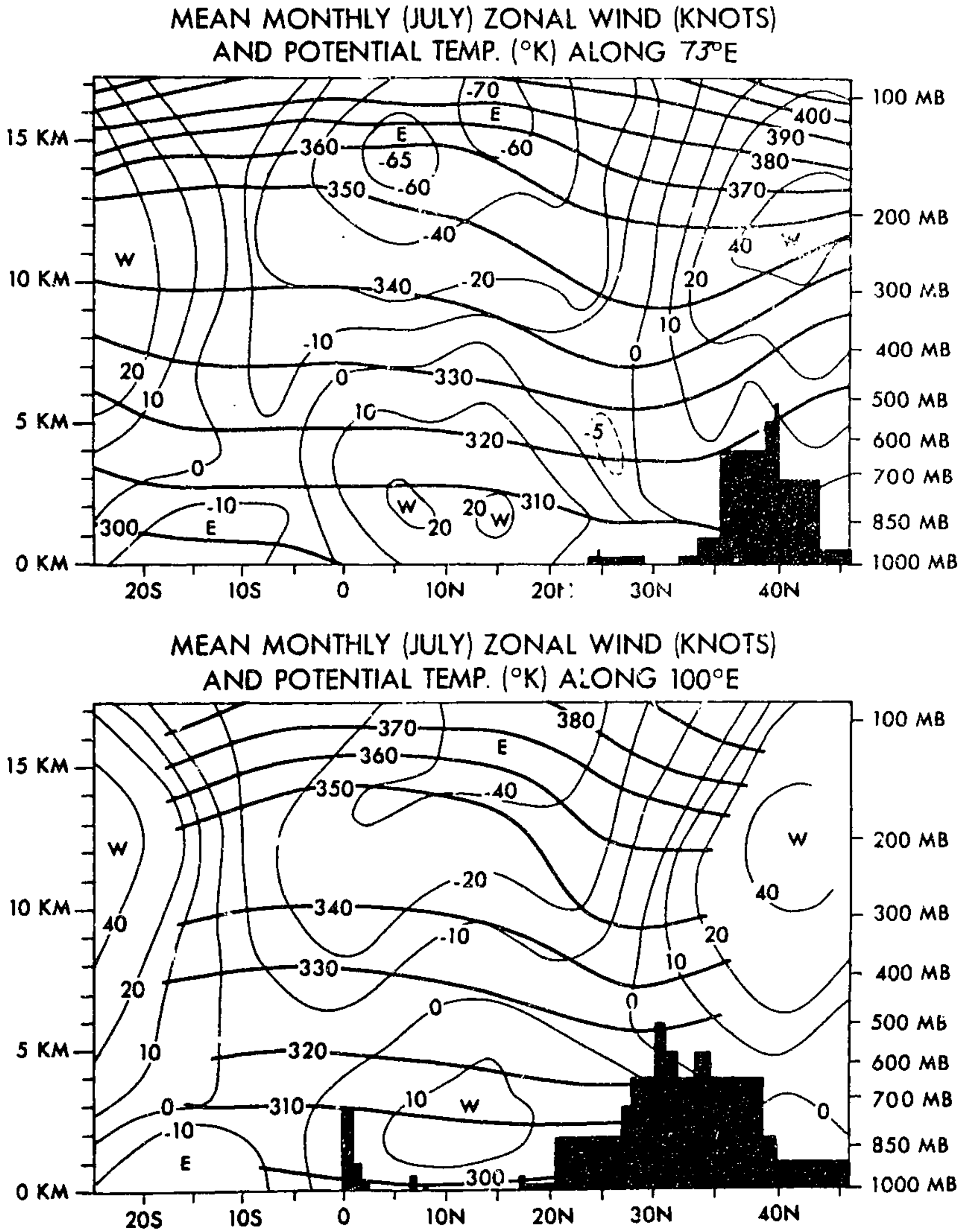

Figure 1.2 Same as Figure 1.1 along 73E and 100E (From: Ramage and Raman, 1972).

ture of the mean circulation is fairly homogeneous between longitudes 73°E and 100°E.

Figure 1.3 shows the vertical structure of temperature and moisture for the mean monsoon atmosphere. Moist static energy decreases from the surface value of 85.0 cal/gm to 81.0 cal/gm at about 3 km. Like the mean tropical atmosphere, the monsoon atmosphere is also conditionally unstable, with large values of mixing ratio in the lowest layers.

The purpose of this thesis is to study the dynamics of the disturbances which may appear due to the instabilities of the mean monsoon circulation. The basic approach will be to investigate the instability mechanisms due to which infintesimal perturbations upon this mean state may grow. Since the mean state is characterized by horizontally and vertically shearing zonal winds, and since monsoon disturbances are accompanied by organized convective activity and precipitation, this work may also be viewed as a general study of the instability of a basic state in which the zonal wind has horizontal and vertical shear, the vertical thermal structure is conditionally unstable, and the moist convective heating is parameterized in terms of the large-scale variables.

It is well known that monsoon depressions are among the most important components of the monsoon circulation. Although the depressions rarely attain hurricane intensity, the rainfall associated with them is quite large and accounts for a major portion of the total monsoon rainfall. However, no systematic study has been made previously to investigate the dynamics of these disturbances and to identify the physical mechanisms and dynamic instabilities which may be responsible for the growth and maintenance of these depressions. So far as is known to the author, this study

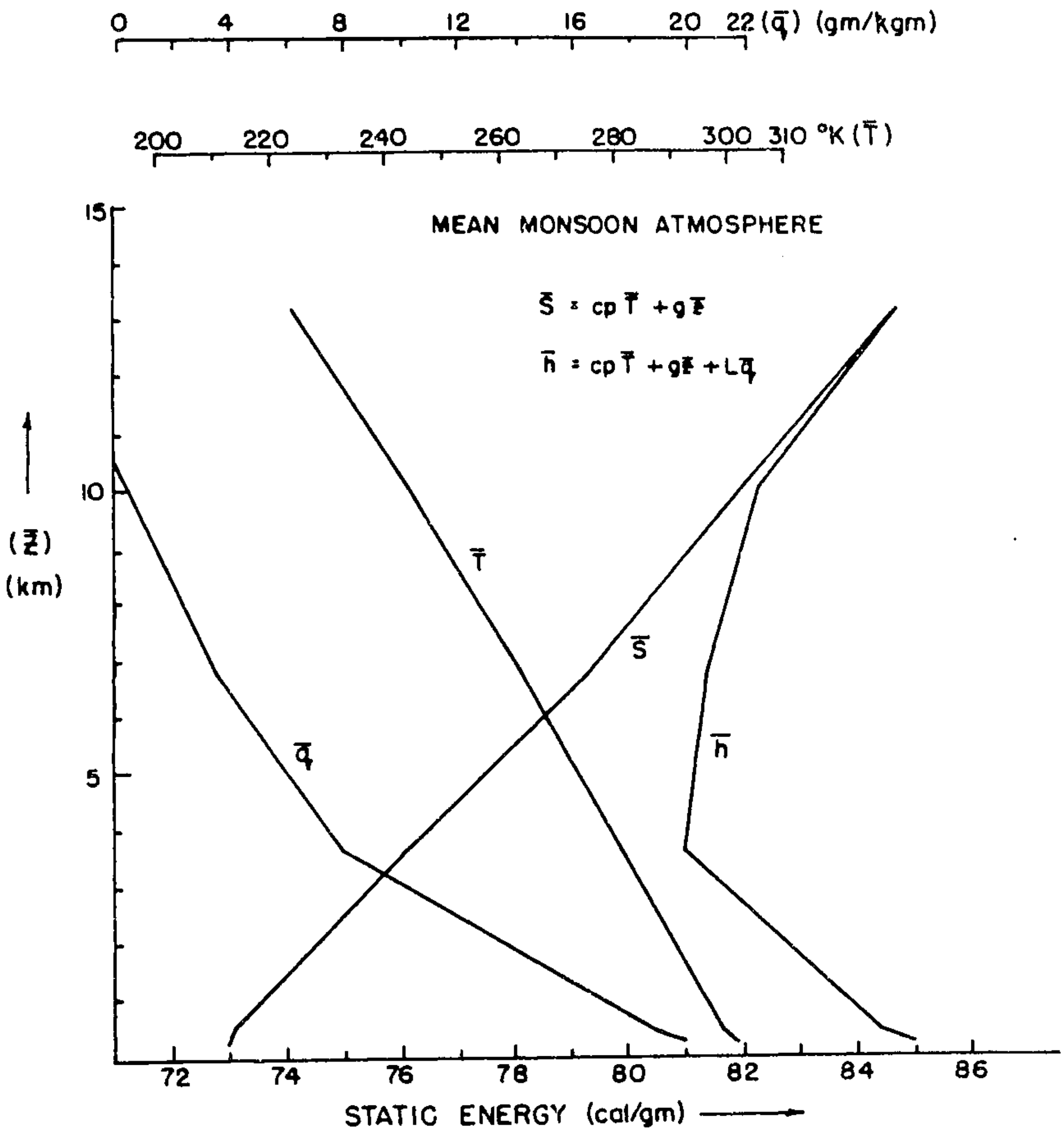

Figure 1.3 Vertical structure of temperature $\bar{T}$, mixing ratio $\bar{q}$, dry static energy $\bar{S}$, and moist static energy $\bar{h}$ for mean monsoon atmosphere.

is the first such attempt in this direction. In particular, the study focuses upon the disturbances observed between longitudes 70°E and 100°E. This is the longitudinal belt of maximum meridional temperature and pressure gradients and substantial cyclogenesis. Although the paucity of data is a general problem for the whole monsoon region, the synoptic network over India provides reasonable data coverage in the longitude belt under consideration.

Figure 1.4 shows a typical synoptic situation in which a monsoon depression is located over northeast India. For the same synoptic situation, Figure 1.5 displays the vertical cross-sections of meridional wind, temperature anomaly, and absolute vorticity, along a zonal plane at 22°N. These figures have been reproduced from a paper by Krishnamurti, et. al (1975), which is perhaps the first documented detailed analysis of the structure of a monsoon depression. In this paper, the authors make the following statement about the structure of the monsoon depressions:

> "The horizontal scale of the depression is about 2,000 km, the vertical scale about 10 km, its westward speed of motion about 5° longitude/day. The monsoon depression is an intense close vortex that has horizontal wind speeds of about 10 to 15 mps and its closed circulation extends to about 9 km in the vertical. . . . The vortex has a very well-defined cold core in the lower troposphere and a warm core above 500 mb. . . . Vertical motions show rising motion west of; i.e., ahead of, the trough line and descending motion to the rear. . . ."

It is not clear why the authors considered the horizontal scale of the monsoon depression to be 2,000 km. We may see from Figure 1.5 (top panel) that the distance between the maxima of northerly and southerly components of the meridional wind is nearly 16 degrees of longitude, which may be considered as one-half wavelength. Therefore, when considering the monsoon depression as an idealized, wave-like perturbation, it seems more

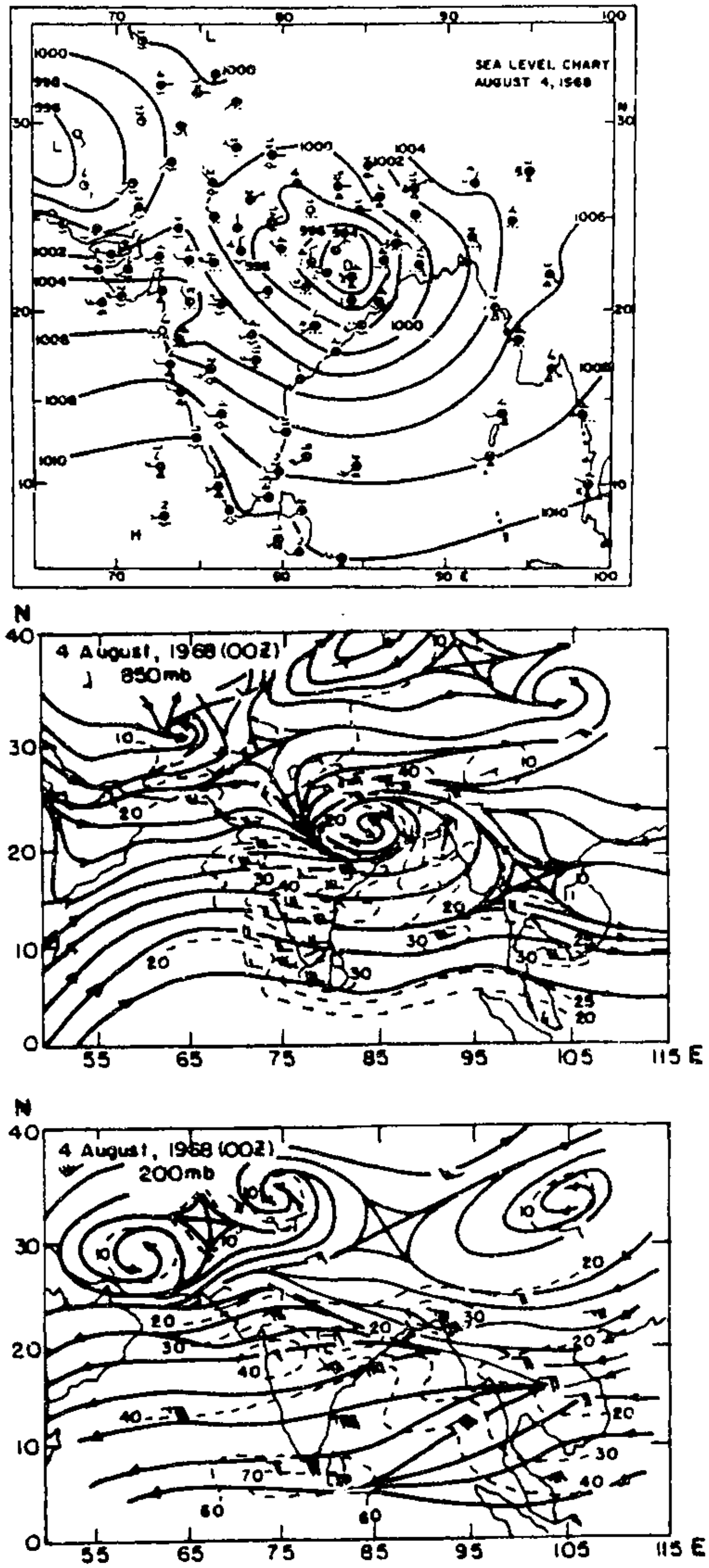

Figure 1.4 (a) Surface pressure map, (b) Motion field at 850 mb, (c) Motion field at 200 mb, for 00Z on 4 August, 1968 (From: Krishnamurti et. al, 1975).

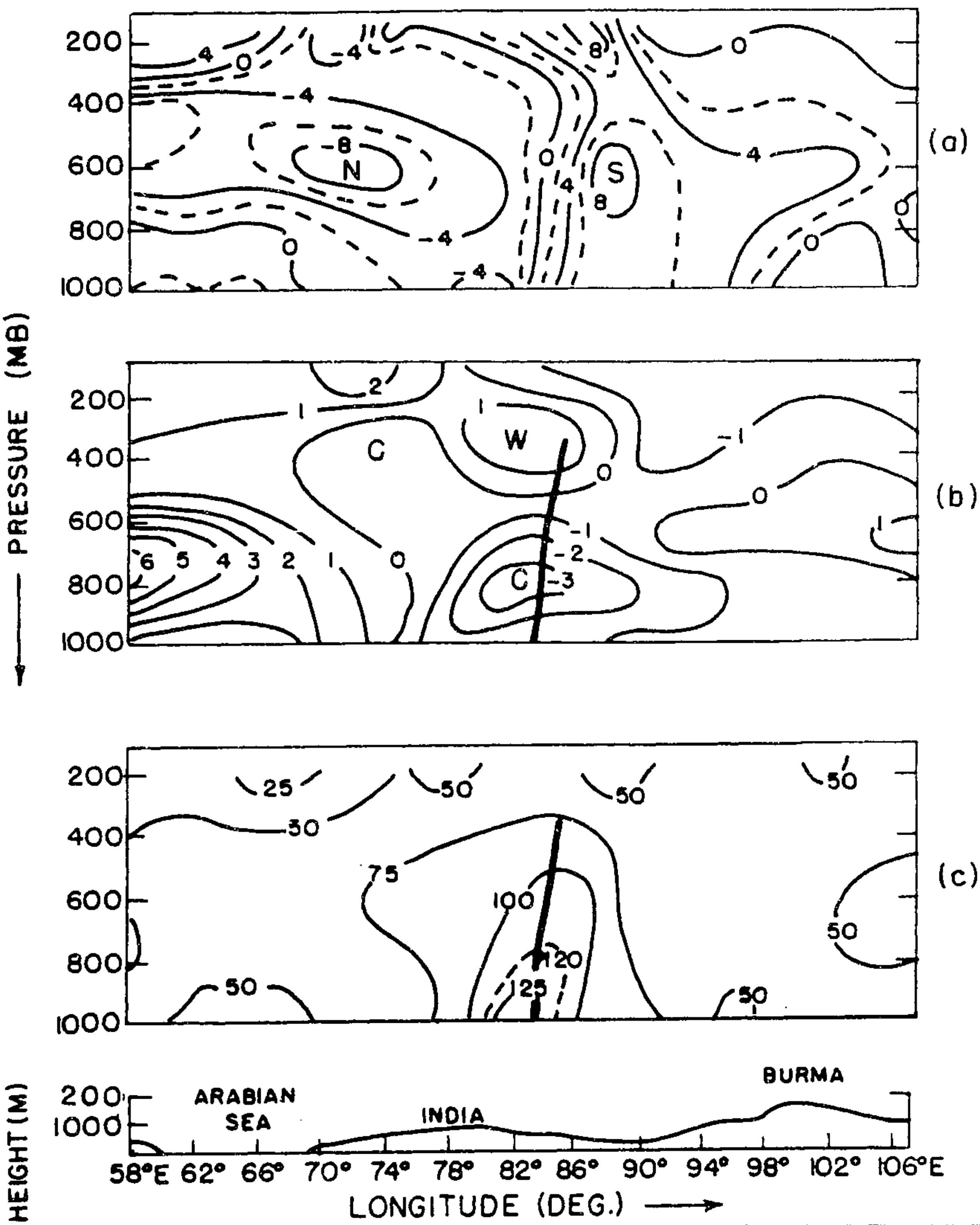

Figure 1.5 Vertical cross-section of (a) meridional wind (m/s), (b) temperature anomaly (°C), (c) absolute vorticity ($10^{-6}s^{-1}$) along 22N (From: Krishnamurti et. al, 1975).

reasonable to take the horizontal wavelength as 3,000 km.

Figure 1.6 shows the tracks of observed monsoon depressions over India in the month of July for the period 1891-1960. The general direction of movement of these disturbances is between west and west-northwest. Their phase speed is typically about 3 m/s. Due to scarcity of observations on the Burma coast, it is not possible to determine whether these disturbances formed over the Bay of Bengal or whether they originated further eastwards. We have examined the daily satellite cloud pictures for the months of June through September for the years 1967-1973 in an attempt to trace the movement of organized cloud clusters from regions east of the Bay of Bengal. Due to extensive monsoon cloudiness in the region, it was not possible to identify, or to trace, the individual clusters, but a subjective visual inspection of daily cloud pictures suggested that most of the disturbances which originated in the Bay of Bengal formed in situ and then moved westwards over the Indian subcontinent. This conclusion is further supported by an earlier study of Ramanna (1967), in which he examined the dates for which a cyclonic system was observed on the China coast, and the dates for which a monsoon depression appeared over the Bay of Bengal. His conclusion was that not more than 15 percent of the monsoon depressions would have developed from the westward moving perturbations which come from the China sea. It seems, therefore, reasonable to assume that most of these disturbances develop over the Bay of Bengal and then move overland. The questions that we would be primarily interested in are: What makes this area so cyclogenetic? Why do the monsoon depressions grow, or why do the weak perturbations which come from the east intensify after moving over this region?

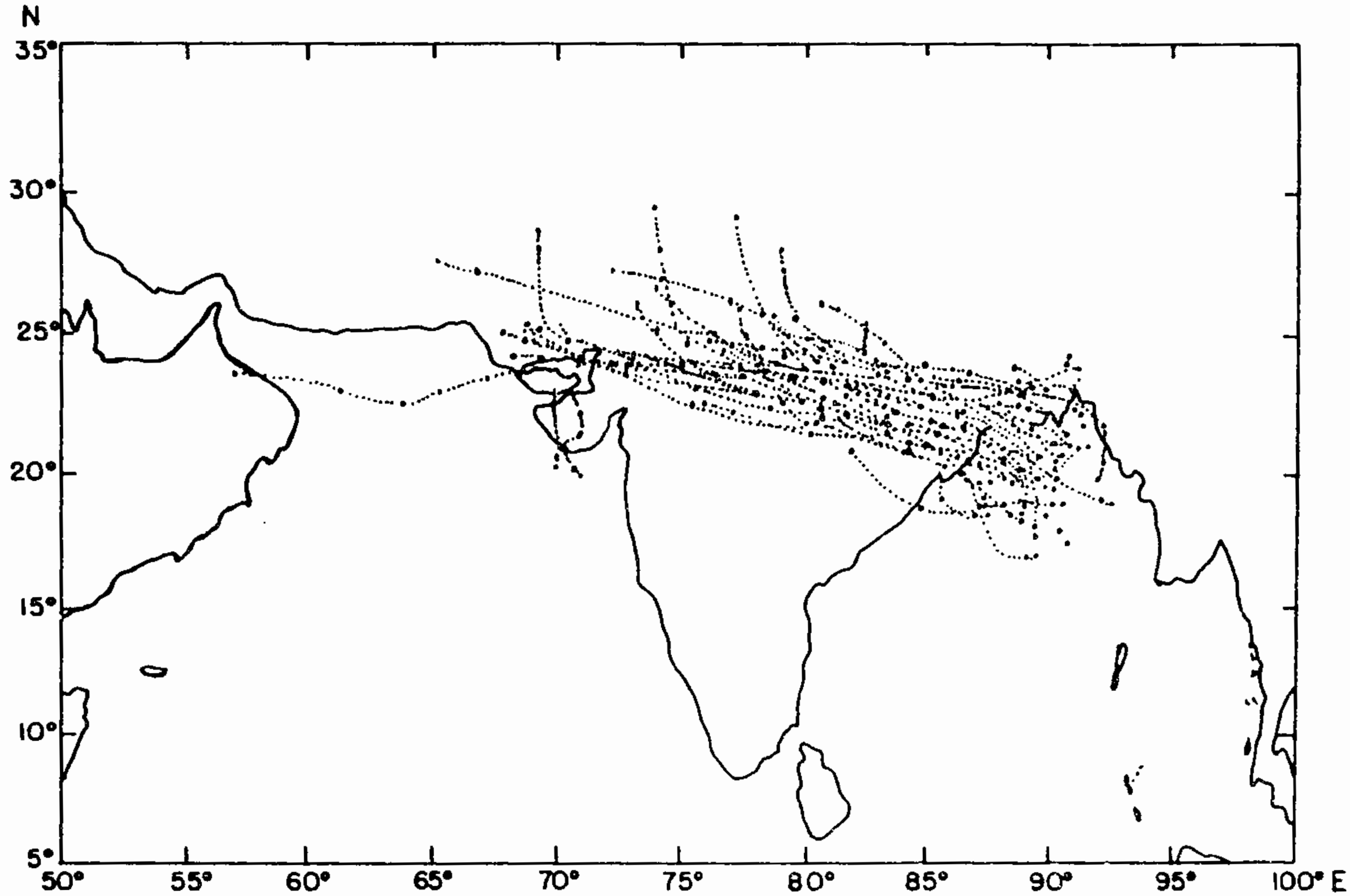

Figure 1.6 Tracks of cyclonic storms during July for 1891-1960 (India Meteorological Department).

Since the mean monsoon zonal flow has appreciable horizontal and vertical shear, it is quite likely that barotropic-baroclinic instability may play a role in the genesis of these disturbances. Since extensive organized moist-convection and large amounts of precipitation are associated with these disturbances, it is quite likely that the CISK mechanism may be important for their growth and maintenance. We shall, therefore, make a systematic analysis of CISK-barotropic-baroclinic instability to understand the physical mechanisms responsible for the growth and maintenance of these disturbances.

One of the unique features of the monsoon disturbances, as distinguished from other tropical disturbances, is that they form sufficiently far from the equator so that the mass and the motion fields are in reasonable geostrophic balance. The spatial scale ($\approx$ 2,000-3,000 km) and the propagation speed ($\approx$ 3 m/s) of these disturbances suggests that a quasi-geostrophic model may be an adequate dynamical framework for their study.

In Chapter 2, we have examined the combined barotropic-baroclinic instability of mean monsoon zonal flow, $\overline{U}(y,p)$, using a ten-layer quasi-geostrophic model. Because $\overline{U}$ is a function of y and p, the problem becomes non-separable, and this is a manifestation of the fact that there are two sources of energy (available kinetic energy and available potential energy). We have, therefore, followed the initial value approach to instability analysis, in which the linearized perturbation equations for a given wavelength are numerically integrated in time for an arbitrary initial condition. The integration is continued until the phase speeds and the growth rates converge to their constant values over the whole computational domain. These are the values of phase speed and growth rate for the most unstable mode. Integrations were performed for a range of wavelengths.

In Chapter 3, we have examined the role of the CISK mechanism for the development of monsoon disturbances. We have parameterized the heating due to cumulus convection in terms of the Ekman pumping at the lowest level and have used empirical profiles for the vertical distribution of heating. We have also experimented with the parameterization of heating in terms of the vertical velocity at the top of the lowest layer. The primary objective of such experimentation is to show that the results are very sensitive to the shape of the empirically chosen vertical distribution function and therefore to emphasize the need for a physical theory from which to deduce a scheme to parameterize heating due to cumulus convection.

In Chapter 4, we have described the quasi-equilibrium assumption of Arakawa and Schubert (1974) which is used in this thesis to parameterize the heating and the moisturizing effects of cumulus ensembles. We have incorporated this scheme within a three-layer quasi-geostrophic model to perform an instability analysis of a conditionally unstable atmosphere with vertical shear. We have also studied a two-layer model and pointed out the inadequacy of two-layer models for the study of the dynamics of disturbances for which moist convection processes are important.

In Chapter 5, we have analyzed the instability of the monsoon zonal flow, $\overline{U}(y,p)$. We have used the initial value approach of Chapter 2 and have applied the parameterization of moist-convection, as described in Chapter 4.

In Chapter 6, we have presented a summary of the study and our principal conclusions.

CHAPTER 2. BAROTROPIC-BAROCLINIC INSTABILITY OF MONSOON FLOW

One of the noteworthy features of the cross-section of the zonal wind along 85°E (see Fig. 1.1) is the presence of a weak easterly wind between the two westerly maxima. Subtraction of a constant U (which is equivalent to a Galilean translation in the zonal direction) would readily show an internal jet. This suggests the possibility of an internal jet instability mechanism (Charney and Stern, 1962) in this region. One of the necessary conditions for this instability is that the gradient of potential vorticity on an isentropic surface should vanish in the region. Figure 2.1 shows the cross-section of potential vorticity along 85°E. It is seen that this necessary condition for instability is satisfied.

We shall first examine the instability properties of the basic flow using the inviscid, adiabatic, quasi-geostrophic system of equations. Since U is a function of y and p, the perturbation equations become non-separable; we shall follow the initial value approach to stability analysis (Brown, 1969). In this approach, the linearized perturbation equations of the model are numerically integrated in time with an initial arbitrary perturbation of given wavelength. The integration is continued until the phase speed and the growth rate (as determined by (2.6) and (2.5)) converge to constant values over all points of the computational grid. Such integrations are repeated for several values of wavelength in order to find the wavelength for which the growth rate is a maximum.

2.1 The Mathematical Model

The linearized form of the vorticity and thermal equations may be written as:

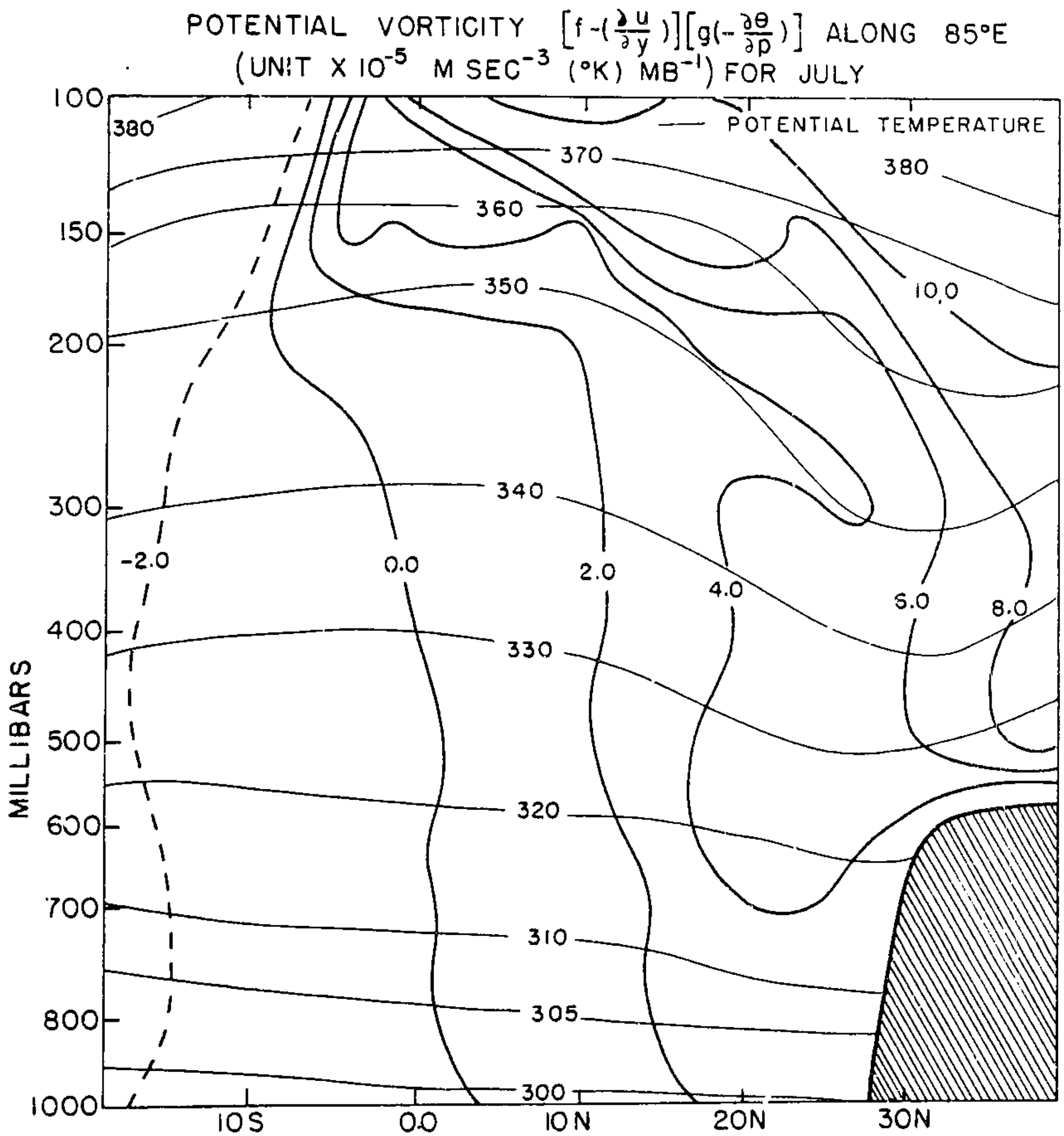

Figure 2.1 Cross-section of potential vorticity ($10^{-5}MS^{-3}MB^{-1}$(°K) along 85E.

$$\left(\frac{\partial}{\partial t}+\bar{U}\frac{\partial}{\partial x}\right)\nabla^2\psi' + \left(\beta - \frac{\partial^2 \bar{U}}{\partial y^2}\right)\frac{\partial \psi'}{\partial x} - f_0 \frac{\partial \omega'}{\partial p} = 0 \tag{2.1}$$

$$\left(\frac{\partial}{\partial t}+\bar{U}\frac{\partial}{\partial x}\right)\frac{\partial \psi'}{\partial p} - \frac{\partial \bar{u}}{\partial p}\frac{\partial \psi'}{\partial x} + \frac{\sigma \omega'}{f_0} = 0 \tag{2.2}$$

where ψ' and ω' are the perturbation stream function and vertical velocity $\left(\frac{dp'}{dt}\right)$, respectively. σ is the stability parameter, which is a function of p only, and is given as:

$$\sigma(\bar{p}) = -\frac{R\bar{T}}{p\bar{\theta}}\frac{\partial \bar{\theta}}{\partial p} \tag{2.3}$$

where the bar (-) denotes the mean over an isobaric surface. f_0 is the constant value of the coriolis parameter and $\beta = \frac{\partial f}{\partial y}$. Assuming geostrophic balance between the mass field and the motion fields, we may derive the omega equation for ω' from (2.1) and (2.2), viz:

$$f_0\frac{\partial^2 \omega'}{\partial p^2} + \frac{\sigma}{f_0}\nabla^2\omega' = \frac{\partial}{\partial p}\left\{\left(\bar{u}\nabla^2 + \beta - u_{yy}\right)\frac{\partial \psi'}{\partial x}\right\} - \nabla^2\left\{\bar{u}\frac{\partial}{\partial p}\left(\frac{\partial \psi'}{\partial x}\right) - \frac{\partial \bar{u}}{\partial p}\frac{\partial \psi'}{\partial x}\right\} \tag{2.4}$$

The first and second terms on the right hand side of (2.4) are respectively the differential vorticity advection and the Lapacian of thickness advection. (A diagnostic ω equation yields that value of vertical velocity that is needed to maintain geostrophic and hydrostatic balance.)

The perturbation ψ' is taken to be of the form

$$\psi'(x, y, p, t) = Re\left\{\Psi(y, p, t)\, e^{ikx}\right\}$$

where Ψ is complex. k is the wavenumber along x.

$$\Psi = \Psi_r + i\,\Psi_i$$

$$\Psi = \left\{ F_r(y,p) + i\, F_i(y,p) \right\} e^{(\nu - ikc)t}$$

Then, $$\Psi_r = \left\{ F_r \operatorname{Cos}(kct) + F_i \operatorname{Sin}(kct) \right\} e^{\nu t}$$

and $$\Psi_i = \left\{ F_i \operatorname{Cos}(kct) - F_r \operatorname{Sin}(kct) \right\} e^{\nu t}$$

Solving for ν and c, we obtain the growth rate

$$\nu = \frac{\Psi_r(\partial\Psi_i/\partial t) + \Psi_i(\partial\Psi_r/\partial t)}{\Psi_r^2 + \Psi_i^2} \qquad (2.5)$$

and the phase speed

$$c = \frac{\Psi_i(\partial\Psi_r/\partial t) - \Psi_r(\partial\Psi_i/\partial t)}{k(\Psi_r^2 + \Psi_i^2)} \qquad (2.6)$$

We may also write $$\omega' = Re\left\{ W e^{ikx} \right\}$$

where $$W = W_r + i\, W_i$$

We may decompose (2.1) and (2.3) for the real and imaginary parts of the complex amplitudes Ψ and W.

Since $$\nabla^2 = \left(-k^2 + \frac{\partial^2}{\partial y^2}\right)$$

we have

$$\frac{\partial}{\partial t}\left(-k^2 + \frac{\partial^2}{\partial y^2}\right)\Psi_r = \bar{U}k\left(-k^2 + \frac{\partial^2}{\partial y^2}\right)\Psi_i + \left(\beta - \bar{U}_{yy}\right)k\,\Psi_i + f_o\frac{\partial W_r}{\partial p} \qquad (2.7)$$

$$\frac{\partial}{\partial t}\left(-k^2+\frac{\partial^2}{\partial y^2}\right)\Psi_i = -\bar{U}k\left(-k^2+\frac{\partial^2}{\partial y^2}\right)\Psi_r - \left(\beta - \bar{U}_{yy}\right)k\Psi_r + f_0\frac{\partial W_i}{\partial p} \tag{2.8}$$

$$\frac{\sigma}{f_0}\left(-k^2+\frac{\partial^2}{\partial y^2}\right)W_r + f_0\frac{\partial^2 W_r}{\partial p^2} = \left[k\left(-k^2+\frac{\partial^2}{\partial y^2}\right)\left\{\bar{U}\frac{\partial \Psi_i}{\partial p} - \Psi_i\frac{\partial \bar{U}}{\partial p}\right\} - k\frac{\partial}{\partial p}\left\{\bar{U}\left(-k^2+\frac{\partial^2}{\partial y^2}\right) + \beta - \bar{U}_{yy}\right\}\Psi_i\right] = F_r \tag{2.9}$$

$$\frac{\sigma}{f_0}\left(-k^2+\frac{\partial^2}{\partial y^2}\right)W_i + f_0\frac{\partial^2 W_i}{\partial p^2} = \left[-k\left(-k^2+\frac{\partial^2}{\partial y^2}\right)\left\{\bar{U}\frac{\partial \Psi_r}{\partial p} - \Psi_r\frac{\partial \bar{U}}{\partial p}\right\} + k\frac{\partial}{\partial p}\left\{\bar{U}\left(-k^2+\frac{\partial^2}{\partial y^2}\right) + \beta - \bar{U}_{yy}\right\}\Psi_r\right] = F_i \tag{2.10}$$

2.2 Numerical Integration of the Ten-layer Quasi-geostrophic Model

A finite difference representation of (2.7) through (2.10) for the model shown schematically in Figure 2.2, was integrated using centered differences in space and time. A forward difference in time was used for the first time step and also at every fiftieth time step, to suppress the separation of the solutions at even and odd numbered time steps. The upper and lower boundary conditions were $\omega' = 0$ at $p = 0$ and $p = 1000$ mb. The lateral boundary conditions were $v' = 0$, i.e., $\psi' = 0$ at the lateral boundaries.

Integrations were performed for two geometrical configurations (Fig. 2.2). In the first case (domain I), a vertical wall was placed at 28.75N. In the second case (domain II), steeply-sloping Himalayan topography was simulated by a vertical wall extending up to 600 mb; the Tibetan plateau extended polewards to 40N, which is the northernmost limit of the domain of integration in the model. A horizontal grid length (Δy) of 138.89 km (1.25 degrees of latitude) and a vertical grid length (Δp) of 100 mb, were used for numerical integrations. The time increments (Δt)

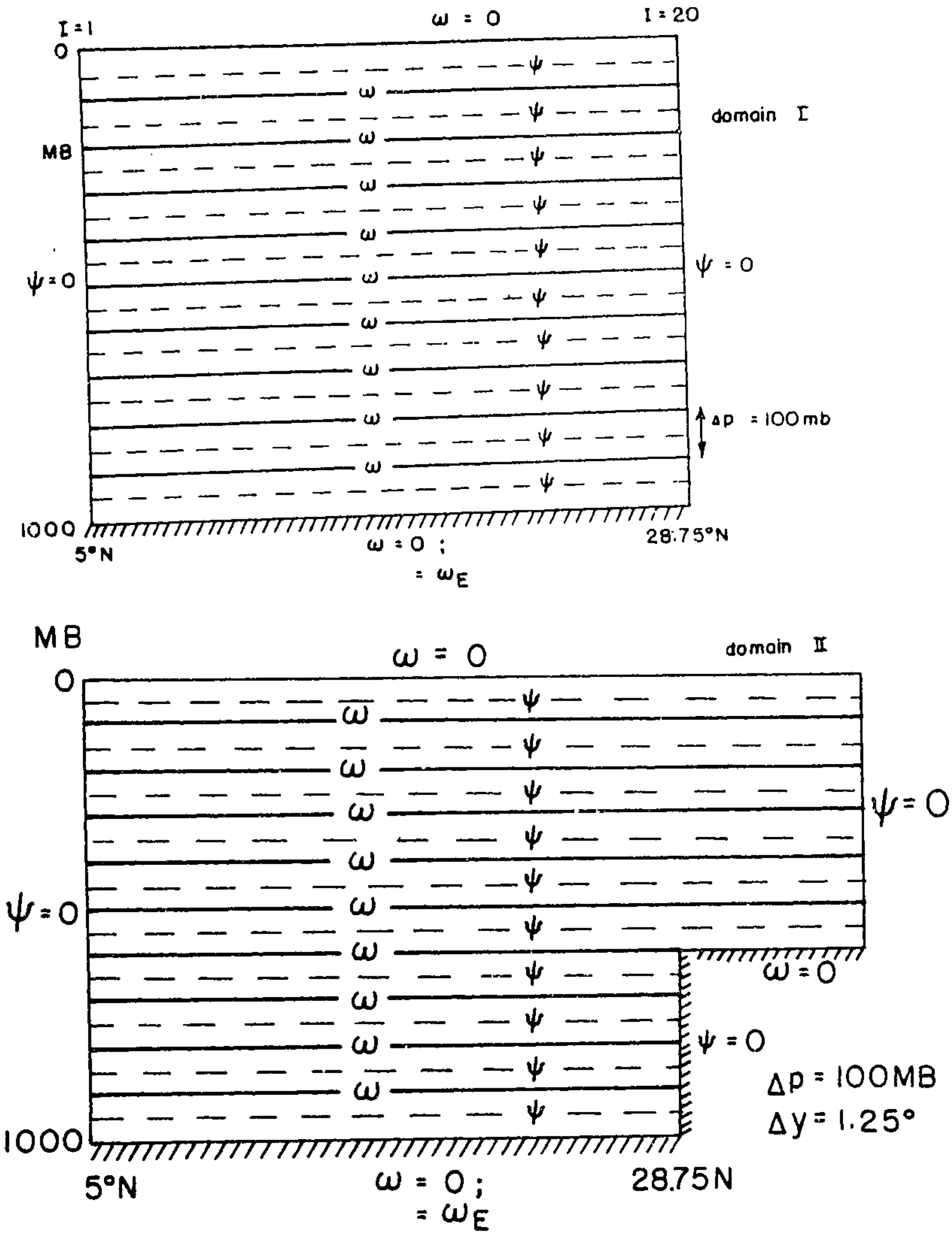

Figure 2.2 Schematic representation of the ten-layer model for domanin I and domain II.

used depended upon the wave number k ($= \frac{2\pi}{L}$, where L is the wavelength); the actual values of Δt were given by

$$\Delta t = \left(k\,\bar{U}_{max}\right)^{-1} \qquad \text{with} \quad \bar{U}_{max} = 40 \text{ m/s}$$

The tendency terms $\frac{\partial \Psi_r}{\partial t}$ and $\frac{\partial \Psi_i}{\partial t}$, were found from (2.7) and (2.8) by use of a one-dimensional relaxation technique. The Liebman relaxation technique with overrelaxation coefficient of 0.3 was used to solve (2.9) and (2.10) at each time step. At the end of every fifty time steps, the phase speed C and growth rate ν were calculated from (2.5) and (2.6). If they had converged to constant values, the integration was terminated. All the integrations began with a constant value of Ψ specified over the whole domain.

We point out that Klein (1974) used $\Delta y = 300$ km for similar numerical calculations and found that for a middle latitude winter profile of $\bar{U}(y,p)$, the most unstable wavelength was 4000 km. In order to assess the effect of the horizontal grid resolution (Δy), we have carried out three experiments with $\Delta y = 69.45$ km, 138.9 km and 277.8 km. For the given $\bar{U}$ (y, p), the wavelength of maximum growth rate remained nearly the same for the cases $\Delta y = 69.45$ km and $\Delta y = 138.9$ km, but for the case $\Delta y =$ 277.8 km, the wavelength of maximum growth rate increased by nearly 1000 km. These integrations indicated that coarse resolution may introduce a numerical viscosity which may change the shape of the growth rate curve.

2.3 Structure of the Most Unstable Mode

Figure 2.3 shows the growth rate and phase speed versus wavelength curves obtained for domains I and II. In both these cases, the wavelength of the most rapidly growing perturbation is 3000 km. The e- folding times

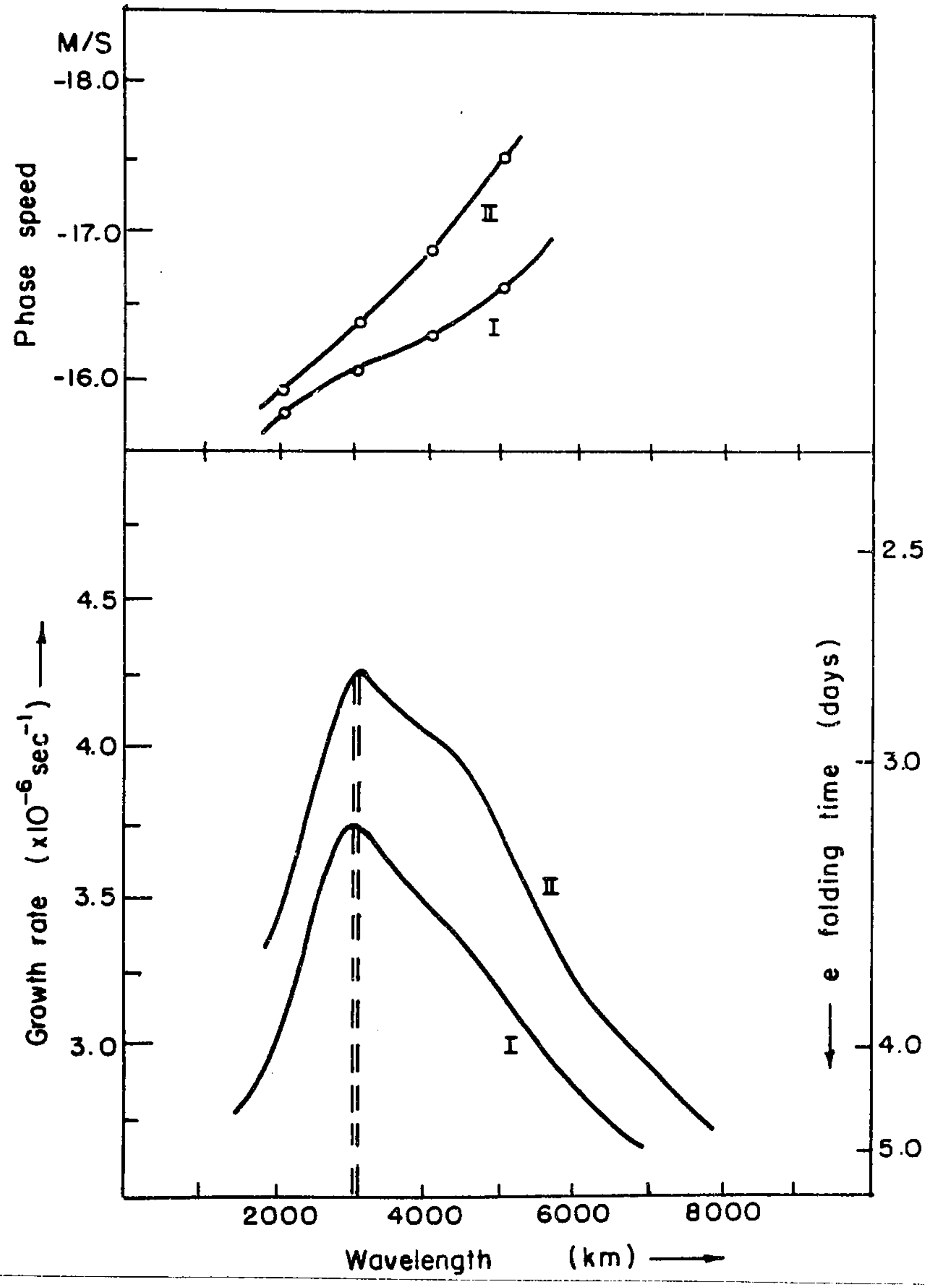

Figure 2.3 Growth rate and phase speed versus wavelength for domain I and domain II.

for cases I and II were 3.2 days and 2.6 days, respectively. This difference in the growth rates is due to the differences in available kinetic energy density. These, in turn, are due to the relative locations of the subtropical westerly jet and the tropical easterly jet at 150 mb. Figure 2.4 shows the structures of the amplitude and phase of Ψ for both cases. The amplitudes are found to be concentrated at 150 mb and fall off very rapidly at the lower layers. Since the amplitudes vary over orders of magnitude in the vertical, the phase lines are not very meaningful. The presence of an elevated plateau in domain II has no appreciable effect on the structure of the perturbation above 600 mb. It only affects the kinematics near the plateau boundary.

These results suggest that it is the barotropic instability of the flow at 150 mb which is responsible for the structure and the growth of the most unstable mode; since the model is vertically coupled through the $f_0 \frac{\partial \omega}{\partial p}$ term, the fastest growing mode of the barotropically unstable 150 mb flow dominates the whole domain. This suggestion will be examined further in section 2.4.

Since the horizontal scale of the most unstable mode is about 3000 km, we have examined the horizontal uniformity of the mean zonal flow over a longitudinal belt of 3000 km. Figure 2.5 displays the cross-section of potential vorticity along 73E and 100E. Comparison between Figure 2.5 and Figure 2.1 shows that the mean zonal flow is homogeneous between the longitudes 73E and 100E, and therefore, such a perturbation analysis is justified.

2.4 Energetics of the Most Unstable Mode

In order to gain some further insight into the characteristics of

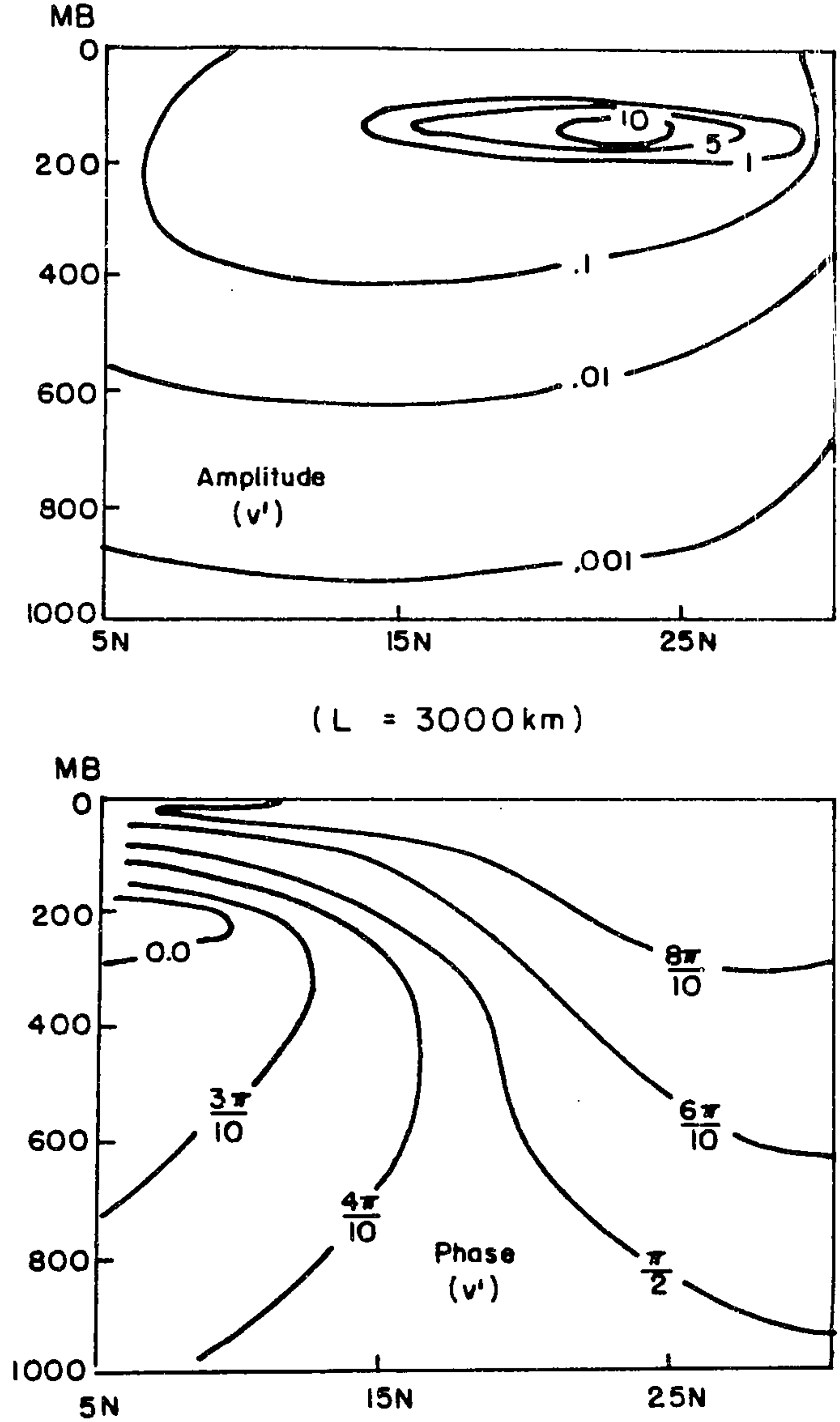

Figure 2.4a Amplitude and phase structure of the most unstable mode (wavelength = 3000 km) for domain I.

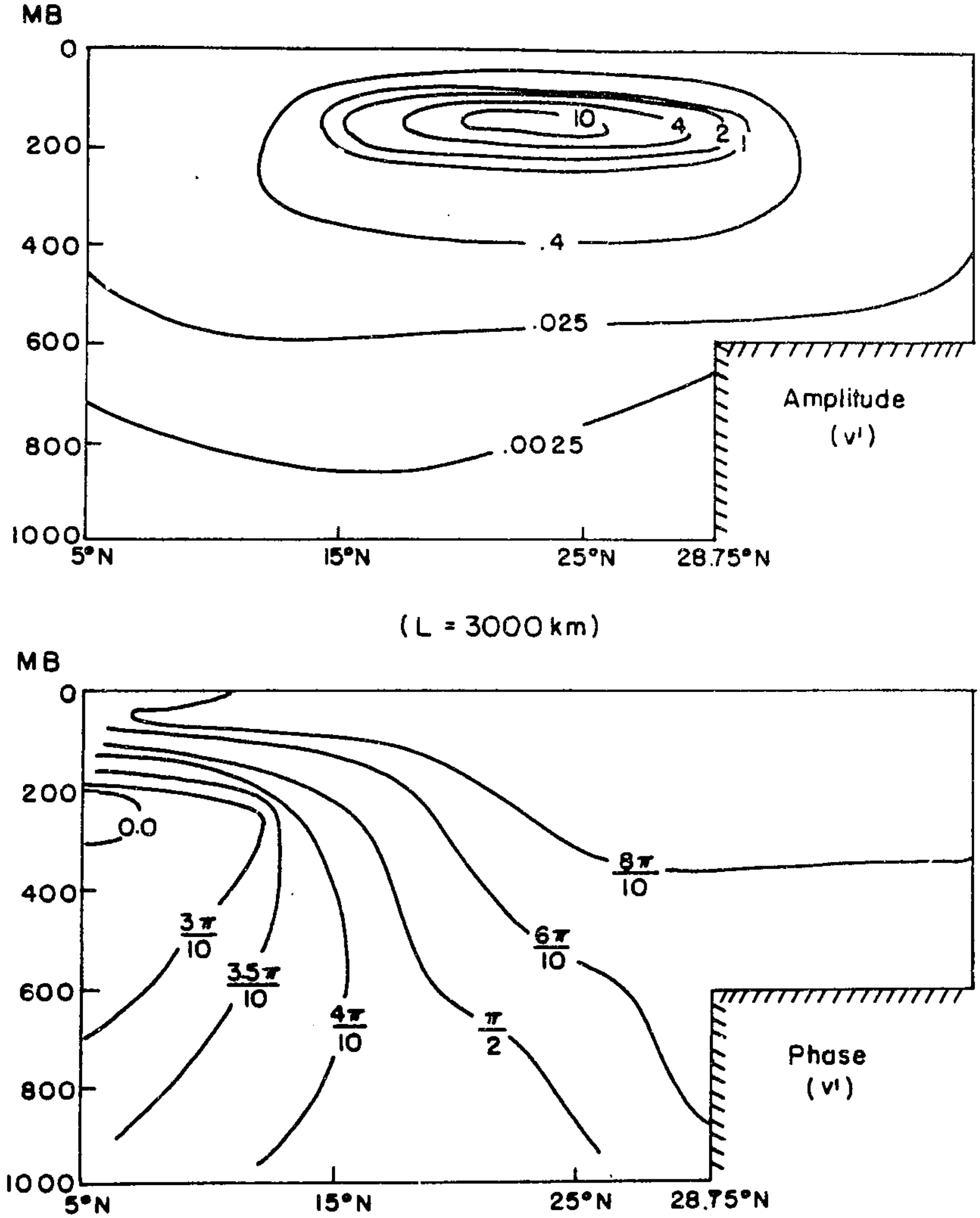

Figure 2.4b Same as Figure 2.4a for domain II.

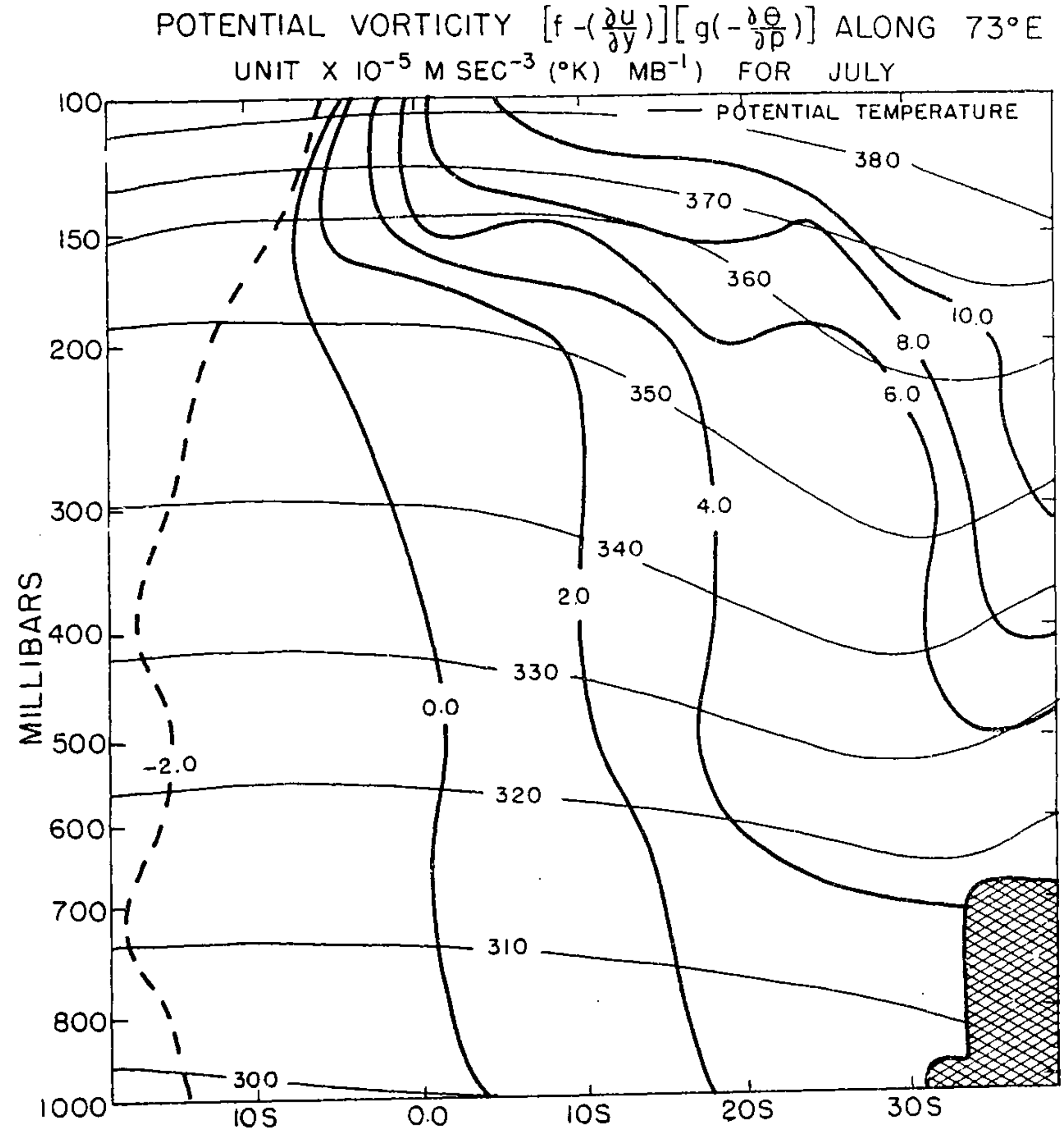

Figure 2.5a Same as Figure 2.1 along 73E.

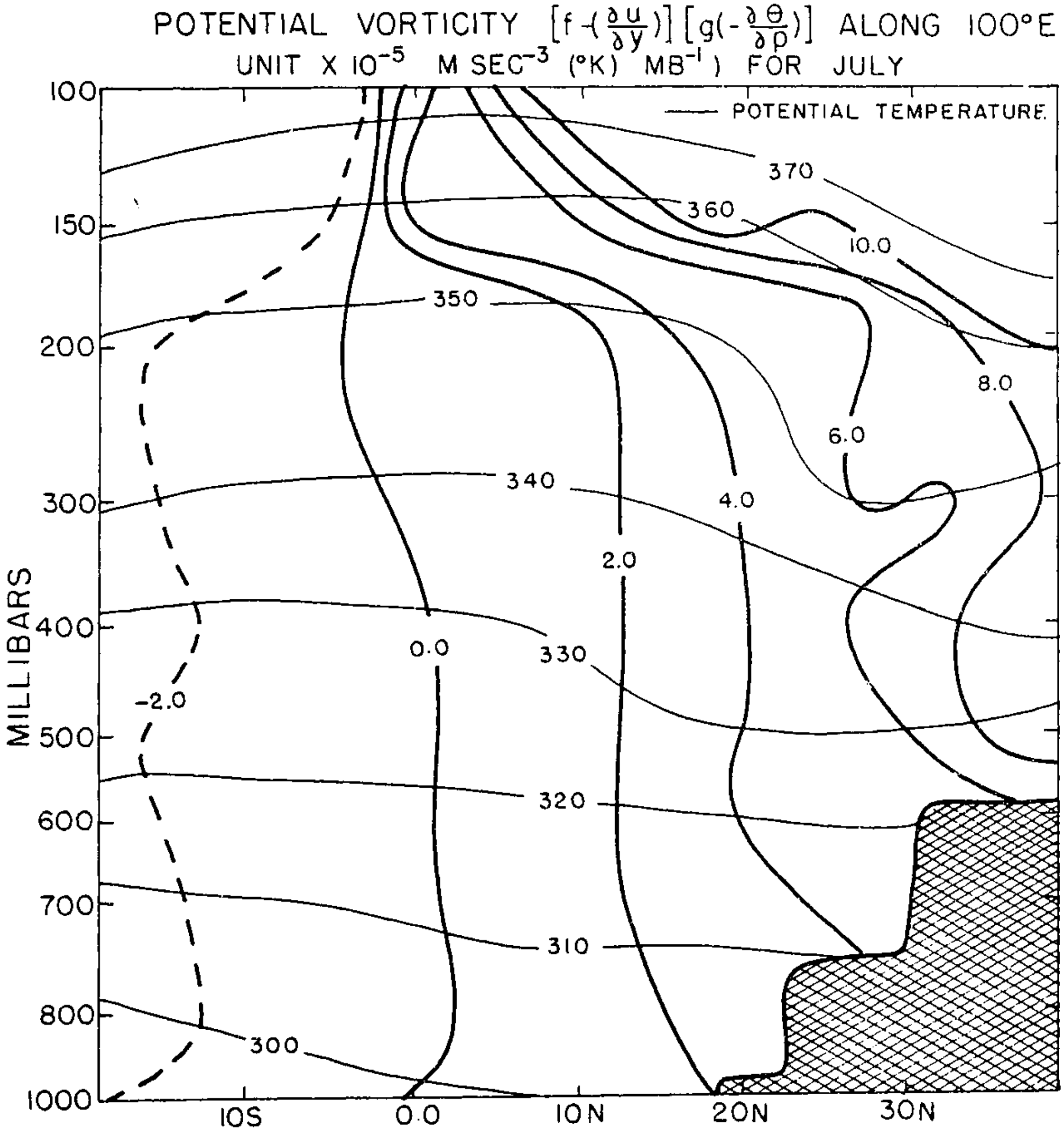

Figure 2.5b Same as Figure 2.1 along 100E.

the unstable modes, energy transformations were calculated for the most unstable mode (L = 3000 km) for domains I and II. Results for both domains were nearly identical (the northern boundary did not affect the results), because the amplitudes were concentrated at 150 mb.

Expressions for the conversion of eddy kinetic energy to zonal kinetic energy, C(KE, KZ); for zonal available potential energy to eddy available potential energy, C(AZ, AE); and for eddy available potential energy to eddy kinetic energy, C(AE, KE), are given as follows:

$$C(KE,\ KZ) = \int_0^{p_0}\int_0^{D} \bar{\Psi}\,\frac{\partial^2 (\overline{u'v'})}{\partial y^2}\,dy\,dp = \frac{k}{2Dg}\int_0^{p_0}\int_0^{D} \frac{\partial \bar{U}}{\partial y}\left(\Psi_i \frac{\partial \Psi_r}{\partial y} - \Psi_r \frac{\partial \Psi_i}{\partial y}\right) dy\,dp$$

$$C(AZ,\ AE) = \int_0^{p_0}\int_0^{D} \frac{f_0^2}{\sigma}\,\frac{\partial \bar{\Psi}}{\partial y}\,\frac{\partial}{\partial y}\left\langle \frac{\partial \psi'}{\partial x}\frac{\partial \psi'}{\partial p}\right\rangle dy\,dp = \frac{k f_0^2}{2Dg}\int_0^{p_0}\int_0^{D} \frac{1}{\sigma}\,\frac{\partial \bar{U}}{\partial p}\left(\Psi_r \frac{\partial \Psi_i}{\partial p} - \Psi_i \frac{\partial \Psi_r}{\partial p}\right) dy\,dp$$

$$C(AE,\ KE) = \int_0^{p_0}\int_0^{D} f_0\,\omega' \frac{\partial \psi'}{\partial p}\,dy\,dp = \frac{f_0}{2Dg}\int_0^{p_0}\int_0^{D}\left(W_r \frac{\partial \Psi_r}{\partial p} + W_i \frac{\partial \Psi_i}{\partial p}\right) dy\,dp$$

where D = lateral width of the domain = $19\,\Delta y$

and p_0 = surface pressure = 1000 mb, $\langle\ \rangle$ denotes domain average.

Figure 2.6 shows the numerical values of these conversions in arbitrary units. We see that the most dominant conversion is from KZ to KE, which demonstrates the importance of barotropic instability.

This also suggests that the barotropic instability of the zonal flow at 150 mb may be the primary excitation mechanism for these modes. In order to verify this result, a barotropic instability analysis was performed for the zonal flow at the 150 mb level.

Figure 2.7 displays the results of the barotropic-baroclimic insta-

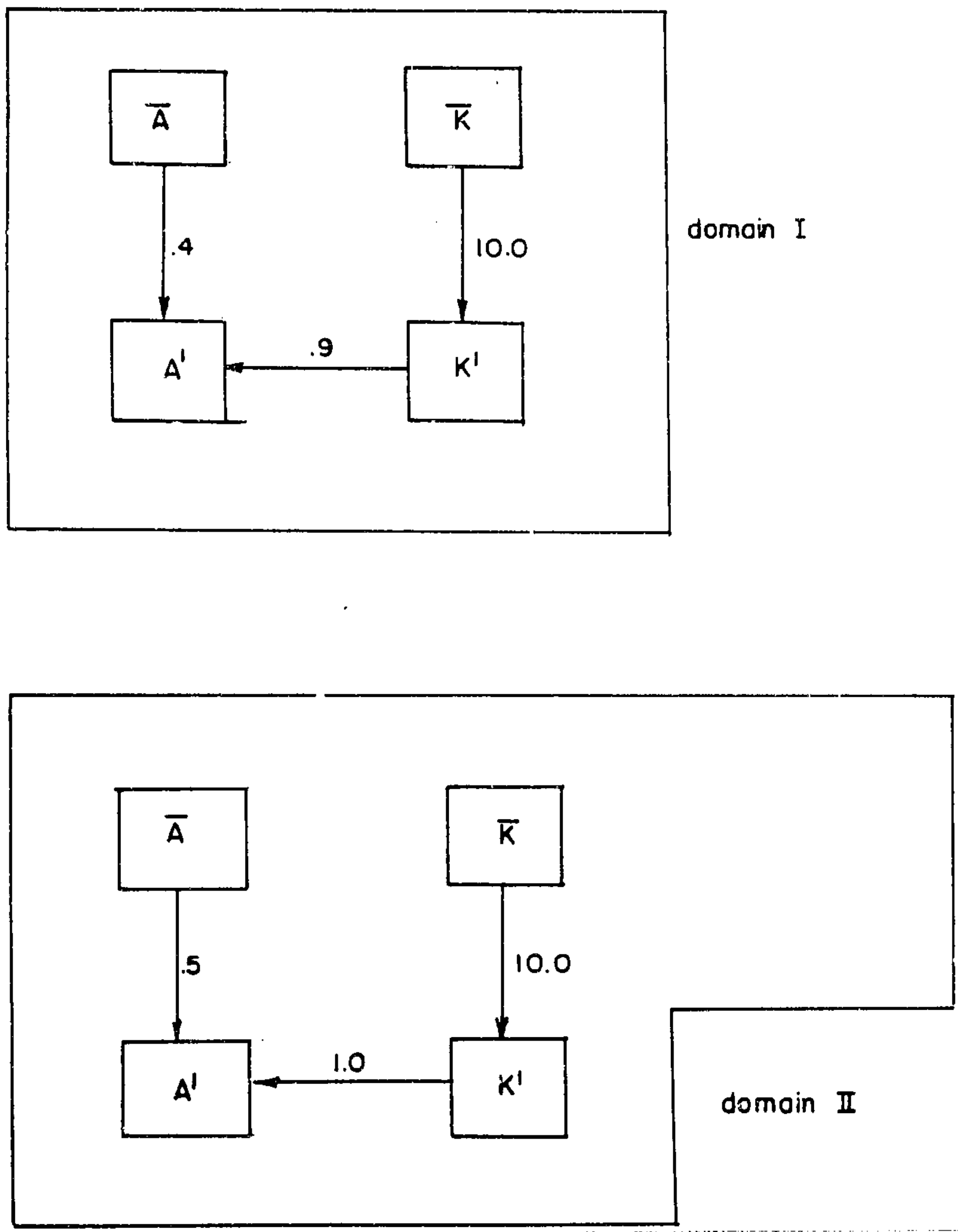

Figure 2.6 Energy transformations (in arbitrary units) for the most unstable mode (wavelength = 3000 km) for domain I and domain II.

bility analysis for the entire domain I, and the barotropic instability analysis of the zonal flow at 150 mb. It may be seen that both curves are almost identical, confirming the earlier suggestion that most of the contribution to the instability shown in Figure 2.3 comes from the barotropic instability at 150 mb. In fact, the growth rate is slightly higher for the barotropic (150 mb) case, because the lower levels have weaker horizontal and vertical shears, and therefore, smaller available kinetic energy and available potential energy. The same conclusion could have been reached by examining the time evolution of the patterns of convergence for phase speed and growth rate during the integration. For example, it was observed that the convergence of c and ν occurred first at 150 mb and then proceeded downwards. This reflects the influence of the instability at 150 mb level on the lower levels, through the vertical coupling. However, the time scale over which all the levels become 'contaminated' by the instability of 150 mb is very large (50 days), compared to the period of the most unstable wave at 150 mb (3 days).

The growth rates and the phase speeds for a range of wavelengths were also calculated for the case where $\frac{\partial U}{\partial p} = 0$ and $U(y)$ at each level was the same as $U(y)$ at 150 mb. The results were very similar to the one shown in Figure 2.7 for the 150 mb barotropic case.

The results of this section suggest that it is rather unlikely that the barotropically unstable disturbances at 150 mb could account for the observed monsoon depressions which have amplitude maxima at the lower tropospheric levels, and are rarely detected at 200 mb.

2.5 Role of Barotropic-Baroclinic Instability in the Growth of the Monsoon Depressions

The results of the preceding section indicate that the zonal wind at

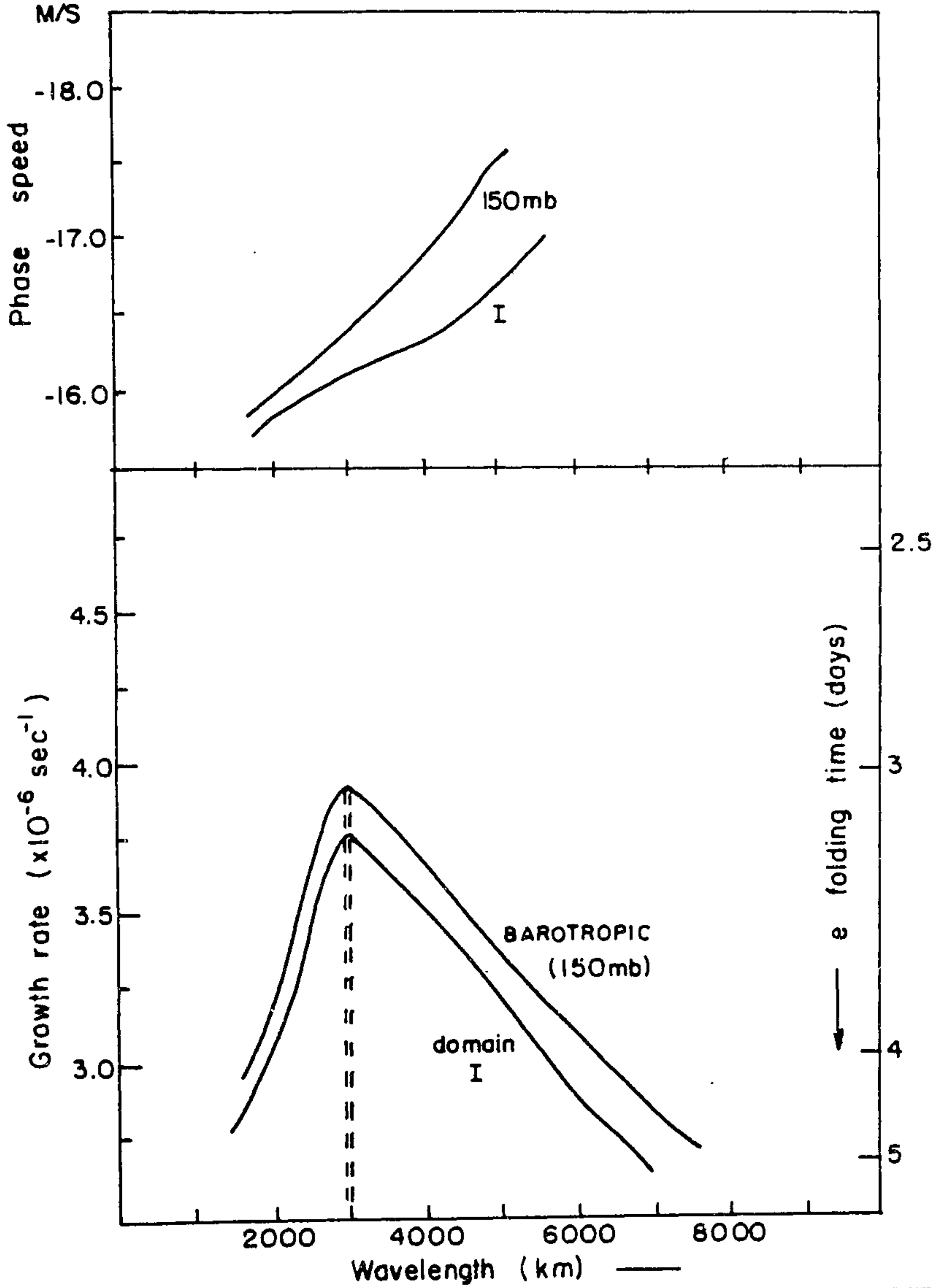

Figure 2.7 Growth rate and phase speed versus wavelength for domain I and for barotropic instability at 150 MB.

150 mb is barotropically unstable, and that the fastest growing mode has the wavelength of 3000 km. The conversion, C(AZ, AE), is small, and therefore, the baroclinic instability mechanism is not important. The structure of the most unstable mode is such that most of the amplitude is concentrated at 150 mb. Since the vertical shear of the mean monthly (July) meridional wind over the Bay of Bengal is small ($\frac{\partial \bar{V}}{\partial z} \approx .3 m/s/km$) and the static stability in the lower troposphere is large (Richardson number $\approx$ 100), the baroclinic instability of the mean meridional wind will not be important for the growth of monsoon depressions.*

Although the necessary conditions for internal jet instability are satisfied, the above results suggest that this is not the mechanism for the growth of the monsoon depressions. It is rather unlikely that the barotropically unstable disturbances at 150 mb could account for the observed monsoon depressions which have their amplitude maxima at the lower tropospheric levels and are rarely detected at 200 mb. Therefore, proper inclusion of moist-convective heating seems to be not only desirable, but essential to explain the growth of the monsoon depressions.

These results, however, seem to explain the occurrence of westward propagating waves at 200 mb. The phase speed of the computed most unstable perturbation (see section 2.3) agrees reasonably well with the observed phase speeds of 10-12° longitude/day at 200 mb (Krishnamurti, 1971). These results also support the hypothesis of Colton (1973) that small-scale waves at 200 mb are continuously draining the energy of the mean motion and quasi-stationary large-scale waves.

*A paper by Mak (December 1975, J.Atmos.Sci.) on baroclinic instability of a flow with a meridional wind component, which appeared after the thesis was completed, is not relevant because of the very large meridional wind shear in the basic flow.

CHAPTER 3. INSTABILITY OF VERTICALLY SHEARING ZONAL FLOW WITH EMPIRICAL VERTICAL DISTRIBUTIONS OF CISK-TYPE HEATING

3.1 The CISK

Charney and Eliassen (1964) have suggested that the development of tropical disturbances in a conditionally unstable atmosphere may be viewed as a kind of secondary instability in which the cumulus and cyclone-scale motions cooperate, rather than compete, in such a way that the low level synoptic convergence, as well as frictional convergence in the boundary layer, pumps moisture upwards to the cloud base. The upward pumping is further accelerated by the latent heat of condensation. In response to the accelerating upward mass flux in the clouds, there is a compensating sinking in the immediate cloud environment. The associated heating by adiabatic compression increases the mean buoyancy and therefore the mean upward velocity with height. The resulting stretching of the vortex tubes of the earth's vorticity intensifies the cyclonic vorticity and enhances the low level convergence and therefore increases the heating. This mechanism is referred to as the Conditional Instability of the Second Kind (CISK) (Charney, 1973).

Our main objective in this and the following chapters will be to investigate the plausibility of CISK theory as a mechanism for the growth of the monsoon depressions.

Although the CISK theory indicates that the moist-convective heating should be related to the total convergence of moisture into a vertical unit column, it does not determine how this heating should be distributed in the vertical. In the original formulations of Charney and Eliassen (1964), they took only two layers with equal heating and in Charney (1971), the thermodynamic equation was used only at one mid-atmospheric level, where the heating was specified.

The determination of the actual vertical distribution of heating requires a parameterization of moist convection in a conditionally unstable atmosphere. The first reasonable theory for such a parameterization was proposed only very recently by Arakawa and Schubert (1974). In the past, several studies have been carried out with empirical or very simplified specifications of the vertical heating function (Yamasaki, 1969; Hayashi, 1970; Chang, 1971; Lindzen, 1974). Such studies can be broadly put into two categories. In the first category, it is assumed that the heating is proportional to the Ekman pumping only (viz., Chang, 1971), i.e., $$Q \sim \eta(p)\, \omega_E$$
where ω_E denotes the Ekman pumping.

In the second category (Yamasaki, 1969, etc.), it is assumed that the heating is proportional to the vertical velocity at the top of the lowest layer, i.e., $$Q \sim \eta(p)\, \omega^*$$
where ω^* denotes the vertical velocity at the top of the lowest layer. The contention here is that the wave convergence, with or without Ekman pumping should be used to parameterize the heating.

We will refer to these two parameterizations as Ekman-CISK, and Wave-CISK, respectively.

$$Q \sim \eta(p)\, \omega_E \qquad \text{Ekman-CISK}$$

$$Q \sim \eta(p)\, \omega^* \qquad \text{Wave-CISK}$$

Yamasaki (1969) performed the instability analysis for the growth of tropical disturbances, using wave-CISK type heating. His choices of $\eta(p)$, however, were totally arbitrary.

Recent diagnostic studies by Yanai, et. al (1973) and several others have shown a vertical distribution of heating due to moist-convection associated with tropical systems. Although these studies describe the heating distribution for particular type of disturbances occurring over particular geographical regions, they may provide a reasonable representation of the heating distribution function for those tropical disturbances which have significant moist-convective activity associated with them. Therefore, the vertical distribution function η may now be chosen in a less arbitrary manner. Here, we will present the results of instability analysis with specified η profiles for two cases where heating is of Ekman-CISK type, and wave-CISK type, respectively. The more complete problem of parameterizing the effects of cumulus heating, in terms of large-scale variables, using the quasi-equilibrium assumption of Arakawa and Schubert (1974), will be studied in the next chapter.

3.2 The Ten-layer Model with Vertical Shear

If $\dot{Q}$ is the rate of heating per unit mass, (2.2) may be written as:

$$\left(\frac{\partial}{\partial t}+\bar{U}\frac{\partial}{\partial x}\right)\frac{\partial \psi'}{\partial p}+\frac{\partial \bar{U}}{\partial p}\frac{\partial \psi'}{\partial x}+\frac{\sigma}{f_0}\omega'=\frac{R}{c_p p}\frac{\dot{Q}}{f_0}\equiv\hat{Q} \tag{3.1}$$

The heating parametrization is:

$$\hat{Q}=\eta(p)\frac{\sigma}{f_0}\omega_E' \tag{3.2}$$

or

$$\hat{Q}=\eta(p)\frac{\sigma}{f_0}\omega^{*'} \tag{3.3}$$

where $\omega^{*'}$ is the vertical velocity at the 900 mb level, which corresponds to the top of the lowest layer (see Fig. 3.1).

ω_E' may be given as (Charney, 1971):

$$\left.\begin{aligned} \omega_E' &= -g f_0 \frac{D}{2} \zeta'_{j=10} \\ \text{where} \quad \zeta'_{j=10} &= \nabla^2 \psi'_{j=10} \\ \text{and} \quad D &= \sqrt{\frac{2\nu}{f_0}} \quad ; \quad \nu = 100 \text{ m}^2/\text{s} \end{aligned}\right\} \quad (3.4)$$

Since ω is, in general, complex, we may take

$$\hat{Q} = \hat{Q}_r + i \hat{Q}_i \quad (3.5)$$

For $\frac{\partial}{\partial y} = 0$, the system (2.7-2.10) may be written as:

$$\frac{\partial \Psi_r}{\partial t} = \bar{U} k \Psi_i - \frac{\beta \Psi_i}{k} - \frac{f_0}{k^2} \frac{\partial W_r}{\partial p} \quad (3.6)$$

$$\frac{\partial \Psi_i}{\partial t} = -\bar{U} k \Psi_r + \beta \frac{\Psi_r}{k} - \frac{f_0}{k^2} \frac{\partial W_i}{\partial p} \quad (3.7)$$

$$\frac{\partial^2 W_r}{\partial p^2} - \frac{\sigma k^2}{f_0^2} W_r = F_r - \frac{k^2}{f_0} \hat{Q}_r \quad (3.8)$$

$$\frac{\partial^2 W_i}{\partial p^2} - \frac{\sigma k^2}{f_0^2} W_i = F_i - \frac{k^2}{f_0} \hat{Q}_i \quad (3.9)$$

where F_r and F_i are the right-hand sides of (2.9) and (2.10) for $\frac{\partial}{\partial y} = 0$.

We solve the above equations (3.6)-(3.9), using the procedure described in Chapter 2.

3.2.1 Specification of the heating profile η.

We have experimented with two versions of the η specification: a) constant η profile, and b) variable η profile.

Constant η profile:

In this case,

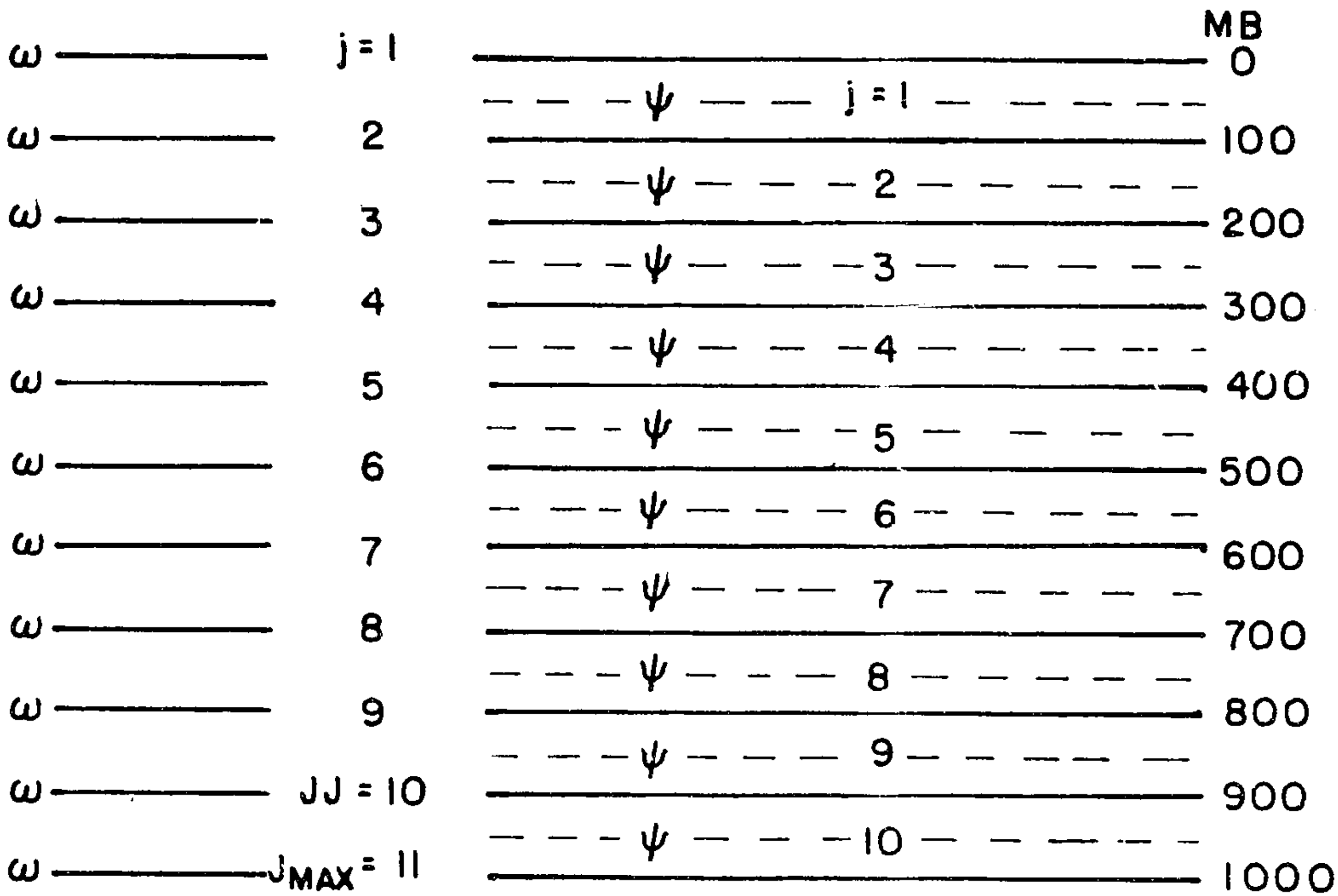

Figure 3.1 Schematic representation of the ten-layer model.

$$\eta = \text{constant} \tag{3.10}$$

and from (3.2) or (3.3)

$$\hat{Q} = \alpha\left(-\frac{M_B}{f_0}\right)\sigma \tag{3.11}$$

where $-M_B$ denotes either ω_E or ω^*. For a constant value of η, the heating realized under this formulation may be considered as equivalent to the heating provided by a non-entraining deep cloud and $\frac{M_B}{g}$ may be considered as the mass flux at the base of the cloud. This clearly shows the weakness of this formulation, because the mass flux at the base of the cloud need not be just equal to the Ekman pumping or vertical velocity at the top of the lowest layer. However, in this chapter, our aim is to study the effects of such simple formulations with empirical heating profiles, so that we can make a realistic assessment of the adequacy and validity of such formulations.

The approach in this section, therefore, may be considered as an intermediate step between the totally arbitrary specifications of the heating functions like Yamasaki (1969) and Koss (1975), etc., and the heating profile obtained by the application of a closure theory of parameterization. The primary motivation for presenting these results is not to explain the growth of tropical/monsoon disturbances, but to point out the sensitivity of the results to the specification of the vertical heating distribution function.

If we assume that the moist air entering the base of the clouds is saturated and has mixing ratio q^*, the total realisable heating in the interior is given by:

$$Q_{\text{total}} = \frac{L M_B q^*}{g} \tag{3.12}$$

where L is the latent heat of condensation. In (3.11), α is determined by imposing the consistency constraint that the total heating realized in the interior should be equal to Q_{total}. If we further assume that Q_{total} heats the atmosphere between the pressure levels p_* and p_T (which denote the base and the top of the hypothetical cloud), the consistency condition requires that:

$$\frac{L M_B q^*}{g} = \int_{p_*}^{p_T} \left(\frac{M_B}{g} \frac{c_p}{R} p\sigma\right) dp \tag{3.13}$$

and therefore,

$$\alpha = \frac{L (R/c_p)\ q^*}{\int_{p_*}^{p_T} (p\sigma)\, dp} \tag{3.14}$$

One of the primary reasons for imposing the consistency condition is to make possible the intercomparisons among the results for different vertical distributions. In order to make such comparisons, the vertically integrated total heating should be kept constant in each case, and only the vertical distribution should be different. Profiles η', η'', η''' (Fig. 3.4) give the same amount of total heating. (Heating due to η' and η_1 is not the same.)

Variable η profile

We have also made instability calculations with a variable η specification, where the functional form of η is the same as the vertical profile of Q given by Yanai, et. al (1973). We recognize that this heating distribution was obtained from the data of the Marshall Islands area and it is by no means a universal heating profile; however, it does provide a quantitative heating distribution in a synoptic situation in which heating was provided by moist convection processes.

If Q_y denotes the Q value in Yanai, et. al (1973), (see Fig. 3.2), we may determine $\eta_y(p)$ as:

$$\eta_y(p) = \frac{Q_y(p)}{Q_y(p_*)} \tag{3.15}$$

where p_* = 900 mb for our calculations.

Therefore, $$\eta_y(p_*) = 1$$

Now, in our model, $\hat{Q}$ is given as:

$$\hat{Q} = \frac{-\alpha M_B \sigma}{f_0}$$

and $$M_B = -\eta(p)\,\omega_E$$

or $$M_B = -\eta(p)\,\omega^*$$

As discussed before, α is now determined by:

$$= \frac{L\,(R/c_p)\,q^*}{\int_{p_*}^{p_T} (p\eta\sigma)\,dp} \tag{3.16}$$

For our calculations, we need $\eta(p)$, which is the vertical profile of M_B. Since $\eta_y(p)$ is the vertical profile of $M_B \frac{\partial \bar{S}}{\partial p}$, we may calculate the vertical profile of M_B using $\eta_y(p)$ and the known vertical profile of $\frac{\partial \bar{S}}{\partial p}$.

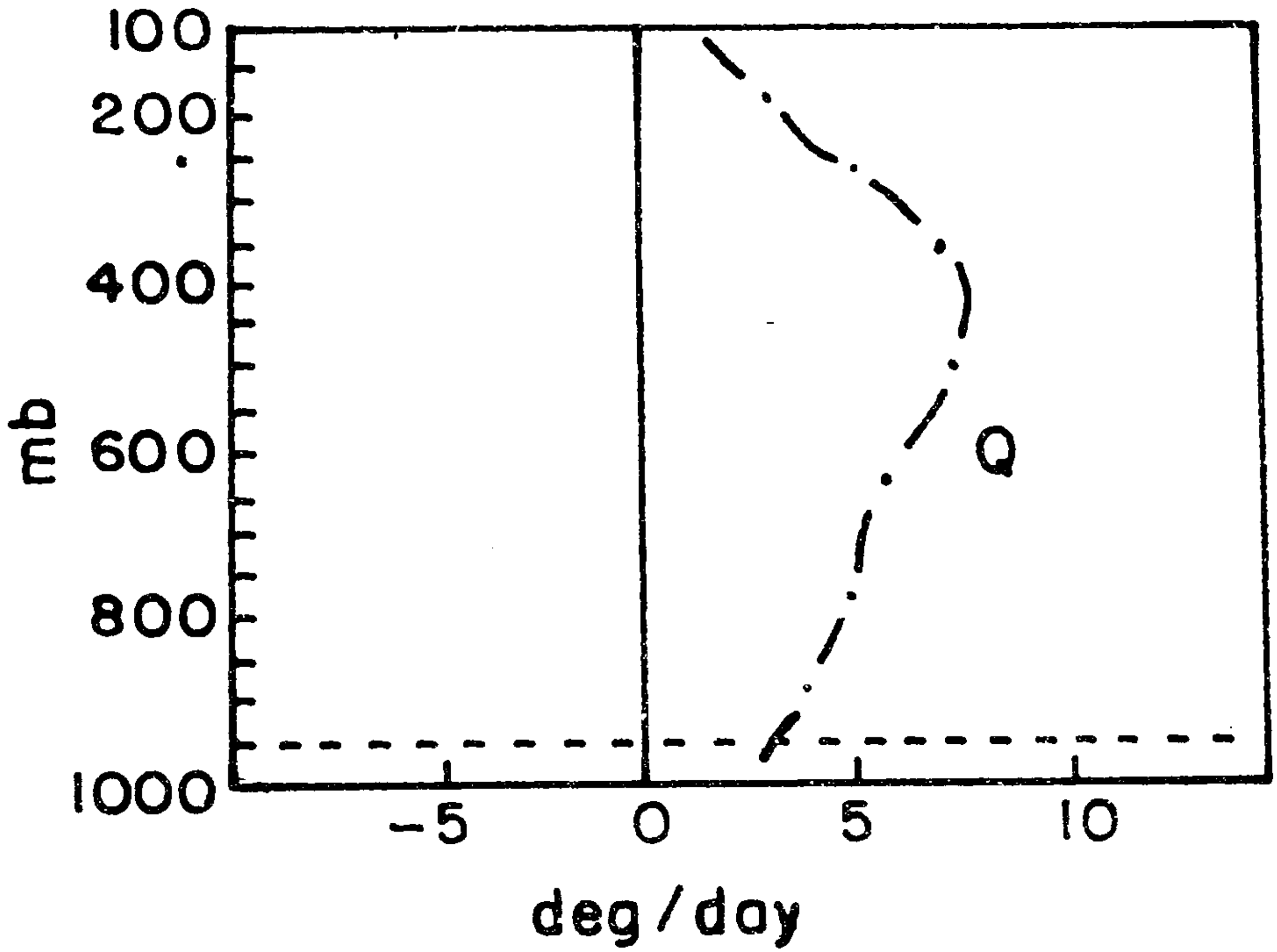

Figure 3.2 Vertical distribution of non-radiative diabatic heating over the Marshall Islands region (From: Yanai et. al, 1973).

$$\frac{\partial \bar{s}}{\partial p} = c_p\left(\frac{p}{p_o}\right)^{R/c_p} \frac{\partial \bar{\theta}}{\partial p}$$

$$\frac{(\partial \bar{s}/\partial p)}{(\partial \bar{s}/\partial p)^*} = \frac{T\theta^*(\partial \bar{\theta}/\partial p)}{T^*\theta\,(\partial \bar{\theta}/\partial p)^*} = \frac{p\sigma}{p^*\sigma^*}$$

(where $*$ refers to the reference level, 900 mb).

$$\eta_y(p) = \left[M_B\,(\partial \bar{s}/\partial p)\right] / \left[M_B^*\,(\partial \bar{s}/\partial p)^*\right]$$

$$M_B(p) = M_B^*\ \eta(p)$$

Therefore, we have:

$$\eta(p) = \eta_y(p)\frac{p_*\sigma^*}{p\,\sigma} \qquad (3.17)$$

The η profile given by (3.17) is designated as η_1 in Figure 3.3. η_2 and η_3 in Figure 3.3 are two other artificial modifications of the profile, in which heating does not occur above 400 mb, and 600 mb, respectively. Similarly, Figure 3.4 shows three types of constant η profiles designated as η', η'', η''', in which heating does not occur above 200 mb, 400 mb, and 600 mb, respectively. The value of α given by (3.14) is shown along the x axis. We have presented the results of instability analysis, using these six η profiles. Vertical structure of the mean zonal wind is shown in Figure 3.5. q^* is taken as 20 gm/kgm.

3.3 Numerical Procedure

For the case of Ekman-CISK heating, the forcing terms on the r.h.s. of (3.8) and (3.9) contain only terms in Ψ and the method of solving these equations for the ten-layer model (Fig. 3.1) is the relaxation method described in Chapter 2. But, for wave-CISK type heating, $\hat{Q}$ is

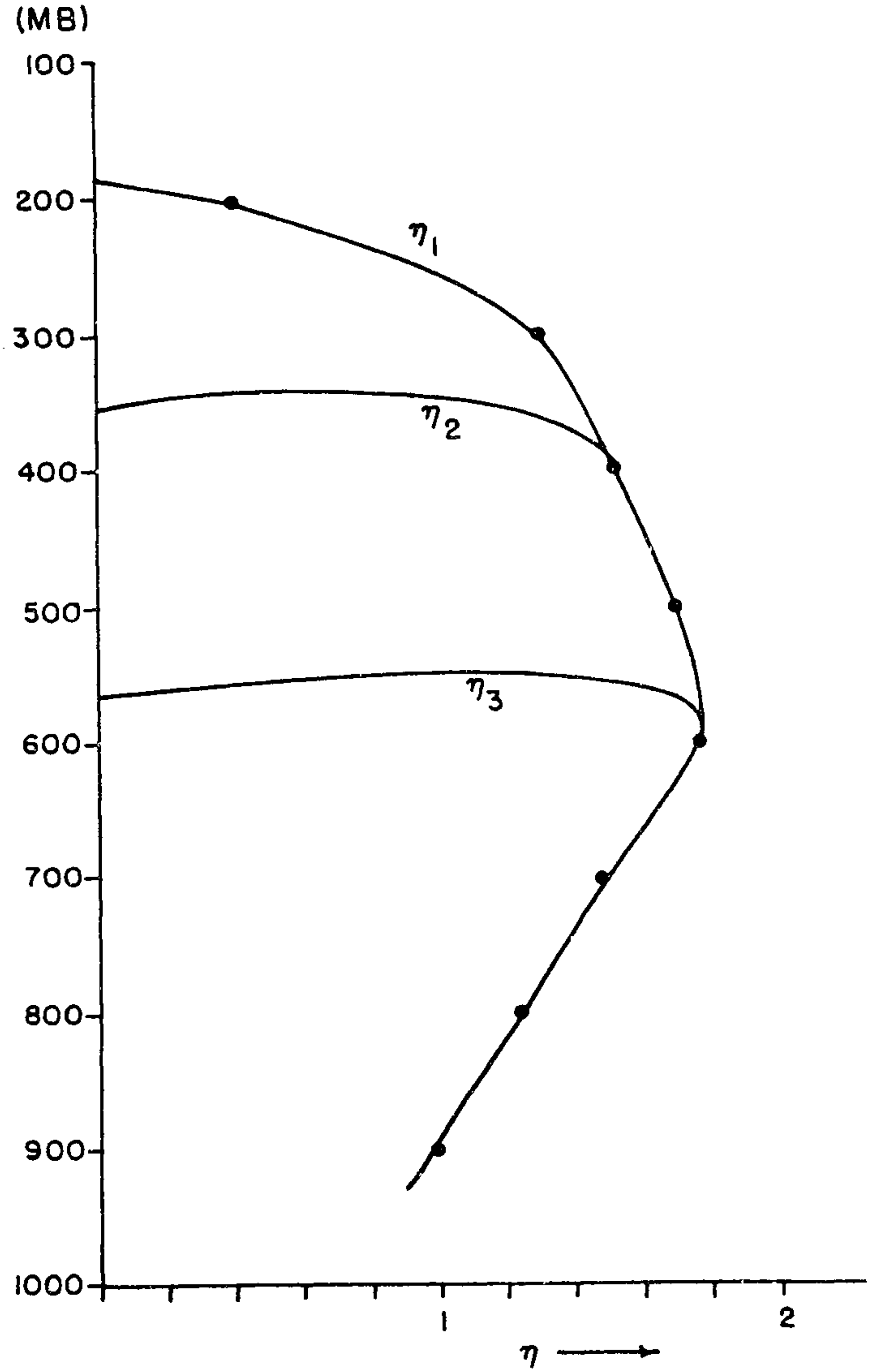

Figure 3.3 Shape of the vertical distribution functions η_1, η_2, η_3.

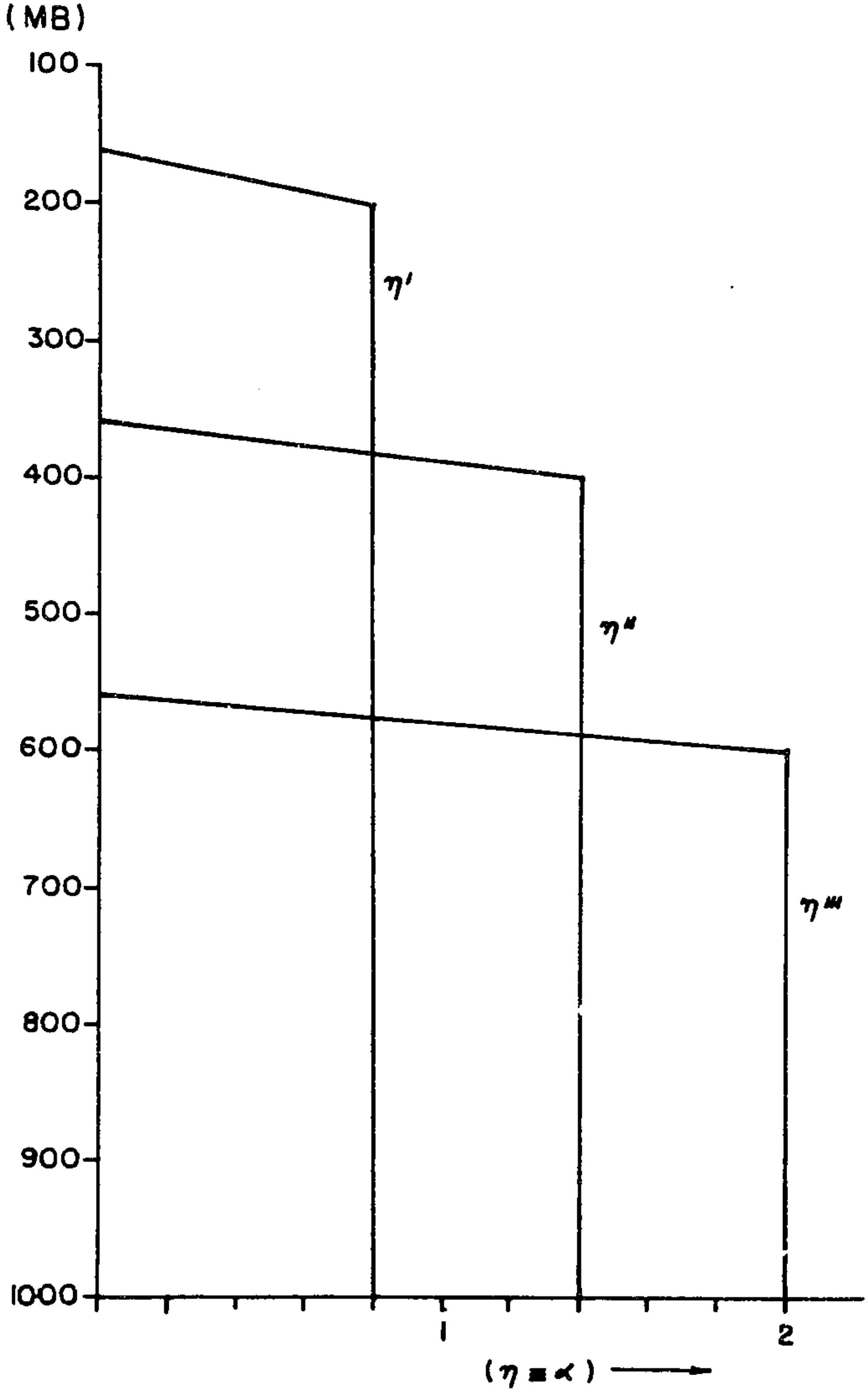

Figure 3.4 Shape of the vertical distribution functions η', η'', η'''.

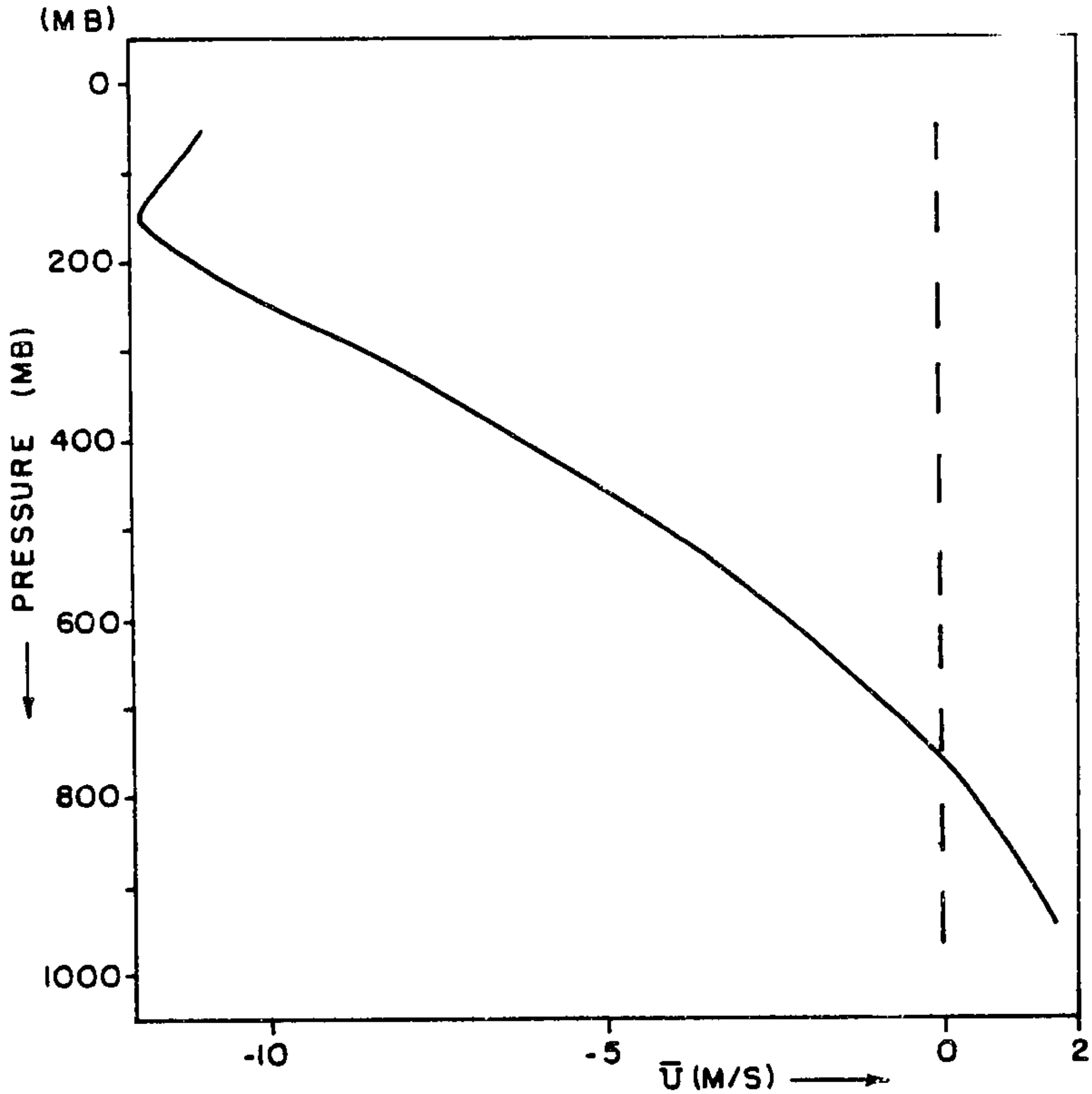

Figure 3.5 Vertical profile of the zonal wind.

proportional to $W(j=10)$, which is the unknown variable on the l.h.s. of (3.8) and (3.9), to be determined. In this case, the relaxation technique is not desirable. The technique we follow here is a modified version of the method described by Richtmyer and Morton (1967, page 200), which is merely a special adaptation of the Gauss elimination procedure. The modification is needed to account for the fact that the r.h.s. of (3.8) and (3.9) are functions of $W(j=10)$.

The finite-difference form of (3.8) or (3.9) may be written (see Fig. 3.1) as:

$$a_j \omega_{j-1} + b_j \omega_j + c_j \omega_{j+1} = d_j + e_j \omega_{JJ} \qquad (j = 2, JJ) \tag{3.17}$$

where $JJ = JMAX-1 = 10$

For (3.8), the coefficients a_j, b_j, c_j, d_j, e_j are given as:

$$\left.\begin{aligned} a_j &= 1 \\ b_j &= -(2 + k^2 \sigma_J \Delta p^2 / f_0^2) \\ c_j &= 1 \\ d_j &= F_j (\Delta p)^2 / f_0 \\ e_j &= -\eta_j \sigma_J k^2 \Delta p^2 / f_0^2 \end{aligned}\right\} \tag{3.18}$$

Since (3.17) is a linear equation in ω_j, we may assume that ω_j and ω_{j+1} are related as:

$$\omega_j = \alpha_j \omega_{j+1} + \beta_j + \gamma_j \omega_{JJ} \tag{3.19}$$

and

$$\omega_{j-1} = \alpha_{j-1} \omega_j + \beta_{j-1} + \gamma_{j-1} \omega_{JJ} \tag{3.20}$$

where α_j, β_j, γ_j are the constant coefficients to be determined. Substitution of (3.19) and (3.20) into (3.17) gives the following recursion formulae for α_j, β_j, γ_j.

$$\alpha_j = -c_j/(a_j \alpha_{j-1} + b_j)$$

$$\beta_j = (d_j - a_j \beta_{j-1})/(a_j \alpha_{j-1} + b_j) \qquad (3.21)$$

$$\gamma_j = (e_j - a_j \gamma_{j-1})/(a_j \alpha_{j-1} + b_j)$$

We can calculate α_j, β_j, γ_j for $j = 2$, JMAX, if we know their values for $j = 1$.

The upper boundary condition on ω determines α, β, γ for $j = 1$

For $\omega = 0$ at $p = 0$, i.e., $j = 1$

we get $\alpha_1 = 0$

$\beta_1 = 0$

$\gamma_1 = 0$

Now, we can calculate α_j, β_j, γ_j using (3.21).

In order to calculate ω for $j = 2$, JJ from (3.19), we need the boundary condition at j = JMAX. We shall consider two types of boundary conditions:

i) $\omega = 0$ at j = JMAX

ii) $\omega = \omega_E$ at j = JMAX

The boundary condition (i) would correspond to wave-CISK heating without Ekman pumping, and (ii) would correspond to wave-CISK heating with Ekman pumping. We have made the calculations for both these cases and compared the results in the next section.

For $\omega = 0$ at $j = JMAX$ we get from (3.19)

$$\omega_{JJ} = \beta_{JJ} \Big/ \left(1 - \gamma_{JJ}\right)$$

For $\omega = \omega_E$ at $j = JMAX$ we get from (3.19)

$$\omega_{JJ} = \frac{\beta_{JJ} + \alpha_{JJ}\, \omega_E}{\left(1 - \gamma_{JJ}\right)}$$

Then, we can calculate ω for $j = 2$ to $\left(JJ-1\right)$ from (3.19).

The numerical procedure to integrate (3.6) and (3.7), and to calculate the phase speeds and the growth rates, is the same as that described in Chapter 2.

3.4 Growth Rate versus Wavelength

Figure 3.6 displays plots of the growth rate versus wavelength for the six η profiles given in Figure 3.3 and Figure 3.4. The phase speed of the most unstable mode is also given in the same diagram and is labeled as C_R. The parameterization of cumulus heating for these calculations was of the Ekman-CISK type in which heating was assumed to be proportional to the Ekman pumping. Figure 3.7 shows the results for wave-CISK type heating, in which heating was assumed to be proportional to the vertical velocity at 900 mb, and the lower boundary condition for the vertical velocity was the Ekman pumping. When the heating was confined only up to 600 mb and $\alpha = 2$, the values of the growth rates for the η''' profile became very large for the wavelengths shorter than 2000 km. This may be seen from the lower panel of Figure 3.6. When the lower boundary condition for the vertical velocity was the Ekman pumping, and the heating was as-

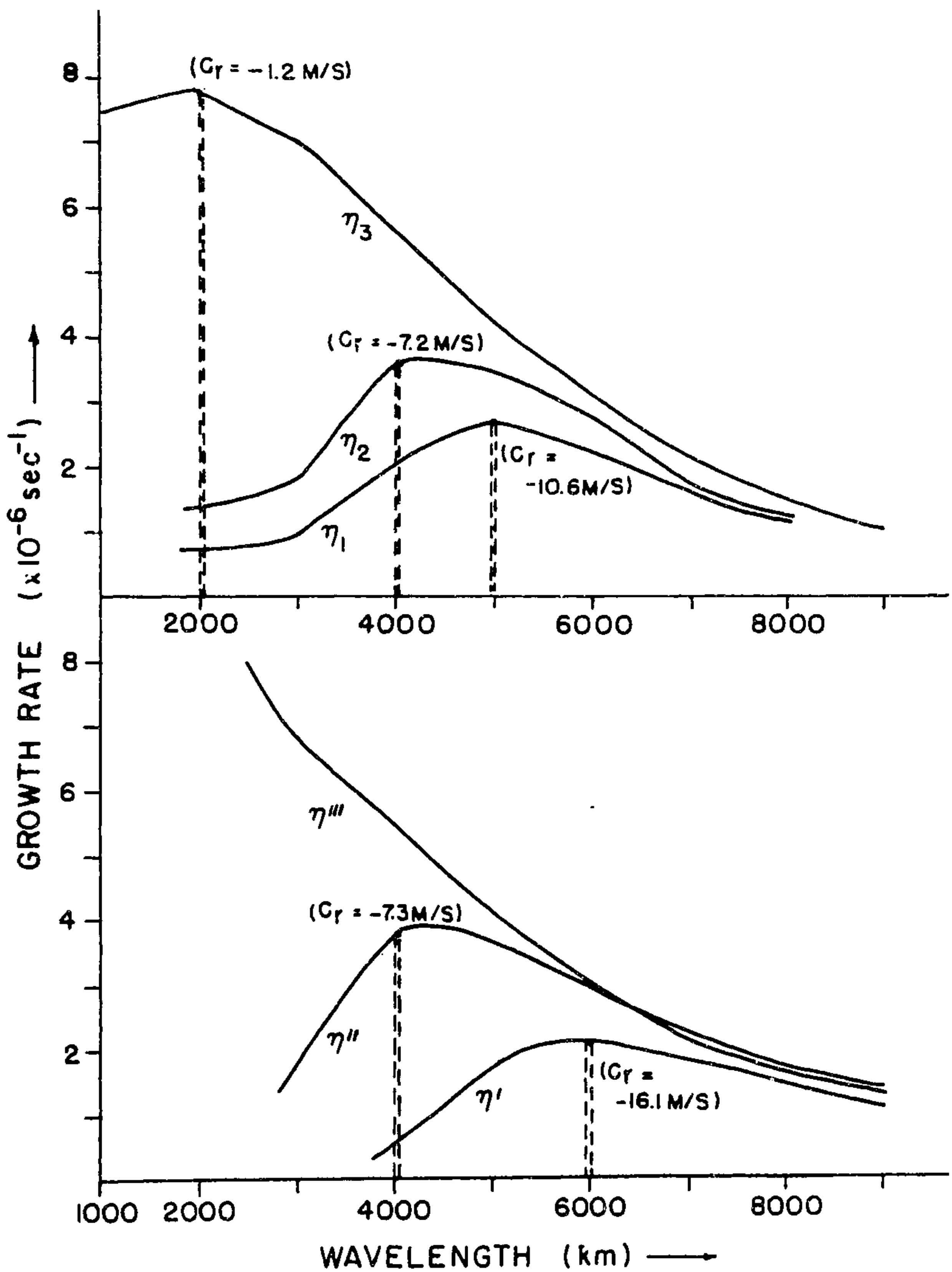

Figure 3.6 Growth rate versus wavelength for Ekman-CISK type heating. Labels η_1, η_2, η_3, η', η'', η''' denote the vertical distribution function and C_r is the phase speed for the most unstable mode.

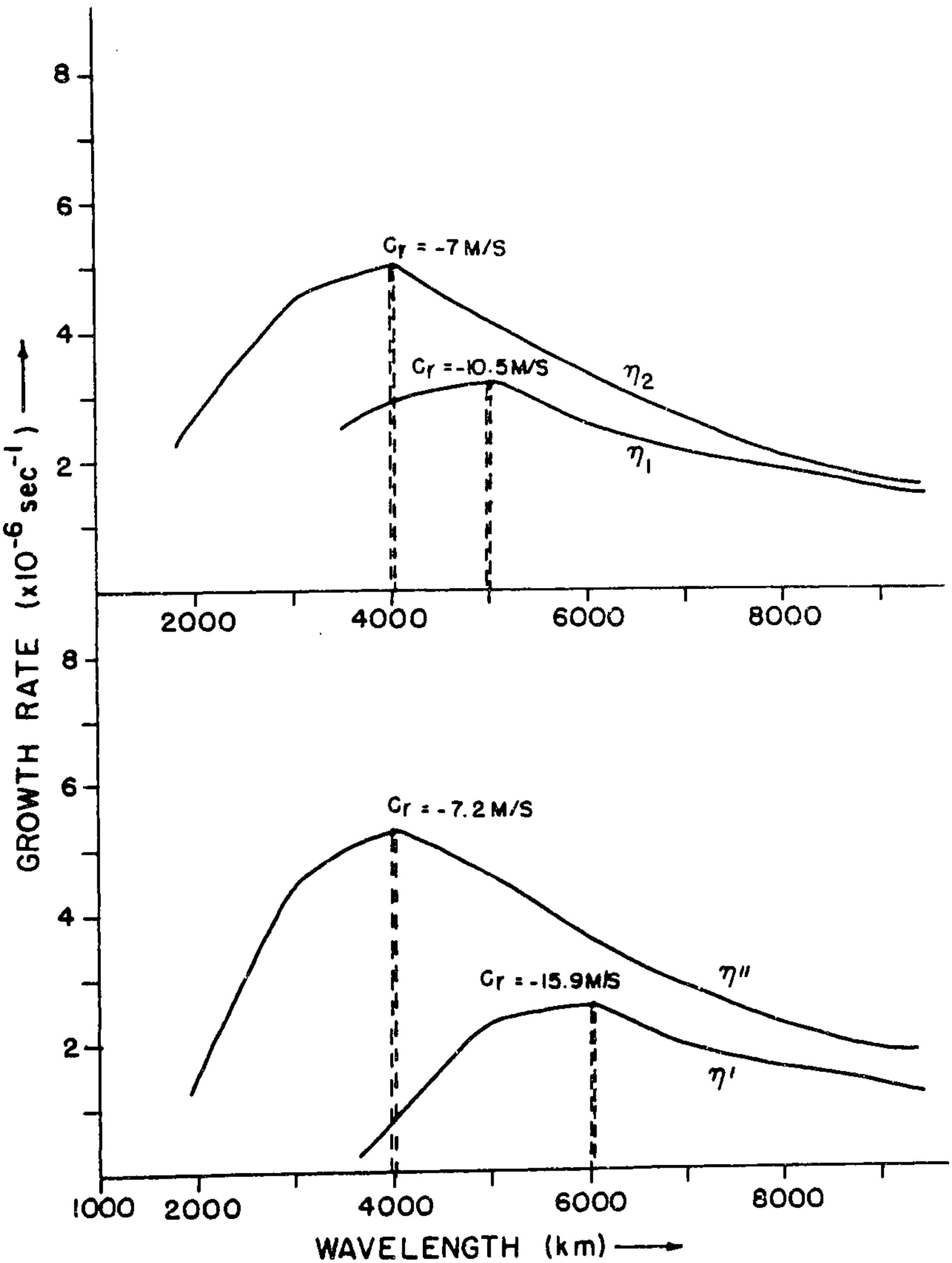

Figure 3.7 Same as Figure 3.6 for wave-CISK type heating.

sumed to be proportional to the vertical velocity at 900 mb, the values of the growth rates for wavelengths shorter than 2000 km became extremely large. In Figure 3.7, we have presented the results for the profiles $\eta_1, \eta_2, \eta', \eta''$ only.

Figure 3.8 gives the vertical structure (amplitude and phase) of Ψ and W for the most unstable modes shown in the upper panel of Figure 3.6, for the profiles η_1, η_2, η_3. The vertical structures of the most unstable modes for the profiles η', η'', η''' was similar to the ones given in Figure 3.8 for η_1, η_2, η_3, respectively, and therefore, are not shown separately.

It may be seen from Figure 3.6 and Figure 3.7 that the horizontal scale of the fastest growing perturbation increases with vertical depth of the atmospheric layer undergoing cumulus heating. This is in accordance with the concept of the Rossby radius of deformation in the theory of geostrophic adjustment, in which the scales of the horizontal and the vertical circulations are interrelated through stratification and rotation. By increasing the depth of the heated layer of the atmosphere, we are effectively increasing the vertical scale of the perturbation and therefore, increasing the corresponding horizontal scale.

The westward phase speed of the most unstable mode also increases with an increase in horizontal wavelength. The perturbations of longer wavelengths have corresponding larger vertical scales. Therefore, the steering level is higher. Since the vertical structure of the zonal flow is such that the speed of the easterlies increases with height, the westward phase speed of these perturbations is also greater.

It may also be seen from Figure 3.6 and Figure 3.7 that the magnitude of the growth rate is larger for those η profiles that provide heating to the smaller vertical depths of the atmosphere. One of the primary reasons for this result is the constraint imposed by the consistency condition (3.16). In this formulation, the vertically integrated total heating is kept constant for all η profiles. Therefore, the magnitude of the rate of heating is larger for those η profiles that provide heating to the smaller vertical depths of the atmosphere. This may be seen from Figure 3.4, in which $\alpha = 1.4$ for η'' and $\alpha = 2$ for η'''.

Since the horizontal scale of the most unstable perturbations decreases with vertical depth of the heated layer, heating per effective unit mass is increased for those η profiles that provide heating to the smaller vertical depths of the atmosphere.

Intercomparison of the upper and the lower panels of Figure 3.6 shows that the nature of the growth rate versus wavelength curves remains the same for both the constant η and the variable η profiles. The heating realized under the assumption of a constant η profile may be considered as equivalent to the heating provided by a non-entraining deep cloud. The variable η profile was determined from the observed vertical distribution of heating in a real synoptic situation, which may have a combination of deep and shallow clouds. The results of the instability analysis remain the same for the case of deep and shallow clouds, as for the case of deep clouds only, perhaps because the heating is provided mainly by deep clouds and the chief role of shallow clouds is to detrain moisture and liquid water into lower layers.

Figure 3.6 and Figure 3.7 also demonstrate that the shape of the growth rate versus wavelength curves is qualitatively the same for both the Ekman-CISK type and the wave-CISK type of heating. However, in either case, the main difference in the results occurs with change of the vertical distribution function used for cumulus heating.

Figure 3.8 shows that the vertical structure of the most unstable modes also depends upon the vertical distribution function for cumulus heating. The maximum amplitudes of ψ' and ω' for the η_1 profile occur at a higher level than those for the η_3 profile. In either case, there is no appreciable phase shift in the vertical. Such vertical structure is consistent with the vertical scales, steering levels, and westward phase speeds, of these perturbations.

Figure 3.9 displays the plots of growth rate versus wavelength for the η_1 profile for the wave-CISK type heating. The upper curve was obtained when the lower boundary condition upon the vertical velocity was given by the Ekman pumping; the lower curve was obtained when the vertical velocity at the lowest level was set equal to zero. The figure shows that when heating was made proportional to the vertical velocity at the top of the lowest layer, the magnitude of the growth rates was increased when Ekman pumping was added at the lowest level.

The results of this section have clearly demonstrated that the horizontal wavelength, phase velocity, growth rate, and the vertical amplitude structure of the most unstable mode depends upon the vertical distribution function for cumulus heating. It is, therefore, possible to simulate several kinds of tropical disturbances by choosing suitable profiles. For example, the most unstable mode in the case of the η_3 profile (see Fig. 3.6) has nearly the same horizontal wavelength (2000 km) and westward phase speed as a typical monsoon depression. However,

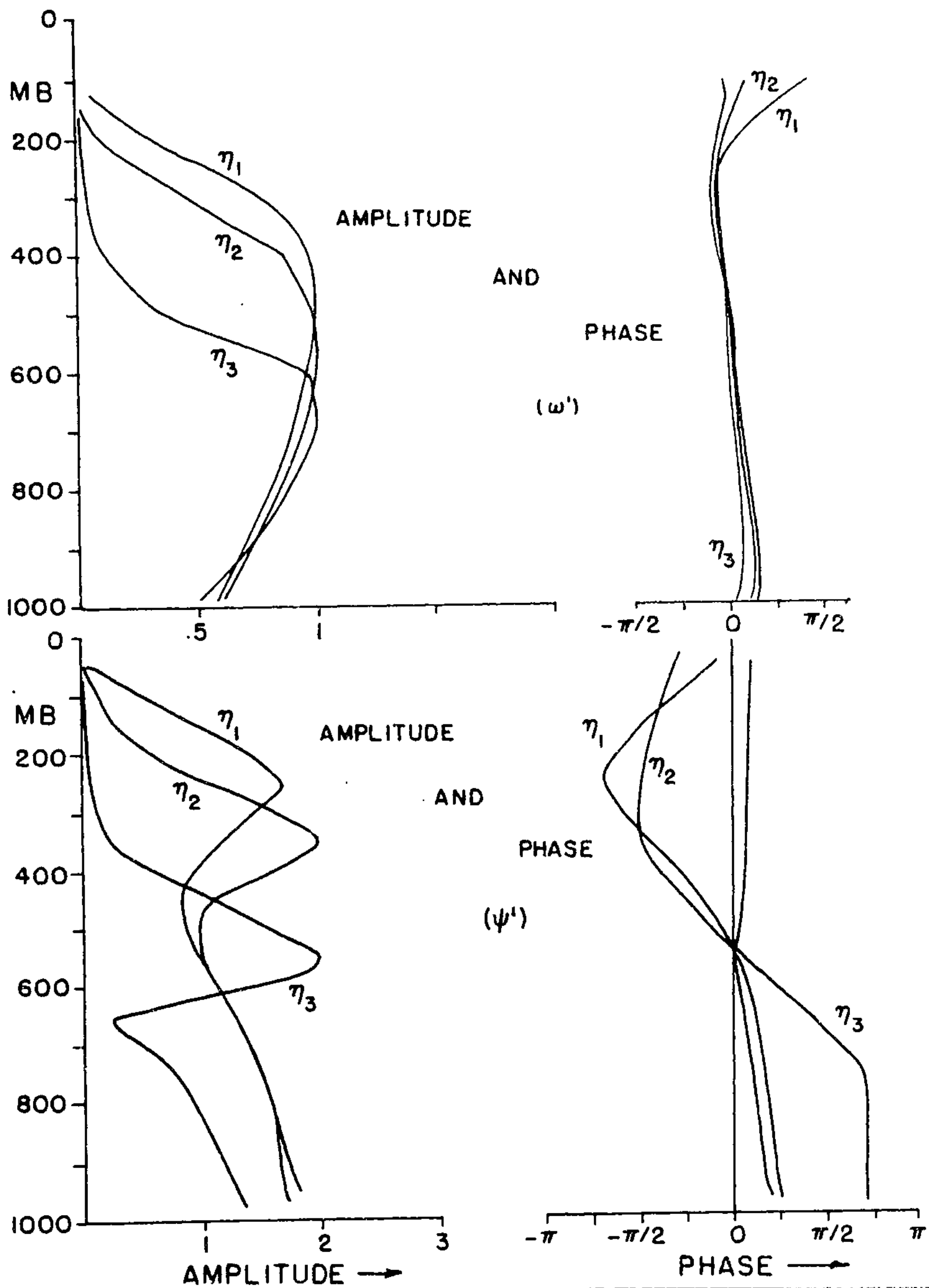

Figure 3.8 Amplitude and phase structure of (ω') and (ψ') for the most unstable modes of the-Ekman CISK type heating with the profiles η_1, η_2, η_3.

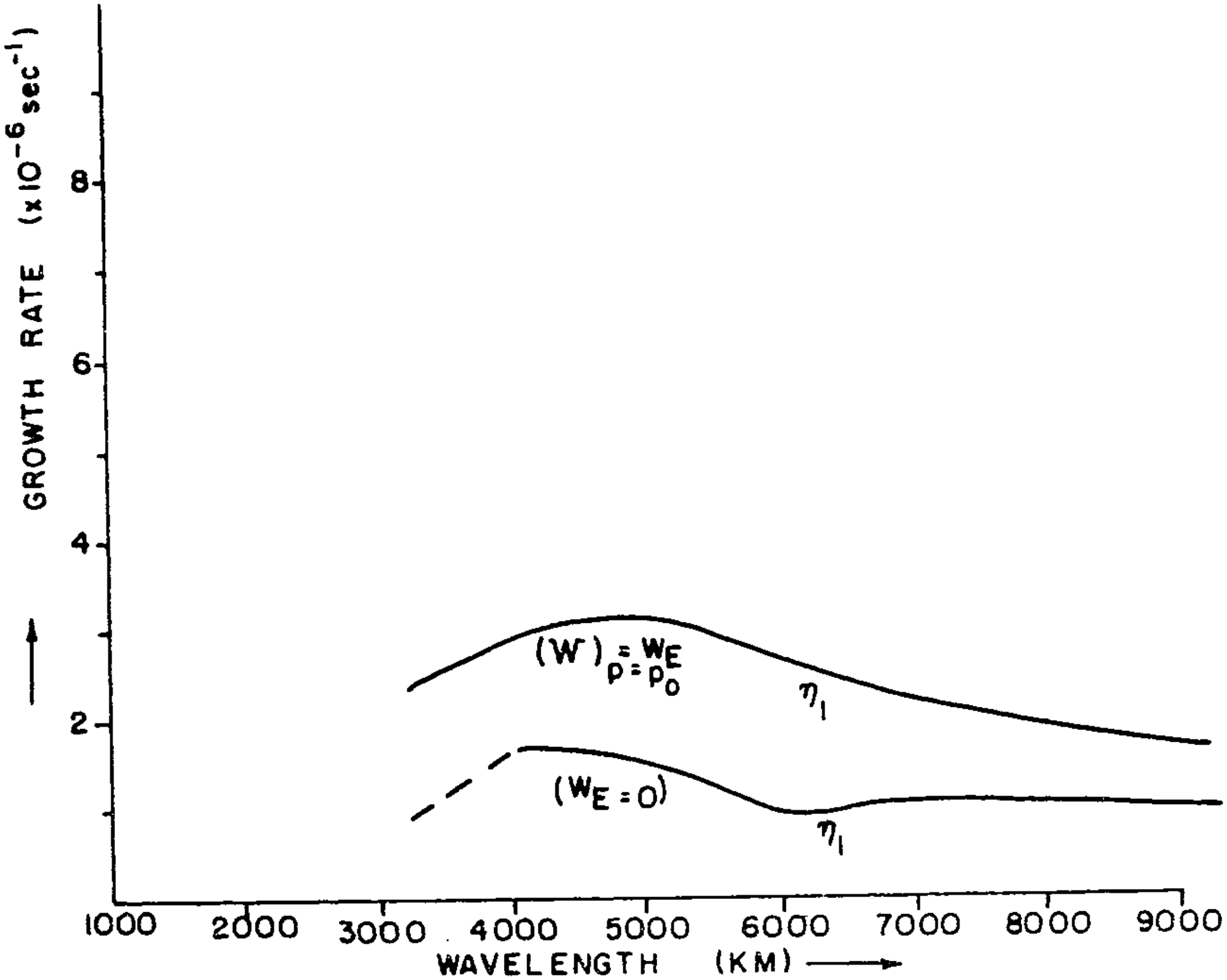

Figure 3.9 Growth rate versus wavelength for wave-CISK type heating with, and without, Ekman pumping for the profile η_1 .

the purpose of these calculations was not so much to simulate the growth of the monsoon depressions as to point out that one can simulate several kinds of tropospheric tropical/monsoon disturbances by choosing suitable η profiles. Since the choice of η is largely arbitrary, it points to the need of a theory for deducing the effects of the moist convection.

In the next section, we have applied the quasi-equilibrium assumption of Arakawa and Schubert (1974) to parameterize the effects of moist convection.

In all the analyses presented in this chapter, heating is considered a perturbation quantity and is assumed to have a sinusoidal variation in the longitudinal direction. This assumption is made to simplify the mathematical analysis of the linear stability problem. Earlier works by Yamasaki (1969), Hayashi (1970), Chang (1971), Koss (1975) and Lindzen (1974) also suffer from this shortcoming of linearizing the condensation process. In the observed synoptic waves, precipitation is mainly confined to the convergent regions of the wave. According to this assumption, heating occurs over half of the wavelength of the perturbation and an equal amount of cooling takes place over the remaining half of the wavelength. The effect of this assumption may be to enhance the rate of generation of available potential energy and therefore, to overestimate the magnitude of the growth rates.

In the next chapter also, heating has been assumed to be a linear perturbation variable. Consideration of the nonlinear character of condensation with the quasi-equilibrium assumption for parameterization of moist convection, makes the problem extremely complicated.

CHAPTER 4 QUASI-EQUILIBRIUM ASSUMPTION AND GROWTH OF DISTURBANCES

Assuming that a fraction, σ_c, of a unit synoptic area is covered with convective clouds, and that $\sigma_c \ll 1$, the equations for the mean dry static energy S ($= c_p \bar{T} + g \bar{z}$) and the mixing ratio q, may be written as (Arakawa and Schubert, 1974):

$$\rho \frac{\partial \bar{s}}{\partial t} = -\rho \bar{\underset{\sim}{v}} \cdot \nabla \bar{s} - \rho \bar{w} \frac{\partial \bar{s}}{\partial z} + M_c \frac{\partial \bar{s}}{\partial z} - L D \ell + \tilde{Q}_R + \sum_i Q_{Ri} \tag{4.1.1}$$

$$\rho \frac{\partial \bar{q}}{\partial t} = -\rho \bar{\underset{\sim}{v}} \cdot \nabla \bar{q} - \rho \bar{w} \frac{\partial \bar{q}}{\partial z} + M_c \frac{\partial \bar{q}}{\partial z} + D\left(\bar{q}^* - \ell - q\right) \tag{4.1.2}$$

where: bars (-) denote the average over unit synoptic area;

tildas ($\sim$) denote the average over the cloud-free environment;

and star (*) denotes the saturation value;

$\sum_i Q_{Ri}$ denotes the total radiative effects of the clouds;

L is the latent heat of condensation;

$\bar{q}^*$ is the saturation mixing ratio;

$\bar{\underset{\sim}{v}}$ is the mean horizontal velocity vector;

$\bar{w}$ is the mean vertical velocity such that:

$$\rho \bar{w} = M_c + \tilde{M} \tag{4.1.3}$$

where: M_c is the total mass flux in the clouds and

$\tilde{M}$ is the mass flux between the clouds;

D is the total detrainment from the clouds into the environment;

ℓ is the detrained liquid water.

If we define a size parameter λ for the clouds, we may denote the cloud mass flux M_c as:

$$M_c(z) = \int_0^{\lambda_D} m(z,\lambda)\, d\lambda \qquad (4.1.4)$$

where λ is the value of λ for the cloud which is detraining at the level z .

The mass flux $m(z,\lambda)$ at any level for the clouds of type λ may be given as:

$$m(z,\lambda) = m_B(\lambda)\, \eta(z,\lambda) \qquad (4.1.5.)$$

where $m_B(\lambda)$ is the mass flux in the base of the cloud of type λ and η prescribes the vertical profile of the mass flux (and depends upon the rates of entrainment and detrainment). The fractional rate of entrainment (assumed constant in z) is given by $\frac{1}{\eta}\frac{\partial \eta}{\partial z}$. Let us further assume that we identify a cloud type by its fractional rate of entrainment and that therefore:

$$\lambda = \frac{1}{\eta}\frac{\partial \eta}{\partial z} \qquad (4.1.6)$$

then

$$\eta = e^{\lambda(z-z_B)} \qquad \text{for } z_B \leqslant z \leqslant z_D(\lambda)$$
$$z > z_D \qquad (4.1.7)$$

where z_B is the height of the cloud base and $z_D(\lambda)$ is the level of vanishing bouyancy for the cloud type λ . It is further assumed that the clouds entrain for their whole depth and detrain only at the level of vanishing bouyancy. If h denotes the moist static energy ($h = c_pT + gz + Lq$), the value of h in a cloud at any level z may be given as:

$$h_c(z,\lambda) = \frac{1}{\eta(z,\lambda)}\left[h_c(z_B,\lambda) + \lambda \int \eta(z',\lambda)\,\bar{h}(z')\,dz'\right] \qquad (4.1.8)$$

where $h_c(z_B,\lambda)$ is the value of h_c at the cloud base ($z = z_B$). The equation for the budget of cloud moisture q_c and liquid water ℓ may be written as:

$$\frac{\partial}{\partial z}\left[\eta(z,\lambda)\left\{q_c(z,\lambda) + \ell(z,\lambda)\right\}\right] = \frac{\partial \eta(z,\lambda)}{\partial z}\;\bar{q}(z,\lambda) - \eta(z,\lambda)\,(\gamma) \qquad (4.1.9)$$

where γ is the rate of conversion of liquid water to precipitation.

It may be seen from (4.1.1) and (4.1.2) that the influence of the cloud ensemble, in modifying the large-scale fields $\bar{s}$ and $\bar{q}$, appears through the terms containing M_c and D. The heating in this system is provided by the term $M_c \frac{\partial \bar{s}}{\partial z}$, which may be viewed as the effect of adiabatic compression of the subsiding air in the cloud free region which is needed to compensate for the cloud mass flux. Alternatively, $M_c \frac{\partial \bar{s}}{\partial z}$ may be viewed as the adiabatic cooling of the ascending cloud parcels, which is just compensated by release of latent heat of condensation inside the cloud, and therefore, a measure of non-adiabatic heating due to condensation. The term $-\ell D L$ represents the cooling due to evaporation of the detrained liquid water. (Evaporation of falling rain has not been included here.)

$M_c \frac{\partial \bar{q}}{\partial z}$ represents the drying of the environment due to a downward mass flux and D ($\bar{q}^* - \ell - \bar{q}$) is the moistening of the environment due to detrainment of liquid water and moisture from the clouds.

This formulation highlights the importance of a spectrum of clouds needed to maintain the observed mean thermal and moisture structure (conditional instability) of the tropical atmosphere. Clouds of varying size have different levels of vanishing bouyancy. By detrainment, the clouds provide moisture to the environment, while the downward mass flux in the environment decreases the mixing ratio of the environment. Similarly, the thermal structure is maintained by the heating effect of $M_c \frac{\partial \bar{s}}{\partial z}$ and the cooling due to $-LD\ell$ and radiation.

The problem of parameterizing the effects of moist convection now consists of determining M_c, D, and ℓ. Using the spectral representation of the cloud ensemble and a simple cloud model, it may be seen from (4.1.4), (4.1.5) and (4.1.9) that the problem of parameterization is finally reduced to finding the mass flux at the cloud base $m_B(\lambda)$ as a function of λ.

Arakawa and Schubert proposed the concept of quasi-equilibrium between the destabilizing large-scale forcing and the stabilizing effects of the cumulus ensemble. We shall refer to this assumption as the quasi-equilibrium assumption and use the abbreviation QEA.

4.1 Parameterization of Moist-convection by Quasi-equilibrium Assumption

The time change of the kinetic energy of a cloud ensemble may be given as:

$$\frac{d}{dt}K(\lambda) = A(\lambda)\, m_B(\lambda) + \mathcal{D}(\lambda) \qquad (4.1.10)$$

where $K(\lambda)$ and $\mathcal{D}(\lambda)$ represent the kinetic energy and dissipation rate, respectively.

Arakawa and Schubert (1974) call $A(\lambda)$ the cloud work function, which is the kinetic energy generation per unit mass flux and is given by:

$$A(\lambda) = \int_{z_B}^{z_D(\lambda)} \frac{g}{c_p \overline{T}(z)} \eta(z,\lambda) \left\{ S_c(z,\lambda) - \overline{S}(z,\lambda) \right\} dz \qquad (4.1.11)$$

(for a comprehensive discussion, see Arakawa and Schubert (1974))

According to the quasi-equilibrium assumption:

$$\frac{dA}{dt} \approx 0 \qquad (4.1.12)$$

Substituting (4.1.11) into (4.1.12)

$$\frac{dA}{dt} = \left(\frac{dA}{dt}\right)_c + \left(\frac{dA}{dt}\right)_{L.S.}$$

where $\left(\frac{dA}{dt}\right)_c$ represents all the terms involving cloud mass flux and $\left(\frac{dA}{dt}\right)_{L.S.}$ represents the terms involving large-scale variables.

Equation (4.1.12) is found to be of the form:

$$\int_0^{\lambda_{max}} K(\lambda,\lambda')\, m_B(\lambda')\, d\lambda' + F(\lambda) = 0 \qquad (4.1.13)$$

where the Kernel, $K(\lambda,\lambda')$, is a measure of the stabilization of the cloud work function for type λ clouds through the modification of the environment by type λ' clouds, and $F(\lambda)$ is the large-scale forcing.

The solution of (4.1.13) gives us the spectrum of $m_B(\lambda)$, which in turn, determines M_c and D.

The quasi-equilibrium assumption (4.1.12) is based on the hypothesis that the time scale of the changes of large-scale forcing is much larger than the time scale over which the cumulus activity adjusts to a given large-scale forcing. Arakawa and Schubert have given observational evidence to support their assumption. They have shown that the work function, A, remains nearly constant.

Some remarks on the assumptions and limitations of QEA

i) It is assumed that $\sigma_c \ll 1$. This assumption may not be valid for the eyewall region of a hurricane.

ii) The cloud work function is determined only by the vertical thermal structure of the atmosphere. For phenomena such as squall lines and other types of rainbands, dynamical forcings are quite important. In such situations, the work function may have to be redefined.

iii) It is assumed that the clouds are entraining through their whole vertical depth and detraining only at the level of vanishing bouyancy. This is not true for real clouds, because entrainment and detrainment both take place through the whole cloud depth simultaneously. This assumption may not be very serious if we only consider a spectrum of clouds because clouds of different size will have different levels of detrainment.

iv) This parameterization scheme does not include the effects of evaporation of the falling rain. The cooling due to the evaporation of the falling rain may be an important factor in determining the thermal structure of the tropical disturbances.

v) The observational evidence for the constancy of the work function does not seem to be sufficient. More detailed data analysis for a larger variety of synoptic situations may be needed to establish the validity of this assumption. It is one of the unique characteristics of tropical disturbances that the temperature changes associated with them are quite small and therefore, very careful analysis of accurate observations are needed to detect the small changes.

vi) The application of QEA turns out to be equivalent to assuming $A=0$ (Arakawa and Mintz, 1974), which is analogous to some form of convective adjustment in which the computed cloud mass flux is the one which is needed to keep the atmosphere neutral.

vii) The uniqueness of the solution of the integral equation (4.1.13) is not guaranteed. Different spectral distributions of the cloud mass flux may imply quite different vertical distribtutions for the heating.

viii) A cloud type is characterized by only one parameter, namely λ .

In spite of the several limitations of the QEA parameterization, this scheme, for the first time, offers a rational closure hypothesis to determine the effects of a cumulus ensemble, from the large-scale variables and therefore, the application of this scheme merits discussion.

4.2 The Mathematical Model

The basic dynamical framework that we have used for the instability study consists of the quasi-geostrophic equations with the quasi-boussinesq approximation.

Following the notations of the earlier section, the model equations are:

The vorticity equation: $\left(\zeta = \frac{\partial v}{\partial x} - \frac{\partial u}{\partial y}\right)$

$$\frac{\partial \zeta}{\partial t} + \underset{\sim}{v} \cdot \nabla(\zeta + f) = \frac{f_0}{\rho} \frac{\partial}{\partial z}(\rho w) \tag{4.2.1}$$

The dry static energy equation: $\left(s = c_p \bar{T} + g \bar{z}\right)$

$$\rho \frac{\partial s}{\partial t} = -\underset{\sim}{v} \cdot \nabla s - w \frac{\partial s}{\partial z} + M_c \frac{\partial s}{\partial z} - L D \ell \tag{4.2.2}$$

The moist static energy equation: $\left(h = c_p \bar{T} + g z + L q\right)$

$$\rho \frac{\partial h}{\partial t} = -\underset{\sim}{v} \cdot \nabla h - w \frac{\partial h}{\partial z} + M_c \frac{\partial q}{\partial z} + D(h^* - h) \tag{4.2.3}$$

The continuity equation:

$$\nabla \cdot (\rho \underset{\sim}{v}) + \frac{\partial}{\partial z}(\rho w) = 0 \tag{4.2.4}$$

The hydrostatic equation:

$$\frac{\partial p}{\partial z} = -g\rho \tag{4.2.5}$$

We shall linearize the above system of equations with respect to a basic state in which the mean u, s, h, and p are the functions of y and z only and the perturbation quantities are functions of x, y, z, and t.

$$\left.\begin{aligned}
u &= \bar{U}(y,z) + u'(x,y,z,t)\\
v &= 0 + v'(x,y,z,t)\\
w &= 0 + w'(x,y,z,t)\\
M_c &= 0 + M_c'(x,y,z,t)\\
D &= 0 + D'(x,y,z,t)\\
S &= \bar{S}(y,z) + S'(x,y,z,t)\\
h &= \bar{h}(y,z) + h'(x,y,z,t)\\
p &= \bar{p}(y,z) + p'(x,y,z,t)
\end{aligned}\right\} \quad (4.2.6)$$

Here, the bar (-) denotes the mean state and the primes (/) denote the infinitesimal perturbations over that mean state.

Since $\quad u' = \dfrac{1}{\rho(z)\, f_0}\dfrac{\partial p'}{\partial y} \quad$ and $\quad v' = \dfrac{1}{\rho(z)\, f_0}\dfrac{\partial p'}{\partial x}$

we may put $\quad \zeta' = \nabla^2\psi' \quad$ where $\quad \psi' = \dfrac{p'}{\bar{\rho}\, f_0} \qquad (4.2.7)$

$$\nabla^2 = \left(\frac{\partial^2}{\partial x^2} + \frac{\partial^2}{\partial y^2}\right)$$

and $\quad \bar{\zeta}(y,z) = -\dfrac{\partial \bar{U}(y,z)}{\partial y} = -\bar{U}_y$

The condition that $\bar{V} = 0$, $\bar{W} = 0$ and $\bar{M}_c = 0$ implies that the basic state has no mean meridional circulations and no mean cloud mass flux. This assumption has been made to simplify the analysis. Vertical and meridional structure of the basic state, $\bar{U}$, $\bar{S}$, $\bar{h}$ is specified from the observed mean state of the atmosphere.

The linearized system of equations may be written as:

$$\frac{\partial}{\partial t}\left(\nabla^2\psi'\right) + \bar{U}\frac{\partial}{\partial x}\left(\nabla^2\psi'\right) + v'\left(\beta - \bar{U}_{yy}\right) = \frac{f_0}{\bar{\rho}}\frac{\partial W'}{\partial z} \qquad (4.2.8)$$

$$\bar{\rho}\frac{\partial s'}{\partial t} = -\bar{U}\frac{\partial s'}{\partial x} - v'\frac{\partial \bar{s}}{\partial y} + (M_c' - W')\frac{\partial \bar{s}}{\partial z} - LD'\ell \qquad (4.2.9)$$

$$\bar{\rho}\frac{\partial h'}{\partial t} = -\bar{U}\frac{\partial h'}{\partial x} - v'\frac{\partial \bar{h}}{\partial y} + (M_c' - W')\frac{\partial \bar{h}}{\partial z} + D'(\bar{h}^* - \bar{h}) \qquad (4.2.10)$$

$$\frac{\partial}{\partial z}\left(\frac{p'}{\bar{\rho}}\right) = \frac{g s'}{c_p \bar{T}} \qquad (4.2.11)$$

where $W' = \rho w'$ and $v' = \dfrac{\partial \psi'}{\partial x}$

Since $\psi' = \dfrac{p'}{\bar{\rho} f_0}$, we may use the hydrostatic relation (4.2.11) to eliminate the time-dependent terms from (4.2.8) and (4.2.9) and get a diagnostic equation for W'. In a quasi-geostrophic system, the diagnostic equation for vertical velocity gives that vertical velocity field which would be needed to maintain the quasi-geostrophic balance and the hydrostatic balance.

The equation for W' may be written as:

$$\frac{g}{c_p \bar{T}\bar{\rho}}\left[\nabla^2\left\{\bar{U}\frac{\partial s'}{\partial x} + v'\frac{\partial \bar{s}}{\partial y} + (W' - M_c')\frac{\partial \bar{s}}{\partial z} + LD'\ell\right\}\right]$$

$$-f_0\left[\frac{\partial}{\partial z}\left\{\bar{U}\frac{\partial}{\partial x}\nabla^2\psi' + v'(\beta - \bar{U}_{yy}) - \frac{f_0}{\bar{\rho}}\frac{\partial W'}{\partial z}\right\}\right] = 0 \qquad (4.2.12)$$

where $\nabla^2 = \dfrac{\partial^2}{\partial x^2} + \dfrac{\partial^2}{\partial y^2}$ and $\bar{U}_{yy} = \dfrac{\partial^2 u}{\partial y^2}$ (4.2.13)

Equations (4.2.8), (4.2.9), (4.2.10) and (4.2.12) are the four equations for the four variables ψ', s', h' and W'. By making use of the quasi-equilibrium assumption, we calculate M_c' and D' (which in turn determines ℓ) in terms of ψ', w', s', h' and the mean quantities $\bar{U}$, $\bar{s}$, $\bar{h}$ and $\bar{p}$, which finally closes the system.

4.2.1 Finite difference form of the linearized equations

For the three-layer model shown in Figure 4.1, the finite difference forms of (4.2.8), (4.2.9) and (4.2.10) may be written as:

$$\frac{\partial}{\partial t}\nabla^2\psi_1' = -\bar{U}_1\frac{\partial}{\partial x}\nabla^2\psi_1' - \frac{\partial\psi_1'}{\partial x}\left(\beta-\bar{U}_{1yy}\right) + \frac{f_0}{\rho_1\Delta z_1}\left(w_2'-w_0'\right) \tag{4.2.14}$$

$$\frac{\partial}{\partial t}\nabla^2\psi_3' = -\bar{U}_3\frac{\partial}{\partial x}\nabla^2\psi_3' - \frac{\partial\psi_3'}{\partial x}\left(\beta-\bar{U}_{3yy}\right) + \frac{f_0}{\rho_3\Delta z_3}\left(w_4'-w_2'\right) \tag{4.2.15}$$

$$\frac{\partial}{\partial t}\nabla^2\psi_5' = -\bar{U}_5\frac{\partial}{\partial x}\nabla^2\psi_5' - \frac{\partial\psi_5'}{\partial x}\left(\beta-\bar{U}_{5yy}\right) + \frac{f_0}{\rho_5\Delta z_5}\left(-w_4'\right) \tag{4.2.16}$$

$$\frac{\partial s_1'}{\partial t} = \frac{\left(M_2'-w_2'\right)\left(\bar{s}_2-\bar{s}_1\right)}{\rho_1\Delta z_1} - \bar{U}_1\frac{\partial s_1'}{\partial x} - \frac{\partial\psi_1'}{\partial x}\frac{\partial\bar{s}_1}{\partial y} \tag{4.2.17}$$

$$\frac{\partial s_3'}{\partial t} = \left\{\frac{\left(M_2'-w_2'\right)\left(\bar{s}_3-\bar{s}_2\right)+\left(M_4'-w_4'\right)\left(\bar{s}_4-\bar{s}_3\right)}{\rho_3\Delta z_3}\right\} - \frac{D_3\ell_3 L}{\rho_3\Delta z_3} - \bar{U}_3\frac{\partial s_3'}{\partial x} - \frac{\partial\psi_3'}{\partial x}\frac{\partial\bar{s}_3}{\partial y} \tag{4.2.18}$$

$$\frac{\partial s_5'}{\partial t} = \left\{\frac{\left(M_4'-w_4'\right)\left(\bar{s}_5-\bar{s}_4\right)-D_5\ell_5 L}{\rho_5\Delta z_5}\right\} - \bar{U}_5\frac{\partial s_5'}{\partial x} - \frac{\partial\psi_5'}{\partial x}\frac{\partial\bar{s}_5}{\partial y} \tag{4.2.19}$$

$$\frac{\partial h_1'}{\partial t} = \frac{\left(M_2'-w_2'\right)\left(\bar{h}_2-\bar{h}_1\right)}{\rho_1\Delta z_1} - \bar{U}_1\frac{\partial h_1'}{\partial x} - \frac{\partial\psi_1'}{\partial x}\frac{\partial\bar{h}_1}{\partial y} \tag{4.2.20}$$

$$\frac{\partial h_3'}{\partial t} = \left\{\frac{(M_2'-W_2')(\bar{h}_3-\bar{h}_2) + (M_4'-W_4')(\bar{h}_4-\bar{h}_3) + D_3(\bar{h}_3^*-\bar{h}_3)}{\rho_3 \Delta z_3}\right\}$$

$$-\bar{U}_3 \frac{\partial h_3'}{\partial x} - \frac{\partial \psi_3'}{\partial x}\frac{\partial \bar{h}_3}{\partial y} \tag{4.2.21}$$

$$\frac{\partial h_5'}{\partial t} = \left\{(M_4'-W_4')(\bar{h}_5-\bar{h}_4) + D_5(\bar{h}_5^*-\bar{h}_5)\right\}/\rho_3 \Delta z_3 - \bar{U}_5 \frac{\partial h_5'}{\partial x} - \frac{\partial \psi_5'}{\partial x}\frac{\partial \bar{h}_5}{\partial y} \tag{4.2.22}$$

Since the deep clouds would be assumed to be fully precipitating, we shall put $\ell_5 = 0$ in the above system of equations.

The finite difference form of the hydrostatic equation (4.2.11) becomes:

$$\psi_5' - \psi_3' = \alpha_5 S_5' + \alpha_3 S_3'$$

$$\psi_3' - \psi_1' = \alpha_3 S_3' + \alpha_1 S_1' \tag{4.2.23}$$

where

$$\alpha_j = \frac{\Delta z_j\, g}{2 C_p T_j f_0} \quad \text{for } j = 1, 3, 5$$

The finite difference form of (4.2.12) gives the following two equations for W_2' and W_4'.

$$A \nabla^2 W_2' + B \nabla^2 W_4' + C'' W_2' + D W_4' = \nabla^2 (RRR)$$

$$+\left\{(\beta - \bar{U}_{5yy})\frac{\partial \psi_5'}{\partial x} - (\beta - \bar{U}_{3yy})\frac{\partial \psi_3'}{\partial x}\right\} \tag{4.2.24}$$

$$A^{*}\nabla^{2}W_2' + B^{*}\nabla^{2}W_4' + C^{*}W_2' + D^{*}W_4' = -\frac{f_0 W_0'}{\rho_1 \Delta z_1}$$
$$+ \left\{\nabla^{2}(RRR') + (\beta - \bar{U}_{3yy})\frac{\partial \psi_3'}{\partial x} - (\beta - \bar{U}_{1yy})\frac{\partial \psi_1'}{\partial x}\right\} \quad (4.2.25)$$

where

$$A = \alpha'' A_{52} - \alpha' B_{42} - \alpha_3 S_{32} B_{22}'$$
$$B = \alpha'' A_{54} - \alpha' B_{44}' - \alpha_3 S_{32} B_{24}$$
$$C'' = (f_0/\rho_3 \Delta z_3)$$
$$D = \{-f_0/(\rho_3 \Delta z_3) - f_0/(\rho_5 \Delta z_5)\}$$
$$A^* = \alpha'' A_{52} - \alpha^* B_{22}' - \alpha_3 S_{43} B_{42}$$
$$B^* = \alpha'' A_{54} - \alpha^* B_{24} - \alpha_3 S_{43} B_{44}'$$
$$C^* = \{-f_0/(\rho_3 \Delta z_3) - f_0/(\rho_1 \Delta z_1)\}$$
$$D^* = (f_0/\rho_3 \Delta z_3)$$
$$\alpha^* = \alpha_1 S_{21} + \alpha_3 S_{32}$$
$$\alpha'' = (\alpha_3 \eta_{s,3} L \ell_3)/(\rho_3 \Delta z_3)$$
$$\alpha' = (\alpha_3 S_{43} + \alpha_5 S_{54})$$
$$B_{22}' = B_{22} - 1$$
$$B_{44}' = B_{44} - 1$$
$$S_{21} = (\bar{S}_2 - \bar{S}_1)/(\rho_1 \Delta z_1)$$
$$S_{32} = (\bar{S}_3 - \bar{S}_2)/(\rho_3 \Delta z_3)$$
$$S_{43} = (\bar{S}_4 - \bar{S}_3)/(\rho_3 \Delta z_3)$$
$$S_{54} = (\bar{S}_5 - \bar{S}_4)/(\rho_5 \Delta z_5)$$

$$RRR = \left(\overline{U}_5 \frac{\partial \psi_5'}{\partial x} - \overline{U}_3 \frac{\partial \psi_3'}{\partial x}\right) - \alpha' \mu_4 - \alpha_5 \left(\overline{U}_5 \frac{\partial S_5'}{\partial x} + \frac{\partial \overline{S}_5}{\partial y}\frac{\partial \psi_5'}{\partial x}\right)$$
$$-\alpha_3 \left(\overline{U}_3 \frac{\partial S_3'}{\partial x} + \frac{\partial \overline{S}_3}{\partial y}\frac{\partial \psi_3'}{\partial x}\right) + \alpha_3 S_{32}\mu_2 - \alpha'' A_{ss}$$

$$RRR' = \left(\overline{U}_3 \frac{\partial \psi_3'}{\partial x} - \overline{U}_1 \frac{\partial \psi_1'}{\partial x}\right) + \alpha^* \mu_2 - \alpha_3 \left(\overline{U}_3 \frac{\partial S_3'}{\partial x} + \frac{\partial \psi_3'}{\partial x}\frac{\partial \overline{S}_3}{\partial y}\right)$$
$$-\alpha_1 \left(\overline{U}_1 \frac{\partial S_1'}{\partial x} + \frac{\partial \psi_1'}{\partial x}\frac{\partial \overline{S}_1}{\partial y}\right) + \alpha_3 S_{43}\mu_4 - \alpha'' A_{ss}$$

(Expressions for $A_{s2}, A_{s4}, B_{22}, B_{24}, B_{42}, B_{44}, \mu_2, \mu_4, A_{ss}$ are given in Appendix A).

(4.2.24) and (4.2.25) are derived by substituting for M_2 and M_4 from (A-13) and A-14) of Appendix A.

4.3 Calculation of Cloud Mass Flux for a Discrete Model

For finite differencing the expression for the cloud work function $A(\lambda)$ and moist static energy in the cloud h_c, we have followed the scheme given by Arakawa and Mintz (1974) and Arakawa and Chao (1975).

The structure of a three-layer model used in this study is shown in Figure 4.1. It consists of three layers of depth Δz_1, Δz_3 and Δz_5 which are centred at the heights z_1, z_3 and z_5, respectively. ψ, S, h are defined at the levels 1, 3, 5 and W, M_c are defined at the levels 0, 2, 4, 6.

A cloud type is now identified by its level of detrainment and since we have only three layers in vertical, we can consider only two kinds of clouds. In the discrete model, the clouds have their base at z_2 and therefore, the cloud mass flux at the base of the cloud

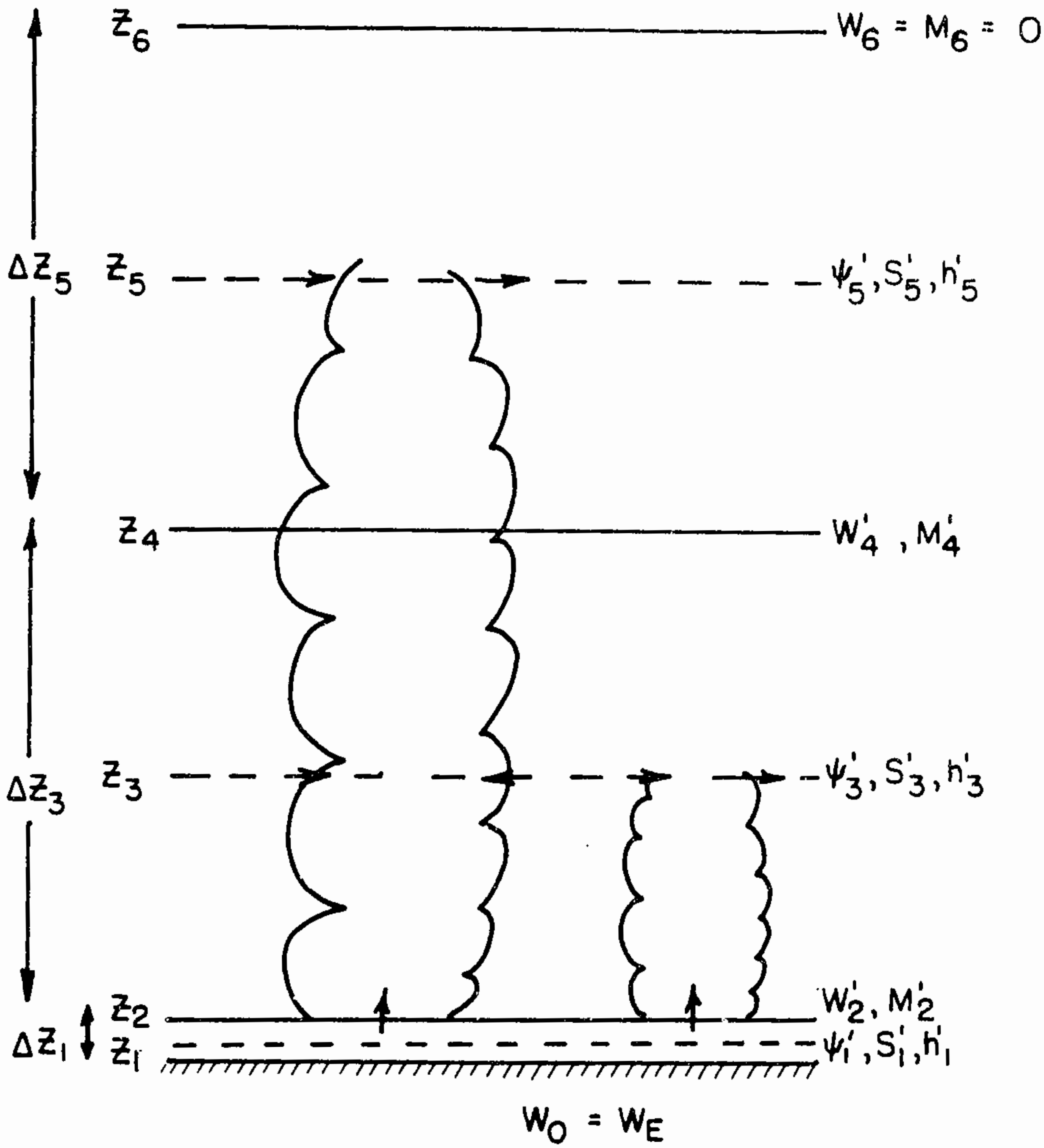

Figure 4.1 Schematic representation of the three-layer model with shallow and deep clouds.

$m_B(z_B, \lambda) = m_B(z_2, \lambda)$

Entrainment occurs at those levels where ψ , s , h are defined and detrainment occurs only at the top of the cloud. The two kinds of clouds that we consider in this model will be referred to as deep clouds and shallow clouds. The non-precipitating shallow clouds detrain at level z_3 . The amount of liquid water detrained at level z_3 is calculated from (4.1.9). The deep cloud is assumed to be fully precipitating and its detrainment level is at z_5 .

The height of the cloud base $z_B = z_2$ is assumed to be constant with time. Following the results of an observational study of Betts, et. al (1974), it has been assumed that the cumulus clouds have their "roots" in the mixed layer, and therefore, the moist static energy of the cloud at the cloud base ($h_c(z_B = z_2)$) is assumed to be equal to the moist static energy at z_1 .

i.e.,

$$h_c(z_B = z_2) = h(z = z_1) \tag{4.3.1}$$

The normalized mass flux $\eta(z, \lambda)$ for the cloud of type λ may be given as:

$$\eta(z, \lambda) = 1 + \lambda(z - z_2) \tag{4.3.2}$$

We shall use the subscript 's' for the shallow clouds, and 'd' for the deep clouds. The numbers 1,2,3,4,5,6 refer to z levels in the Figure 4.1.

For the three-layer discrete model, the expressions for $A(\lambda)$ (4.1.11) and $h_c(z, \lambda)$, (4.1.8) may be written as:

$$A(d) = \frac{g}{c_p \bar{T}_3 (1+\gamma_3)} \left[\eta_{d,4} h_{d,4} + \eta_{d,2} h_{d,2} - h_3^* (\eta_{d,4} + \eta_{d,2}) \right] \frac{\Delta z_3}{2}$$

$$\frac{g}{c_p \bar{T}_5 (1+\gamma_5)} \left[\eta_{d,4} \; h_{d,4} - h_5^* \eta_{d,4} \right] \frac{\Delta z_5}{2} \tag{4.3.3}$$

where $$\gamma_j = \frac{L}{c_p} \left(\frac{\partial q^*}{\partial T} \right)_{p_j} \qquad \text{for } j = 3, 5 \tag{4.3.4}$$

and $$S_c - S = (h_c - h^*) / (1 + \gamma) \tag{4.3.5}$$

$$A(s) = \frac{g}{c_p T_3 (1+\gamma_3)} \left(h_1 - h_3^* \right) \frac{\Delta z_3}{2} \tag{4.3.6}$$

$$h_{d,5} = \frac{1}{\eta_{d,5}} \left[h_{d,2} + (\eta_{d,4} - \eta_{d,2}) h_3 + (\eta_{d,5} - \eta_{d,4}) h_5 \right] \tag{4.3.7}$$

$$h_{d,4} = \frac{1}{\eta_{d,4}} \left[h_{d,2} + (\eta_{d,4} - \eta_{d,2}) h_3 \right] \tag{4.3.8}$$

$$h_{s,3} = \frac{1}{\eta_{s,3}} \left[h_{s,2} + (\eta_{s,3} - \eta_{s,2}) h_3 \right] \tag{4.3.9}$$

$$\eta_{s,3} = 1 + \lambda s \, (z_3 - z_2) \tag{4.3.10}$$

$$\eta_{d,j} = 1 + \lambda d \, (z_j - z_2) \quad ; \; j = 2, 3, 4, 5 \tag{4.3.11}$$

where $$h_{c,2} = h_{d,2} = h_1 \tag{4.3.12}$$

As discussed in section 4.1, $m_B(\lambda)$ is found by putting $\frac{\partial A(\lambda)}{\partial t} = 0$ which yields an integral equation (4.1.13). In the discrete model, we put $\frac{\partial A(s)}{\partial t} = 0$ and $\frac{\partial A(d)}{\partial t} = 0$ and we get two algebraic equations for which the two unknowns would be the mass flux at the base of the shallow clouds, $m_B(s)$ and the mass flux at the base of the deep clouds, $m_B(d)$.

For the purpose of instability analysis, we linearize the expressions for $A(\lambda)$ and $h_c(z,\lambda)$. To be consistent with the linearization used in the section (4.2), we make the following linearization.

$$A(\lambda) = 0 + A'(\lambda)$$

$$\lambda_s = 0 + \lambda_s'$$

$$\lambda_d = 0 + \lambda_d'$$

$$\left.\begin{aligned} h_j &= \bar{h}_j + h_j' \\ s_j &= \bar{s}_j + s_j' \\ h_{cj} &= \bar{h}_{cj} + h_{cj}' \end{aligned}\right\} j = 1 \text{ to } 6$$

Since the level of detrainment of the clouds is fixed at the levels z_3 and z_5 for the shallow and the deep clouds, respectively, and since s and h are being perturbed, it is necessary that λ_s and λ_d are also allowed to change. With a change in s' and h', the cloud ensemble readjusts its characteristic size to be consistent with its detrainment level. This is an additional assumption which is necessitated by the discreteness of the model. The alternative possibility of keeping the λ constant and varying the level of detrainment turns out to be very cumbersome in the discrete model because the calculation of λ itself requires a knowledge of the level of detrainment and z_D appears as upper limit of integration for the cloud work function.

We first compute λ_s and λ_d from the linearized forms of (4.3.9) and (4.3.7), respectively. Since the shallow and the deep clouds detrain at the levels z_3 and z_5, respectively,

$$h_{s,3} = h_3^* \tag{4.3.13}$$

$$h_{d,5} = h_5^* \tag{4.3.14}$$

From (4.3.9), (4.3.10), (4.3.12) and (4.3.13) we get:

$$\lambda_s = \frac{h_1 - h_3^*}{(h_3^* - h_3)(z_3 - z_2)} \tag{4.3.15}$$

From (4.3.7), (4.3.11), (4.3.12) and (4.3.14) we get:

$$\lambda_d = \frac{h_1 - h_5^*}{\left\{ h_5^*(z_5 - z_2) + h_3(z_4 - z_2) - h_5(z_5 - z_4) \right\}} \tag{4.3.16}$$

Knowing λ_s and λ_d, we may compute $\eta_{s,j}$ and $\eta_{d,j}$ from (4.3.10) and (4.3.11), respectively.

For nonprecipitating shallow clouds, we may now calculate (the liquid water detrained at level z_3) from the finite difference form of (4.1.9).

$$\eta_{s,3}(q_{s,3} + l_{s,3}) - \eta_{s,2}(q_{s,2} + l_{s,2}) = (\eta_{s,3} - \eta_{s,2})q_3 \tag{4.3.17}$$

Since $q_{s,2} = q_1$ and $\ell_{s,2} = 0,$

$$\ell_{s,3} = \left[\frac{\bar{q}_1 + \lambda_s (z_3 - z_2)\bar{q}_3}{\eta_{s,3}} - \bar{q}_3^{*} \right] \tag{4.3.18}$$

By equating the time derivative of the perturbation cloud work function equal to zero, we get the following two equations for the shallow and the deep clouds, respectively:

$$\frac{\partial}{\partial t} A'(s) = 0 \quad \Rightarrow \quad \frac{\partial h_1'}{\partial t} - \frac{\partial h_3^{*'}}{\partial t} = 0 \tag{4.3.19}$$

$$\frac{\partial A'(d)}{\partial t} = 0 \quad \Rightarrow \quad R_1 \frac{\partial h_1'}{\partial t} + R_2 \frac{\partial h_3'}{\partial t} + R_3 \frac{\partial h_{d,4}'}{\partial t} + R_4 \frac{\partial h_5^{*'}}{\partial t} + R_5 \frac{\partial \lambda_D}{\partial t} = 0 \tag{4.3.20}$$

where
$$\left.\begin{aligned} R_1 &= \frac{g\,\Delta z_3}{c_p T_3 (1+\gamma_3)\Delta z_5}, \quad R_2 = -R_1(1+\eta_{d,4}) \\ R_3 &= \eta_{d,4} R_1, \quad R_4 = \frac{-g\,\eta_{d,4}}{c_p T_5 (1+\gamma_5)} \end{aligned}\right\} \tag{4.3.21}$$

$$R_5 = \left[\frac{g\,\Delta z_3}{c_p T_3 (1+\gamma_3)\Delta z_5} \left\{ \bar{h}_{d,4} - \bar{h}_3^{*} \right\} + \frac{g}{c_p T_5 (1+\gamma_5)} \left\{ \bar{h}_{d,4} - \bar{h}_5^{*} \right\} \right] \frac{\partial \eta_{d,4}}{\partial \lambda_d}$$

$$\frac{\partial h_{d,4}'}{\partial t} = \left\{ \frac{\partial h_1'}{\partial t} + (\eta_{d,4} - \eta_{d,2}) \frac{\partial h_3'}{\partial t} + \frac{\partial \eta_{d,4}}{\partial \lambda_d} (\bar{h}_3 - \bar{h}_{d,4}) \frac{\partial \lambda_D}{\partial t} \right\} \frac{1}{\eta_{d,4}} \tag{4.3.22}$$

$$\frac{\partial \lambda_d}{\partial t} = \frac{\frac{\partial h_1'}{\partial t} + (\eta_{d,4} - \eta_{d,2})\frac{\partial h_3'}{\partial t} + (\eta_{d,5} - \eta_{d,4})\frac{\partial h_5'}{\partial t} - \eta_{d,5}\frac{\partial h_5^{*\prime}}{\partial t}}{\frac{\partial \eta_{d,5}}{\partial \lambda_D}(\bar{h}_5^* - \bar{h}_5) + \frac{\partial \eta_{d,4}}{\partial \lambda_D}(\bar{h}_5 - \bar{h}_3)} \quad (4.3.23)$$

Substituting (4.3.22) and (4.3.23) into (4.3.20) we get:

$$f_1 \frac{\partial h_1'}{\partial t} + f_2 \frac{\partial h_3'}{\partial t} + f_3 \frac{\partial h_3^{*\prime}}{\partial t} + f_4 \frac{\partial h_5'}{\partial t} + f_5 \frac{\partial h_5^{*\prime}}{\partial t} = 0 \quad (4.3.24)$$

where

$$\begin{aligned}
f_1 &= R_1 + R_3(1+R_6)/\eta_{d,4} + R_5 R_7 \\
f_2 &= R_3(\eta_{d,4} - \eta_{d,2})(1+R_6)/\eta_{d,4} + R_5(\eta_{d,4} - \eta_{d,2})R_7 \\
f_3 &= R_2 \qquad\qquad\qquad\qquad\qquad\qquad\qquad\qquad (4.3.25) \\
f_4 &= (\eta_{d,5} - \eta_{d,4})\left\{R_3 R_6/\eta_{d,4} + R_5 R_7\right\} \\
f_5 &= -\left\{\frac{\eta_{d,4}\, g}{c_p T_5(1+\gamma_5)} + \eta_{d,5}\left(R_3 R_6/\eta_{d,4} + R_5 R_7\right)\right\}
\end{aligned}$$

Time tendencies of perturbation quantities appearing in (4.3.19) and (4.3.24) may be obtained from the finite difference forms of (4.2.9) and (4.2.10). This would give us two equations from which we can find $m_B(s)$ and $m_B(d)$.

Recalling the definition of cloud mass flux (from (4.1.4) and (4.1.5)):

$$M_2 = m_B(s) + m_B(d) \tag{4.3.26}$$

and

$$M_4 = \eta_{d,4}\, m_B(d) \tag{4.3.27}$$

Since the shallow cloud detrains at the level Z_3, the cloud mass flux at the level Z_4 is due to the deep cloud only. Using (4.3.26), (4.3.27), (4.2.9), (4.2.10). (4.3.19) and (4.3.24) we get the following two equations: (Details of the derivations are given in Appendix A.)

$$m_B(s)\, K_{ss} + m_B(d)\, K_{sd} = F_s \tag{4.3.28}$$

$$m_B(s)\, K_{ds} + m_B(d)\, K_{dd} = F_d \tag{4.3.29}$$

(F_s and F_d correspond to the large-scale forcing $F(\lambda)$ of (4.3.13).)

where
$$K_{ss} = \frac{\bar{h}_2 - \bar{h}_1}{\rho_1 \Delta z_1} - \frac{(1+\gamma_3)(\bar{s}_3 - \bar{s}_2)}{\rho_3 \Delta z_3} + \frac{(1+\gamma_3)\,\eta_{s,3}\, L\, l_{s,3}}{\rho_3 \Delta z_3}$$

$$K_{sd} = \frac{\bar{h}_2 - \bar{h}_1}{\rho_1 \Delta z_1} - \frac{(1+\gamma_3)(\bar{s}_3 - \bar{s}_2)}{\rho_3 \Delta z_3} - \frac{(1+\gamma_3)\,\eta_{d,4}(\bar{s}_4 - \bar{s}_3)}{\rho_3 \Delta z_3}$$

$$K_{ds} = f_1 \frac{(\bar{h}_2 - \bar{h}_1)}{\rho_1 \Delta z_1} + f_2 \frac{(\bar{h}_3 - \bar{h}_2)}{\rho_3 \Delta z_3} + f_2\, \eta_{s,3} \frac{(\bar{h}_3^* - \bar{h}_3)}{\rho_3 \Delta z_3}$$
$$+ (1+\gamma_3)\, f_3 \frac{(\bar{s}_3 - \bar{s}_2)}{\rho_3 \Delta z_3} - \frac{f_3 (1+\gamma_3)\,\eta_{s,3}\, l_{s,3}\, L}{\rho_3 \Delta z_3}$$

$$K_{dd} = f_1\frac{(\bar{h}_2-\bar{h}_1)}{\rho_1 \Delta z_1} + f_2\frac{(\bar{h}_3-\bar{h}_2)}{\rho_3 \Delta z_3} + f_2 \eta_{d,4}\frac{(\bar{h}_4-\bar{h}_3)}{\rho_3 \Delta z_3}$$

$$+ f_3(1+\gamma_3)\frac{(\bar{S}_3-\bar{S}_2)}{\rho_3 \Delta z_3} + f_3(1+\gamma_3)\frac{(\bar{S}_4-\bar{S}_3)}{\rho_3 \Delta z_3} + f_4 \eta_{d,4}\frac{(\bar{h}_5-\bar{h}_4)}{\rho_5 \Delta z_5}$$

$$+ f_4 \eta_{d,5}\frac{(\bar{h}_5^*-\bar{h}_5)}{\rho_5 \Delta z_5} + f_5(1+\gamma_5)\eta_{d,5}\frac{(S_5-S_4)}{\rho_5 \Delta z_5} \quad (4.3.30)$$

$$F_s = \left\{\frac{\bar{h}_2-\bar{h}_1}{\rho_1 \Delta z_1} - (1+\gamma_3)\frac{(\bar{S}_3-\bar{S}_2)}{\rho_3 \Delta z_3}\right\}W_2' + \left[(1+\gamma_3)\frac{(\bar{S}_3-\bar{S}_4)}{\rho_3 \Delta z_3}\right]W_4'$$

$$+ \bar{U}_1 \frac{\partial h_1'}{\partial x} + \frac{\partial \bar{h}_1}{\partial y}\frac{\partial \psi_1'}{\partial x}$$

$$- (1+\gamma_3)\bar{U}_3 \frac{\partial S_3'}{\partial x} - (1+\gamma_3)\frac{\partial \bar{S}_3}{\partial y}\frac{\partial \psi_3'}{\partial x} \quad (4.3.31)$$

$$F_d = \left[f_1\frac{(\bar{h}_2-\bar{h}_1)}{\rho_1 \Delta z_1} - f_2\frac{(\bar{h}_3-\bar{h}_2)}{\rho_3 \Delta z_3} - f_3(1+\gamma_3)\frac{(\bar{S}_2-\bar{S}_3)}{\rho_3 \Delta z_3}\right]W_2'$$

$$+\left[f_2\frac{(\bar{h}_4-\bar{h}_3)}{\rho_3 \Delta z_3} + f_3(1+\gamma_3)\frac{(\bar{S}_4-\bar{S}_3)}{\rho_3 \Delta z_3} - f_4\frac{(\bar{h}_4-\bar{h}_5)}{\rho_5 \Delta z_5} - f_5(1+\gamma_5)\frac{(\bar{S}_4-\bar{S}_5)}{\rho_5 \Delta z_5}\right]W_4'$$

$$+ f_1\left(\bar{U}_1\frac{\partial h_1'}{\partial x} + \frac{\partial \bar{h}_1}{\partial y}\frac{\partial \psi_1'}{\partial x}\right) + f_2\left(\bar{U}_3\frac{\partial h_3'}{\partial x} + \frac{\partial \bar{h}_3}{\partial y}\frac{\partial \psi_3'}{\partial x}\right)$$

$$+ f_3(1+\gamma_3)\left(\bar{U}_3\frac{\partial S_3'}{\partial x} + \frac{\partial \bar{S}_3}{\partial y}\frac{\partial \psi_3'}{\partial x}\right) + f_4\left(\frac{\partial h_5'}{\partial x}\bar{U}_5 + \frac{\partial \bar{h}_5}{\partial y}\frac{\partial \psi_5'}{\partial x}\right)$$

$$+ f_5(1+\gamma_5)\left(\bar{U}_5\frac{\partial S_5'}{\partial x} + \frac{\partial \bar{S}_5}{\partial y}\cdot\frac{\partial \psi_5'}{\partial x}\right) \quad (4.3.32)$$

where (from (4.3.4) and (4.3.5))

$$\frac{\partial h_j^*}{\partial t} = (1+\gamma_j)\frac{\partial S_j'}{\partial t} \tag{4.3.33}$$

and

$$W_j = \bar{\rho}\, w_j'$$

Since K_{ss}, K_{sd}, K_{ds}, K_{dd} are the constants determined by the vertical thermal and moisture structure of the atmosphere, we may solve (4.3.28) and (4.3.29) for $M_B(s)$ and $M_B(d)$ in terms of F_s and F_d, which, in turn, are the functions of ψ', S', h' and the mean quantities $\bar{S}$, $\bar{h}$ and $\bar{U}$. This was the purpose of the parameterization scheme.

Solving (4.3.28) and (4.3.29) for $M_B(s)$ and $M_B(d)$, we get:

$$M_B(s) = \left\{ \begin{array}{l} \frac{\partial}{\partial x}\left(a_4 S_1' + a_5 S_3' + a_6 S_5' + a_7 h_1' + a_8 h_3' + a_9 h_5'\right) + \\ A_{S2} W_2' + A_{S4} W_4' + \frac{\partial}{\partial x}\left(a_1\psi_1' + a_2\psi_3' + a_3\psi_5'\right) \end{array}\right. \tag{4.3.34}$$

$$\begin{aligned} M_B(d) = {} & A_{D2}W_2' + A_{D4}W_4' + \frac{\partial}{\partial x}\left(b_1\psi_1' + b_2\psi_3' + b_3\psi_5'\right) \\ & + \frac{\partial}{\partial x}\left(b_4 S_1' + b_5 S_3' + b_6 S_5' + b_7 h_1' + b_8 h_3' + b_9 h_5'\right) \end{aligned} \tag{4.3.35}$$

where A_{S2}, A_{D2}, A_{S4}, A_{D4}, $a_j\,(j=1,9)$ and $b_j\,(j=1,9)$ are the constants of the mean state and are given in Appendix A.

Knowing $M_B(s)$ and $M_B(d)$, we can find M_2 and M_4 from (4.3.26) and (4.3.27):

$$
\left.\begin{aligned}
M_2 &= m_B(s) + m_B(d) \\
M_4 &= \eta_{d,4}\, m_B(d) \\
D_3 &= m_B(s)\, \eta_{s,3} \\
D_5 &= m_B(d)\, \eta_{d,5}
\end{aligned}\right\} \quad (4.3.36)
$$

We also have (the D_3, D_5 relations above)

where D denotes detrainment.

$\frac{\partial \bar{S}}{\partial y}$ is calculated from the thermal wind relation:

$$\frac{\partial \bar{S}(y,z)}{\partial y} = \frac{c_p f_0}{g}\left[\bar{U}(y,z)\frac{\partial \bar{T}(z)}{\partial z} - \bar{T}(z)\frac{\partial \bar{U}(y,z)}{\partial z}\right]$$

It has been assumed that the mean mixing ratio does not vary in the meridional direction. This implies that the meridional gradients of the moist static energy and the dry static energy are the same at any given level.

4.4 The Two-layer Model in a Resting Atmosphere

For a two-layer model shown in Figure 4.2, we may write (4.2.9). (4.2.10), (4.2.8), (4.2.11), as follows:

$$\frac{\partial s_1'}{\partial t} = (M_2' - W_2')\left(\frac{\bar{s}_2 - \bar{s}_1}{\rho_1 \Delta z_1}\right) - \bar{U}_1 \frac{\partial s_1'}{\partial x} - \frac{\partial \psi_1'}{\partial x}\frac{\partial \bar{s}_1}{\partial y} \quad (4.4.1)$$

$$\frac{\partial s_3'}{\partial t} = (M_2' - W_2')\left(\frac{\bar{s}_3 - \bar{s}_2}{\rho_3 \Delta z_3}\right) - \bar{U}_3 \frac{\partial s_3'}{\partial x} - \frac{\partial \psi_3'}{\partial x}\frac{\partial \bar{s}_3}{\partial y} \quad (4.4.2)$$

$$\frac{\partial h_1'}{\partial t} = (M_2'-W_2')\left(\frac{\bar{h}_2-\bar{h}_1}{\rho_1 \Delta z_1}\right) - \bar{U}_1 \frac{\partial h_1'}{\partial x} - \frac{\partial \psi_1'}{\partial x}\frac{\partial \bar{h}_1}{\partial y} \quad (4.4.3)$$

$$\frac{\partial h_3'}{\partial t} = (M_2'-W_2')\left(\frac{\bar{h}_3-\bar{h}_2}{\rho_3 \Delta z_3}\right) + D_3\left(\frac{\bar{h}_3^*-\bar{h}_3}{\rho_3 \Delta z_3}\right) - \frac{\partial \psi_3'}{\partial x}\frac{\partial \bar{h}_3}{\partial y} - \bar{U}_3 \frac{\partial h_3'}{\partial x} \quad (4.4.4)$$

$$\nabla^2\left(\frac{\partial \psi_1'}{\partial t}\right) = -\bar{U}_1 \frac{\partial}{\partial x}\nabla^2\psi_1' - \frac{\partial \psi_1'}{\partial x}(\beta - \bar{U}_{1yy}) + \frac{f_0}{\rho_1 \Delta z_1}(W_2'-W_0) \quad (4.4.5)$$

$$\nabla^2\left(\frac{\partial \psi_3'}{\partial t}\right) = -\bar{U}_3 \frac{\partial}{\partial x}\nabla^2\psi_3' - \frac{\partial \psi_3'}{\partial x}(\beta - U_{3yy}) + \frac{f_0}{\rho_3 \Delta z_3}(-W_2) \quad (4.4.6)$$

$$\psi_3' - \psi_1' = \alpha_1 S_1' + \alpha_3 S_3' \quad (4.4.7)$$

where α_1 and α_3 are defined in (4.2.23).

In a two-layer model, we can consider only one type of cloud. The cloud base is at Z_1 and the cloud top is at Z_3(see Fig. 4.2). The cloud is assumed to be fully precipitating and therefore, there is no cooling due to detrainment of liquid water.

Following the procedure described in section 4.3, we may find the expression for M_2 for a two-layer model.

It is found that:

$$M_2' = \eta W_2' + \frac{\partial}{\partial x}\left\{a_1 S_1' + a_2 h_1' + a_3 S_3' + a_4 h_3' + a_5 \psi_1' + a_6 \psi_3'\right\} \quad (4.4.8)$$

where η, $a_j (j=1,6)$ are the constants determined by $\bar{S}$, $\bar{h}$, $\bar{U}$

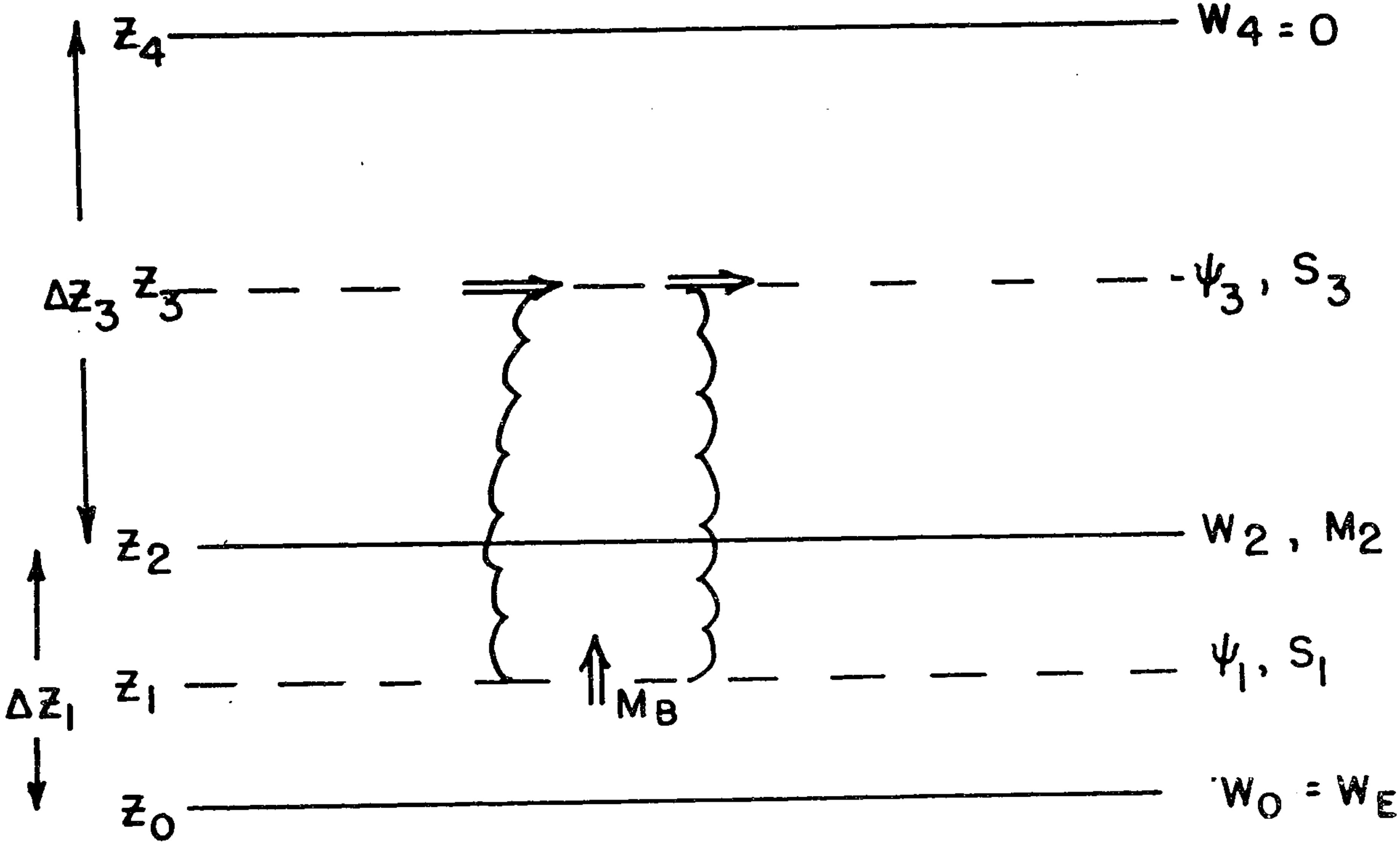

Figure 4.2 Schematic representation of the two-layer model with deep clouds.

and $\overline{p}$. Actual expression for these constants are given in Appendix B.

ψ_j' and W_j' are assumed to be of the form:

$$
\left.
\begin{aligned}
\psi_j' &= \mathrm{Re}\left\{ \Psi_j \, e^{ik(x-ct)} \right\} \\
W_j' &= \mathrm{Re}\left\{ W_j \, e^{ik(x-ct)} \right\}
\end{aligned}
\right. \qquad (4.4.9)
$$

where Ψ_j , W_j and c are complex.

For $\overline{U_j} = 0$, $\frac{\partial \overline{S}}{\partial y} = \frac{\partial \overline{h}}{\partial y} = 0$, (4.4.5), (4.4.6) may be written as:

$$
\left.
\begin{aligned}
k^3 i c \Psi_1 + i k \Psi_1 \beta &= \frac{f_0}{\rho_1 \Delta z_1} (W_2 - W_0) \\
k^3 i c \Psi_3 + i k \Psi_3 \beta &= \frac{f_0}{\rho_3 \Delta z_3} (-W_2)
\end{aligned}
\right\} \qquad (4.4.10)
$$

where W_0 is Ekman pumping at the lowest layer.

$$
\begin{aligned}
W_0 &= - \varepsilon_p k^2 \Psi_1 \\
\varepsilon_p &= \frac{\rho_0}{2} \sqrt{\frac{2\nu}{f_0}}
\end{aligned}
\qquad (4.4.11)
$$

Using (4.4.1), (4.4.2), (4.4.5), (4.4.6) and (4.4.7) an expression for W_2 may be given as:

$$
\begin{aligned}
&W_2 \left[-\frac{f_0}{\rho_3 \Delta z_3} - \frac{f_0}{\rho_1 \Delta z_1} + \overline{a} k^2 \right] \\
&\qquad = -\frac{f_0 W_0}{\rho_1 \Delta z_1} + i k \beta (\Psi_3 - \Psi_1)
\end{aligned}
\qquad (4.4.12)
$$

and $$M_2 = \eta W_2$$

(where η and $\bar{a}$ are the constants given in Appendix B.)

In order to simplify the algebra, we make the following assumptions:

$$\rho_1 \Delta z_1 = \rho_2 (z_3 - z_1) = \rho_3 \Delta z_3 = \rho_2 H \tag{4.4.13}$$

then, using (4.4.12), (4.4.10) may be written as:

$$\left.\begin{aligned} \Psi_1 (X + c) + \Psi_3 A &= 0 \\ \Psi_1 (-Y) + (B + c) \Psi_3 &= 0 \end{aligned}\right\} \tag{4.4.14}$$

(where c (complex) is the eigenvalue.)

$$\left.\begin{aligned} X &= \frac{\beta}{k^2} + \frac{f_0}{k^3 H} \left(\frac{e}{a} \right) \\ &\quad + i \left[\frac{f_0}{Hk^3} \left\{ k^2 \varepsilon_p + \frac{b}{a} \right\} \right] \\ Y &= \frac{f_0}{Hk^3} \left\{ \frac{e}{a} \right\} \\ A &= -Y \\ B &= \frac{\beta}{k^2} + \frac{f_0}{k^3 H} \left\{ \frac{e}{a} \right\} \end{aligned}\right\} \tag{4.4.15}$$

$$a = \frac{(\eta-1)\,k^2 N^2}{f^2} - \frac{2}{H^2}$$

$$b = \frac{k^2\,\varepsilon_p}{f_2\,H^2}$$

$$e = \frac{k\beta}{fH}$$

$$N^2 = \frac{g}{H^2}\left[\frac{(\bar{S}_2-\bar{S}_1)\,\Delta z_1}{2\,c_p\,T_1} + \frac{(\bar{S}_3-\bar{S}_2)\,\Delta z_3}{2\,c_p\,T_3}\right]$$

For nontrivial solutions of (4.4.14), the determinant of the coefficients must be equal to zero.

Equating the determinant of (4.4.14) equal to zero gives us the eigenvalue equation:

$$C = \left[-\frac{B+X}{2} \pm \sqrt{\left\{(B+X)^2 - 4(BX+AY)\right\}}\right]\frac{1}{2} \qquad (4.4.16)$$

where $C = C_r + i\,C_i$

For growing solutions to exist, kC_i should be greater than zero.

Substituting (4.4.15) into (4.4.16) we find that kC_i is always negative for $\eta < 1$.

Therefore, for $\eta < 1$, there are no growing modes.

Since $M_2 = \eta\,W_2$, $\eta < 1$ implies that convective heating is not enough to offset the adiabatic cooling and the perturbations do not grow.

For $\eta > 1$, we may have positive values of kC_i.

It turns out that kc_i is a maximum for

$$(\eta-1)N^2k^2H^2 = 2f^2$$

or
$$k^2 = \frac{2f^2}{H^2N^2(\eta-1)} \qquad (4.4.17)$$

and the maximum value of kc_i is ∞ .

(4.4.17) shows that the scale of maximum growth corresponds to the Rossby radius of deformation, provided the static stability parameter N^2 is scaled by ($\eta-1$) where η may be considered as the heating parameter.

If cumulus heating is assumed to be proportional to the mid-level vertical velocity in a two-layer model, the instability study yields an infinite growth rate for a finite scale. This is the reason why Israeli and Sarachik (1973) and Charney and Eliassen (1964) got infinite growth rates at finite scales. If the heating is assumed to be proportional to the Ekman pumping (Charney, 1971), the maximum growth occurs for the small scales. Since Charney and Eliassen (1964) assumed the heating to be proportional to a linear combination of Ekman pumping and internal vertical velocity at the middle level, they obtained both branches of the solution.

Since η is only a constant determined by the vertical structure of the atmosphere, we may treat η as a parameter and solve the eigenvalue equation (4.4.16) for various values of η .

Figure 4.3 gives the values of kc_i as a function of wavelength for different values of η . The numerical values of the con-

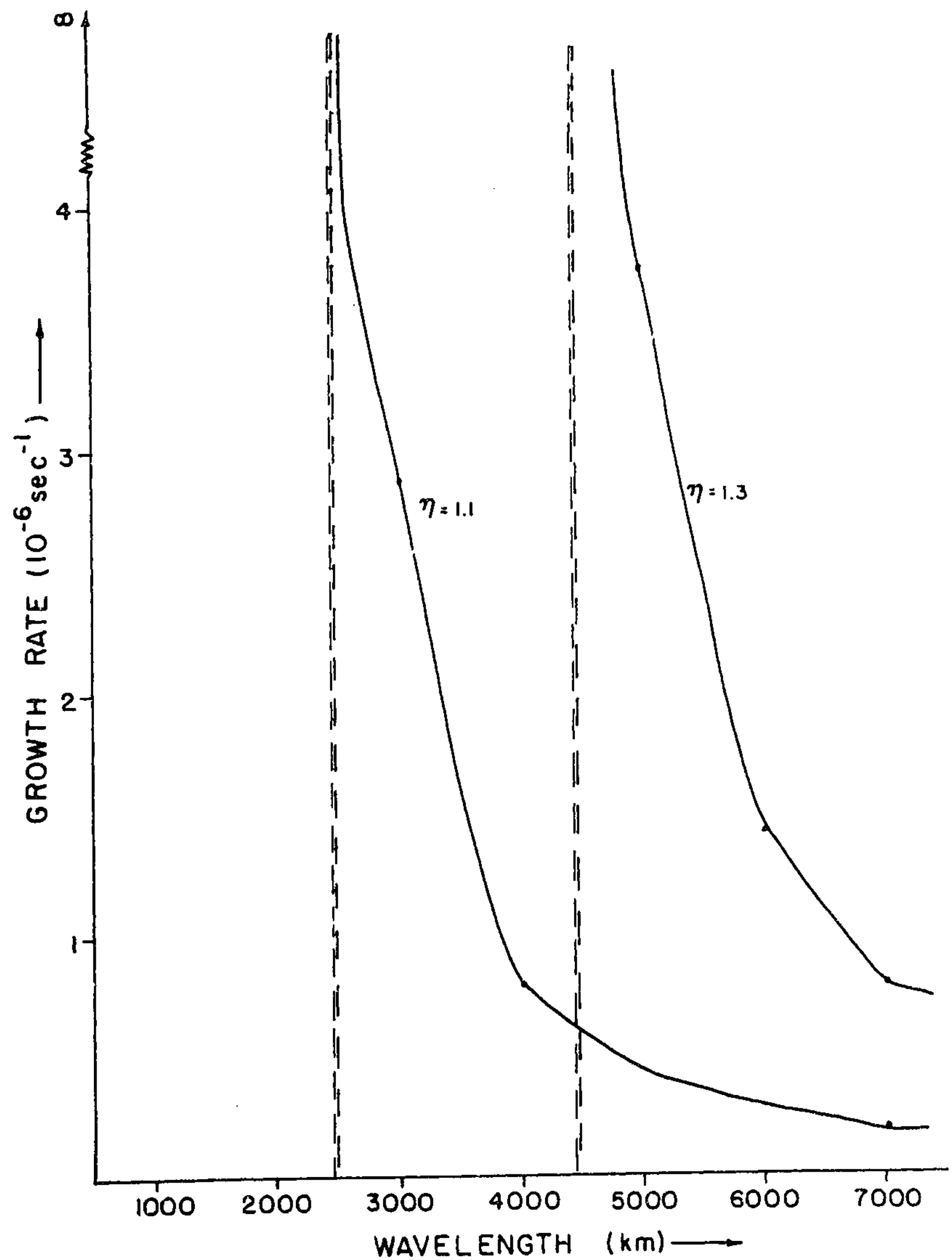

Figure 4.3 Growth rate versus wavelength for the two-layer model of resting atmosphere. η is the heating parameter.

stants used to compute (4.4.15) and (4.4.16) are taken as:

$$N^2 = 1.393 \times 10^{-4}\ \text{sec}^{-2}$$
$$H = 8.37\ \text{km}$$
$$f_0 = 5.566 \times 10^{-5}\ \text{sec}^{-1}$$

The wavelength of maximum growth rate increases as we increase the heating parameter, η, and then growth rate decreases with increase in the wavelength.

In order to get some insight into this phenomena, we may rewrite (4.4.10) as follows:

(By eliminating W_2 and putting $\beta = 0$ for convenience)

$$\left[1 - \frac{2 f_0^2}{k^2(\eta-1) H^2 N^2}\right] \frac{\partial}{\partial t}(\Psi_3 - \Psi_1) = \frac{f_0 \varepsilon_p}{\rho_1 \Delta z_1} \Psi_1 \qquad (4.4.18)$$

where ε_p is the Ekman pumping coefficient given by (4.4.11) and other notations have the same meaning as in the section 4.4.

We may see from the coefficient on the L.H.S. of (4.4.18) that for a given heating (η), stability (N^2) and vertical scale (H), there is a horizontal scale (k) for which the coefficients become zero and for that scale, the growth rate approaches infinity. That horizontal scale is determined by:

$$\frac{2 f_0^2}{k^2(\eta-1) H^2 N^2} = 1$$

$$\text{or} \qquad k^2 = \frac{2f^2}{H^2 N^2 (\eta - 1)}$$

which is the same as (4.4.17).

In a two-layer model, there is only one vertical scale and the horizontal scale associated with that vertical scale is the Rossby radius of deformation.

It may be seen from (4.4.12) that for $k^2 = \left[2f^2/H^2N^2(\eta-1)\right]$, W_2 becomes infinite and therefore, the assumptions of quasi-geostrophic and hydrostatic balance break down for this scale. From (4.4.1) and (4.4.2), it is seen that for $\eta > 1$, heating is associated with upward motion and cooling is associated with downward motion and the flow is therefore unstable.

The occurrence of an infinite growth rate for a finite scale is a consequence of the unrealistic modelling assumptions of only two layers in the vertical and the heating being proportional to the mid-level vertical velocity. In the three-layer case (see Section 4.6) the infinite growth rate at an intermediate wavelength is replaced by a finite maximum growth rate.

4.5 Charney's Two-layer Model of ITCZ with QEA

In order to explain the formation of the Inter-tropical Convergence Zone (ITCZ), Charney (1971) studied the growth of a zonally symmetric perturbation of a resting atmosphere on the rotating earth. The basic driving mechanism in this model was CISK, in which heating was parameterized in terms of the Ekman pumping. Since he took a two-layer model, the temperature equation was defined at the middle level and heating due to condensation was specified at that level. The nonlinear character of the condensation process was correctly accounted for by considering the heating only in a limited region of width (see Fig. 4.4) in which vertical velocity at the top of the boundary layer was upwards.

The purpose of this section is to repeat the instability analysis by Charney (1971) with the quasi-equilibrium assumption of Arakawa and Schubert to parameterize the heating due to condensation.

For a two-layer model (see Fig. 4.4), the nondimensional equations of the model may be written as (Charney, 1971):

$$\left.\begin{aligned}
&\frac{\partial u_1}{\partial t} - v_1 = 0 \quad ; \quad \frac{\partial u_2}{\partial t} - v_2 = 0 \\
&u_1 = -\frac{\partial \phi_1}{\partial y} \quad ; \quad u_2 = -\frac{\partial \phi_2}{\partial y} \\
&\frac{\partial v_1}{\partial y} + \omega_{3/2} - w_E = 0 \quad ; \quad \frac{\partial v_2}{\partial y} - \omega_{3/2} = 0 \\
&\frac{\partial}{\partial t}(\phi_2 - \phi_1) + \lambda^2(\omega_{3/2} - F\eta\,\omega_{3/2}) = 0
\end{aligned}\right\} \quad (4.5.1)$$

where λ^2 is the nondimensional radius of deformation. It may be noted that the only difference between Charney's equations and the above equations is that now the heating term involves the internal vertical velocity $\omega_{3/2}$ instead of the Ekman pumping, w_E.

From the above system of equations, we may derive separate equations for heating and non-heating regions.

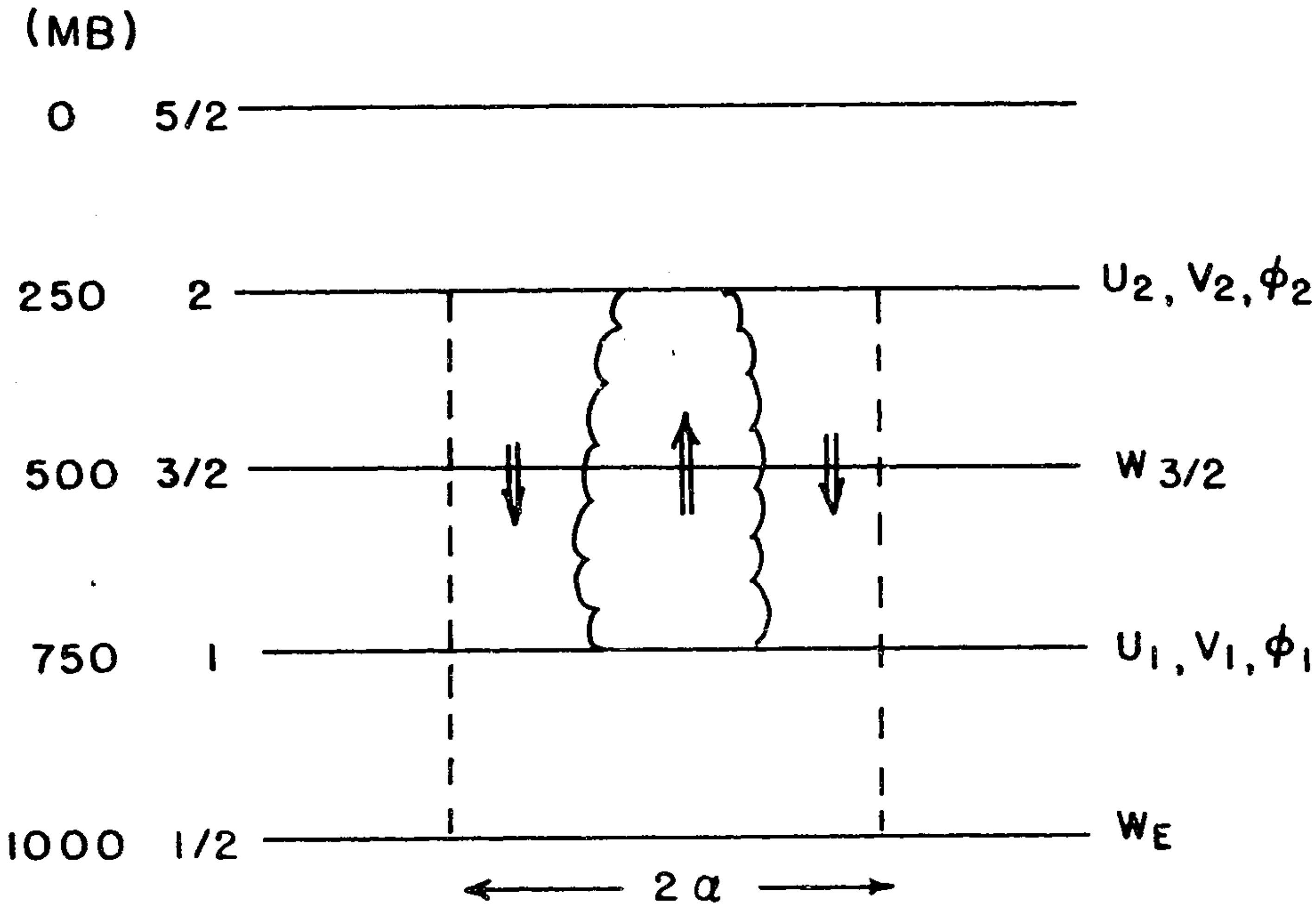

Figure 4.4 Schematic representation of the two-layer model of Charney (1971).

Assuming all dependent variables proportional to $e^{\frac{\sigma}{\sqrt{2}}t}$, we get:

$$\vartheta_{2yy} - \vartheta_2\left[\frac{2+2\sigma}{(1-\eta)(2+\sigma)}\right]\frac{1}{\lambda^2} = 0 \qquad \text{(for heating region)} \quad (4.5.2)$$

$$\vartheta_{2yy} - \vartheta_2\left[\frac{2+2\sigma}{2+\sigma}\right]\frac{1}{\lambda^2} = 0 \qquad \text{(for non-heating region)} \quad (4.5.3)$$

Continuity of mass (pressure) and temperature) at y = a gives the boundary conditions which give the following eigenvalue equation:

$$\frac{1}{\lambda_+}\tan\frac{a}{\lambda_+} = \frac{1}{\lambda_-} \qquad (4.5.4)$$

where

$$\left.\begin{aligned} \lambda_+ &= \left[\frac{(\eta-1)(2+\sigma)}{2+2\sigma}\right]^{1/2}\lambda \\ \lambda_- &= \left[\frac{2+\sigma}{2+2\sigma}\right]^{1/2}\lambda \end{aligned}\right\} \qquad (4.5.5)$$

From (4.5.4) we may see that:

$$\sigma = 0 \quad \text{for} \quad \frac{a}{\lambda} = \sqrt{\eta-1}\,\tan^{-1}\sqrt{\eta-1} \qquad (4.5.6)$$

and

$$\sigma = \infty \quad \text{for} \quad \frac{a}{\lambda} = \sqrt{\frac{\eta-1}{2}}\,\tan^{-1}\sqrt{\frac{\eta-1}{2}} \qquad (4.5.7)$$

So the growth rate is maximum (= ∞) for $\frac{a}{\lambda} = \sqrt{\frac{\eta-1}{2}}\,\tan^{-1}\sqrt{\frac{\eta-1}{2}}$

and decreases to zero for $\frac{a}{\lambda} = \sqrt{\eta-1}\ \tan^{-1}\sqrt{\eta-1}$.

For $\frac{a}{\lambda} > \sqrt{\eta-1}\ \tan^{-1}\sqrt{\eta-1}$, , σ is negative.

For $\frac{a}{\lambda} < \sqrt{\frac{\eta-1}{2}}\ \tan^{-1}\sqrt{\frac{\eta-1}{2}}$, we have no real solutions for σ .

Since η is a constant in a two-layer model, we may treat it as a parameter and solve (4.5.4) for different values of η . Figure 4.5 gives the plot of σ vs $\frac{a}{\lambda}$ for different values of η .

So far as the nature of the growth rate versus wavelength curve is concerned, these results are similar to the results obtained in the earlier section. The maximum growth rate (= ∞) is found for a finite scale and the growth rate decreases as the scale increases. The scale, at which the maximum growth rate occurs, increases with an increase in the heating parameter η .

The ratio of the half of the wavelength L of the most unstable mode (for sinusoidal heating case of section 4.4 and the size of the heating region 2a (see (4.5.7)) may be given as:

$$\frac{L/2}{a} \sim \frac{\pi\lambda\sqrt{\eta-1}}{\lambda\,(\eta-1)} = \frac{\pi}{\sqrt{\eta-1}}$$

Although η is greater than one, but not too much greater than one, it may be suggested that the assumption of sinusoidal nature of heating tends to overestimate the scale of the most unstable mode.

4.6 The Three-layer Model in a Resting Atmosphere

The model equations for a three-layer resting atmosphere are given by the set (4.2.14) through (4.2.25) with the following substitu-

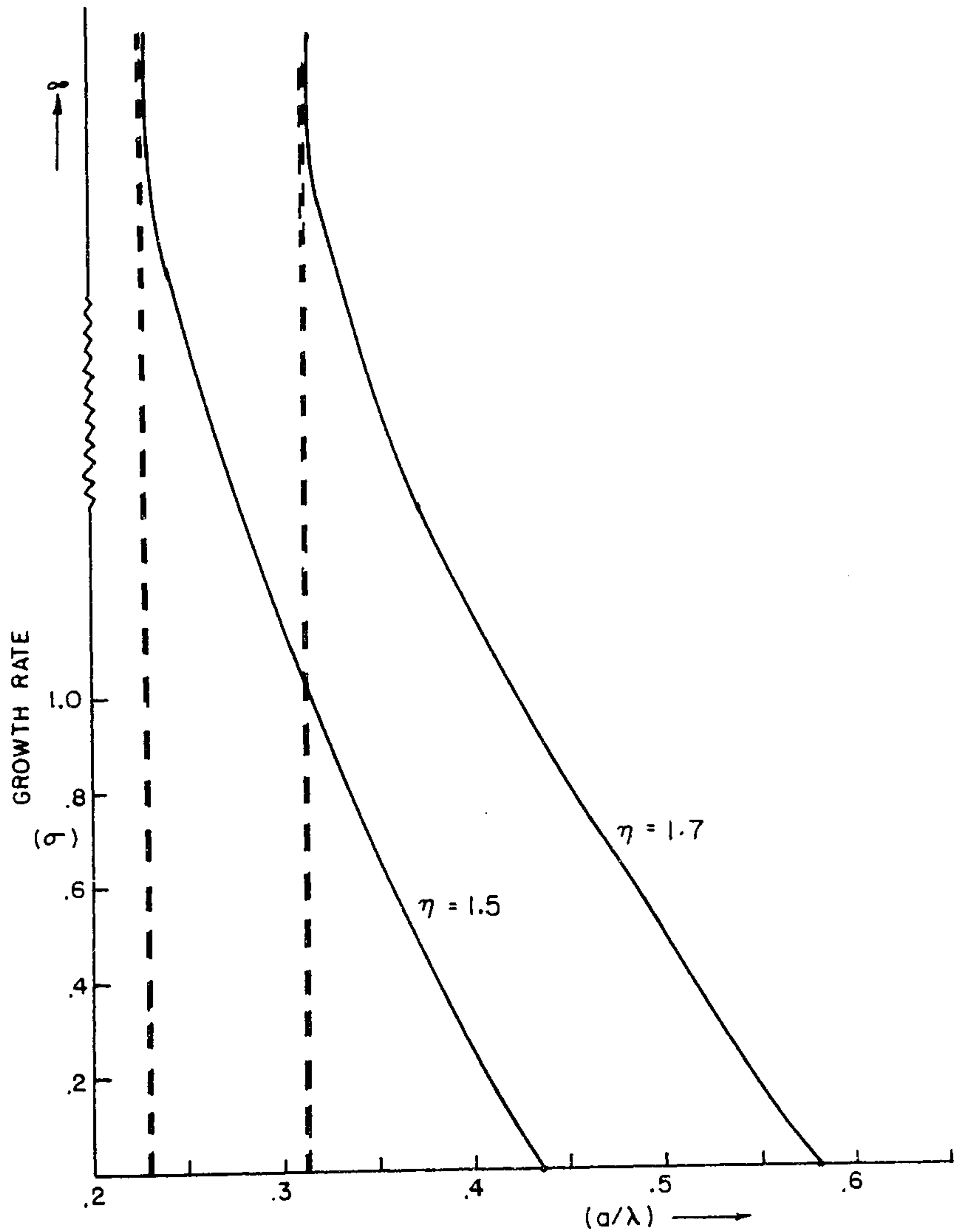

Figure 4.5 Growth rate (nondimensional) versus scale (nondimensional) for Charney's model of ITCZ with the QEA parameterization.

tions:

$$U_j = \frac{\partial \bar{S}_j}{\partial y} = \frac{\partial \bar{h}_j}{\partial y} = 0 \quad \text{for } j = 1, 3, 5 \tag{4.6.1}$$

and

$$\nabla^2 = -k^2$$

Following the notions of Appendix A, the cloud mass flux for a three-layer case, with the assumptions given by (4.6.1), is given as: (Henceforth, we will drop the primes ($'$) from the perturbation quantities)

$$\begin{aligned}
M_2 &= B_{22} W_2 + B_{24} W_4 \\
M_4 &= B_{42} W_2 + B_{44} W_4 \\
m_B(s) &= A_{s2} W_2 + A_{s4} W_4 \\
m_B(d) &= A_{D2} W_2 + A_{D4} W_4 \\
D_3 &= \eta_{s,3}\, m_B(s) \\
D_5 &= \eta_{d,5}\, m_B(d)
\end{aligned} \tag{4.6.2}$$

These substitutions in (4.2.12) yield the equations for W_2 and W_4. Putting (4.4.9) in the whole set of equations, we get the following equations for W_2, W_4, Ψ_1, Ψ_3, Ψ_5 :

$$\begin{aligned}
\left(A - \frac{C''}{k^2}\right) W_2 + \left(B - \frac{D}{k^2}\right) W_4 &= \frac{i\beta}{k}\left(\Psi_3 - \Psi_5\right) \\
\left(A^* - \frac{C^*}{k^2}\right) W_2 + \left(B^* - \frac{D^*}{k^2}\right) W_4 &= \frac{i\beta}{k}\left(\Psi_1 - \Psi_3\right) + \frac{f_0 \varepsilon_p \Psi_1}{\rho_1 \Delta z_1}
\end{aligned} \tag{4.6.3}$$

(These constants are defined in (4.2.25).)

$$\left.\begin{aligned} i k^3 (c)\,\Psi_1 &= \frac{f_0}{\rho_1 \Delta z_1}\left(W_2 + k^2 \epsilon_p \Psi_1 \right) - i\beta k \Psi_1 \\ i k^3 (c)\,\Psi_3 &= \frac{f_0}{\rho_3 \Delta z_3}\left(W_4 - W_2 \right) - i\beta k \Psi_3 \\ i k^3 (c)\,\Psi_5 &= \frac{f_0}{\rho_5 \Delta z_5}\left(- W_4 \right) - i\beta k \Psi_5 \end{aligned}\right\} \quad (4.6.4)$$

where (c) is the complex phase speed ($C = C_r + i C_i$).
We have substituted (4.6.3) into (4.6.4) and solved for the eigenvalue

The vertical structure of the mean tropical atmosphere over the Caribbean and the vertical staggering of Z levels used for these calculations is shown in Figure 4.6.

The cloud base is taken at 600 metres, the shallow clouds detrain at 4.05 km and the deep clouds detrain at 10.95 km. Clouds are assumed to have their roots in the mixed layer and therefore, the value of h at the cloud base is specified from the mean environmental values at Z_1 (= 300 metres).

4.6.1 <u>One-cloud and two-cloud model</u>

We have solved (4.6.4) for the complex phase speed (c) for two cases. For one case, we have taken the deep cloud only and in the other, we have taken the deep and the shallow clouds. We would refer to these two cases as one-cloud and two-cloud models, respectively.

For the case of the deep clouds only, we make the following substitutions in (4.6.2) and (4.2.12):

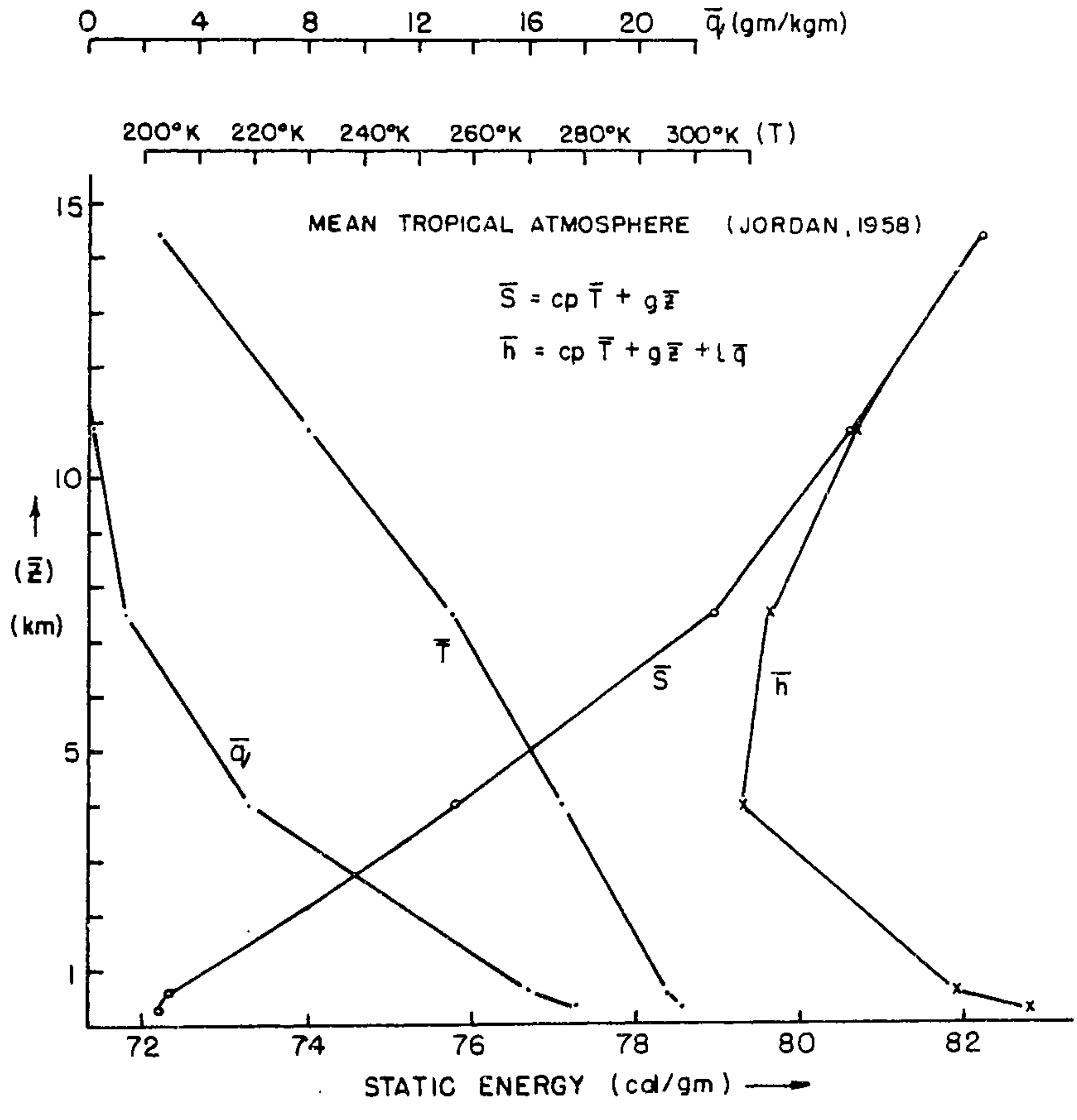

Figure 4.6 Vertical structure of temperature $\overline{T}$, mixing ratio $\overline{q}$, dry static energy $\overline{S}$, and moist static energy $\overline{h}$ for mean tropical atmosphere over the Caribbean.

$$\left.\begin{aligned} &m_B(s) = 0 \\ &A_{s2} = A_{s4} = D_3 = \ell_{s,3} = \eta_{s,3} = 0 \\ &M_2 = m_B(d) \\ &M_4 = \eta_{d,4}\, m_B(d) \\ &m_B(d) = A_{D2} W_2 + A_{D4} W_4 \end{aligned}\right\} \quad (4.6.1.1)$$

(values of A_{D2}, A_{D4} (see Appendix A) are now changed because $\ell_{s,3} = D_3 = 0$)

The boundary condition for the vertical velocity and cloud mass flux is given as: (Referring to the notations of Fig. 4.1)

$$\begin{aligned} &W_0 = W_E \text{ (Ekman pumping)} \\ &M_0 = 0 \\ &W_6 = 0 \\ &\ell_{,6} = 0 \end{aligned} \quad (4.6.1.2)$$

$M_0 = M_6 = 0$, is a statement of the obvious fact that there is no cloud mass flux below the cloud base or above the top of the cloud.

Figure 4.7. gives the phase speed and the growth rate for a range of the values of wavelength. It may be seen that the shape of the growth rate curve remains essentially the same for the two-cloud model and the deep cloud only. Figure 4.8 gives the vertical structure of the amplitude and phase of Ψ for the fastest growing mode. For the one-cloud model, the amplitude is a maximum at the lowest layer and decreases upwards. For the two-cloud model, the amplitude is a maximum at the level Z_3 and then

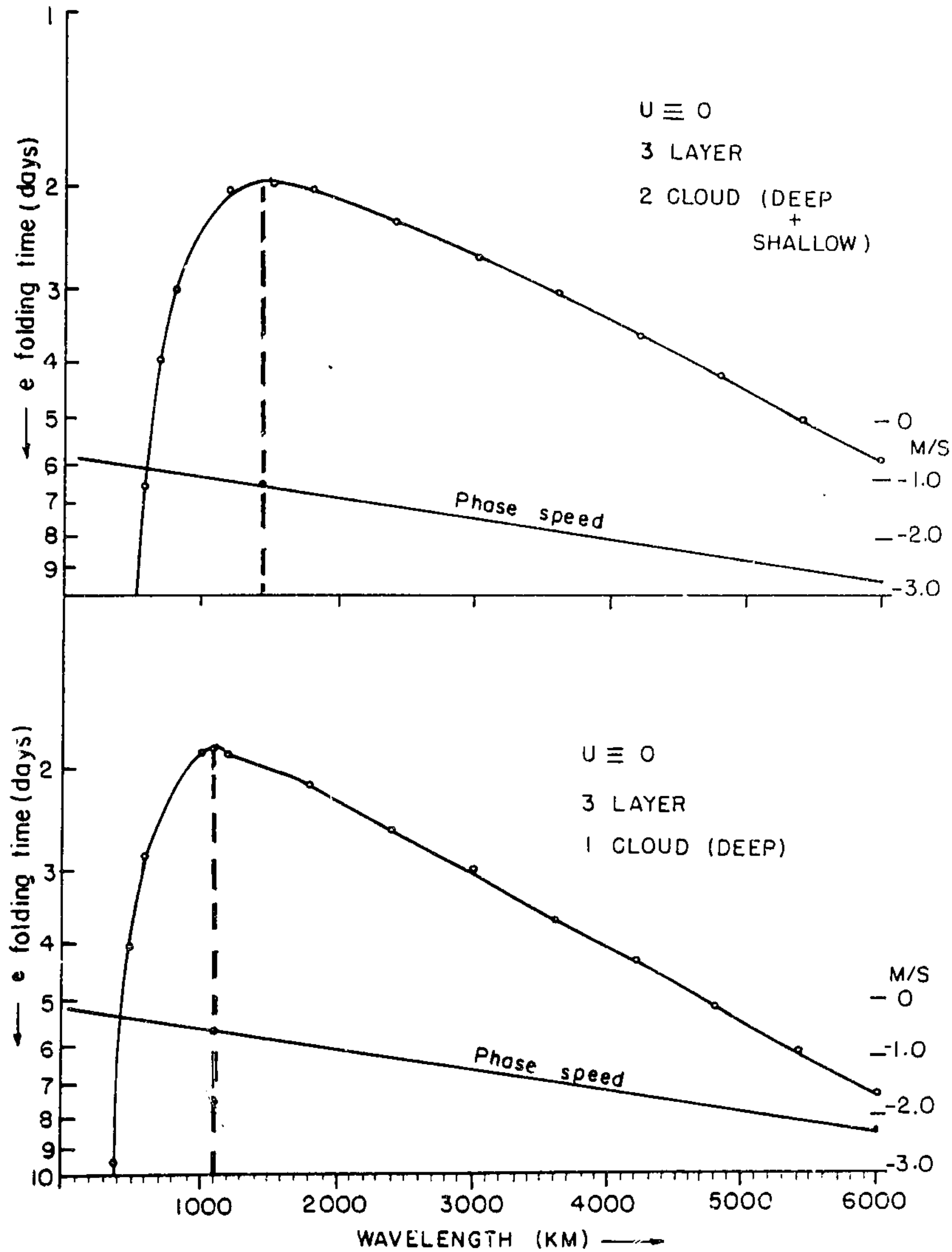

Figure 4.7 e- folding time and phase speed versus wavelength for one-cloud and two-cloud model of the three-layer resting atmosphere.

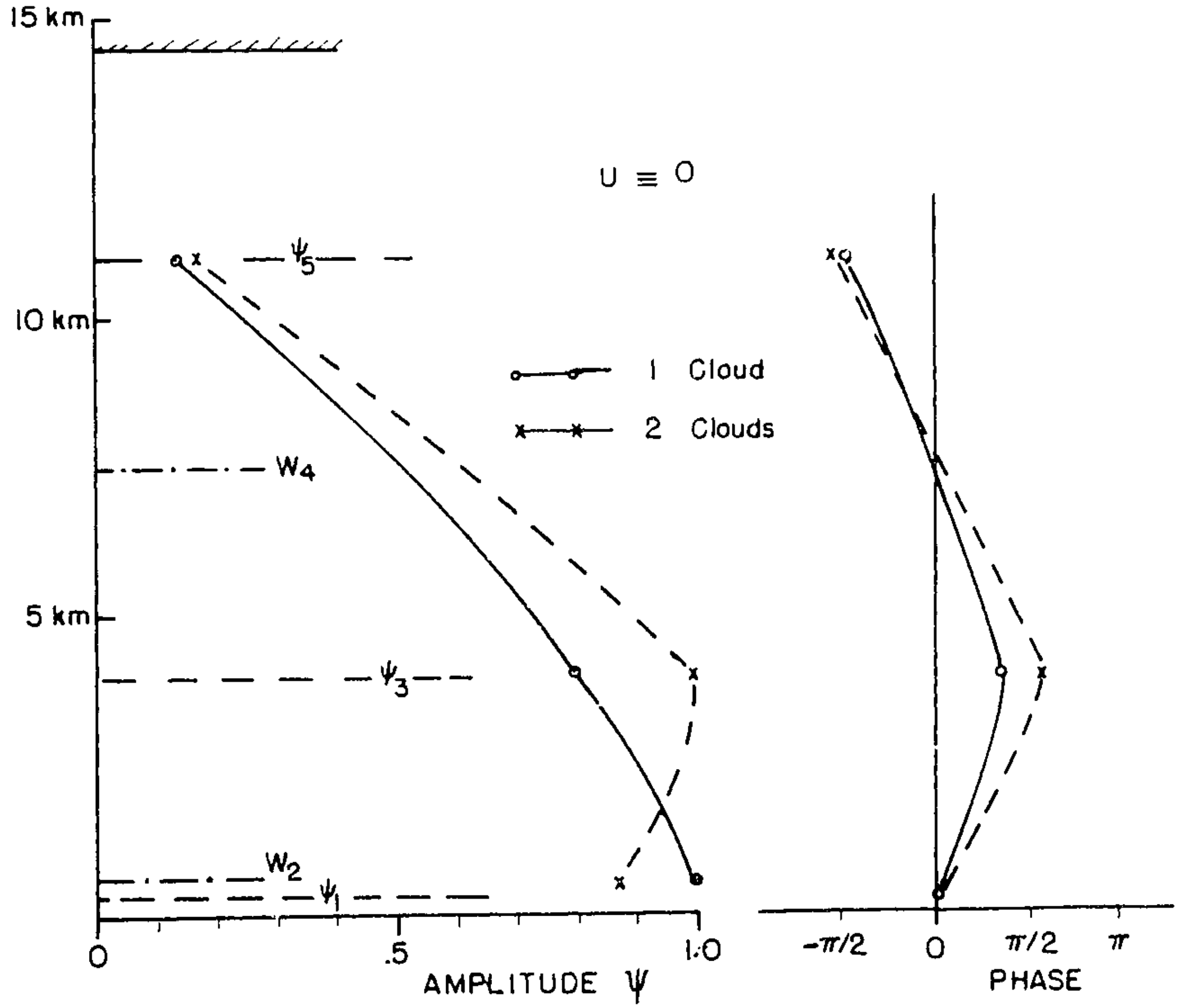

Figure 4.8 Amplitude and phase structure of (ψ) for the most unstable mode of one-cloud and two-cloud model.

decreases upwards. This difference occurs because the shallow clouds contribute to the total cloud mass flux and to the determination of liquid water in the lower layers. This effect is absent in the absence of shallow clouds.

Thus, it is seen that the essential character of the growth rate curve is determined by the deep clouds which are precipitating and providing the heating to the substantial part of the atmosphere. The role of the shallow clouds is to moisturize the lower part of the atmosphere. In an instability analysis, therefore, while considering the growth of the perturbations over a specified mean state, it may be reasonable to ignore the effects of shallow clouds and consider the effects of deep clouds only.

The results in Figure 4.7 are in good agreement with the results of Arakawa and Chao (1975) for a balanced cyclone model (see section 4.6.3 of this thesis). In order to make such comparisons, the vertical structure of $\bar{s}$ and $\bar{h}$ and the vertical staggering of Z levels was kept the same as in Arakawa and Chao (1975).

As shown in Figure 4.7, for the case of deep clouds only, the wavelength of the perturbations having maximum growth rate is 1100 km, the phase speed is -.6 m/s and e- folding time is 1.83 days. The novel feature of this result is the occurrence of maximum growth rate for an intermediate scale of reasonable size ($L \approx 1000$ km). In this model, for growth to occur, the vertically integrated cumulus heating must be greater than the vertically integrated adiabatic cooling. Among all the growing modes, the fastest growing mode is the one for which the vertically integrated net heating is a maximum.

Since the cloud mass fluxes M_2 and M_4 are proportional to a linear combination of W_2 and W_4, the magnitude of the net heating depends upon the vertical structure of the W field (i.e., relative magnitudes of W_2 and W_4) and the constants of proportionality between the mass flux and the vertical velocities. The constants B_{22}, B_{24}, B_{42}, B_{44} (see (4.6.2)) are determined by the quasi-equilibrium assumption. These constants depend upon the mean vertical structure (temperature and moisture) of the atmosphere and therefore, remain the same for all the modes.

Since the equations for W_2 and W_4 (see (4.6.3)) are linear, the interior vertical velocity may be decomposed into a component due to friction in the boundary layer and a component due to heating in the interior. Using the suffix F and H for the components due to friction and heating, respectively,

$$\left.\begin{aligned} W_2 &= W_2^F + W_2^H \\ W_4 &= W_4^F + W_4^H \end{aligned}\right\} \qquad (4.6.1.3)$$

For the purpose of mathematical convenience and without any loss of generality for these results, it is further assumed that $\beta = 0$.

Substituting (4.6.13) in (4.6.3):

$$\begin{aligned} L_1 W_2^F + L_2 W_4^F &= 0 \\ L_3 W_2^F + L_4 W_4^F &= \cdot \frac{f_0 \varepsilon_p \psi_1 k^2}{\rho_1 \Delta z_1} \end{aligned} \qquad (4.6.1.4)$$

and

$$\left.\begin{aligned} A_1 W_2^H + A_2 W_4^H &= (A_1 - L_1) W_2^F + (A_2 - L_2) W_4^F \\ A_3 W_2^H + A_4 W_4^H &= (A_3 - L_3) W_2^F + (A_4 - L_4) W_4^F \end{aligned}\right\} \quad (4.6.1.5)$$

where

$$A_1 = f_0 R_3 + k^2 \{ \alpha' B_{42} + \alpha_3 S_{32} (B_{22} - 1) \}$$

$$A_2 = - f_0 (R_3 + R_5) + k^2 \{ \alpha' (B_{44} - 1) + \alpha_3 S_{32} B_{24} \}$$

$$A_3 = - f_0 (R_1 + R_3) + k^2 \{ \alpha^* (B_{22} - 1) + \alpha_3 S_{43} B_{42} \}$$

$$A_4 = f_0 R_3 + k^2 \{ \alpha^2 B_{24} + \alpha_3 S_{43} (B_{22} - 1) \}$$

$$L_1 = f_0 R_3 - k^2 \alpha_3 S_{32}$$

$$L_2 = - f_0 (R_3 + R_5) - \alpha' k^2$$

$$L_3 = - f_0 (R_1 + R_3) - \alpha^* k^2$$

$$L_4 = f_0 R_3 - \alpha_3 S_{43} k^2$$

(These constants are defined in section 4.2.1)

W_2^F and W_4^F may be calculated from (4.6.1.4) and W_2^H and W_4^H may be calculated from (4.6.1.5). Vertically integrated net heating will be given as:

$$\text{Net Heating} = \dot{Q} \propto \Big[\big\{ (B_{22} - 1) (W_2^F + W_2^H) + B_{24} (W_4^F + W_4^H) \big\} (\bar{S}_3 - \bar{S}_1) + \big\{ B_{42} (W_2^F + W_2^H) + (B_{44} - 1) (W_4^F + W_4^H) \big\} (\bar{S}_5 - \bar{S}_3) \Big] \quad (4.6.1.6)$$

It may be seen from (4.6.1.6) that the net heating depends upon the constants B_{22}, B_{24}, B_{42}, B_{44}, W_2^F, W_4^F, W_2^H and W_4^H. W_2^H and W_4^H depend, interalia, upon W_2^F, W_4^F and the constants B_{22}, B_{24}, B_{42}, B_{44}.

Figure 4.9 shows the magnitude of net heating $\dot{Q}$, for a range of wavelengths. The values of the constants for this model are;

$B_{22} = .562714$, $B_{24} = .220388$, $B_{42} = 1.08013$, $B_{44} = .423034$. The wavelength of the perturbation having maximum growth rate is nearly the same as the wavelength of the perturbation for which the net heating is a maximum.

4.6.2 The role of friction

We have seen in section 4.5 that for the case of a two-layer model of the resting atmosphere there are no growing solutions in the absence of surface friction. (4.6.1.4) and (4.6.1.5) show that, in the absence of surface friction, there are no growing solutions for a three-layer resting atmosphere also. For $\varepsilon_p = 0$ in (4.6.1.4), $W_2^F = W_4^F = 0$, i.e., there is no internal vertical velocity generated due to surface friction.

For $W_2^F = W_4^F = 0$,

the right-hand side of (4.6.1.6) is $= 0$. Then, W_2^H and W_4^H

exist only if

$A_1A_4 - A_2A_3 = 0$

For the values of the constants given above and for the range of wavelengths of interest,

$$A_1 A_4 - A_2 A_3 \neq 0$$

and therefore, $W_2^H = W_4^H = 0$

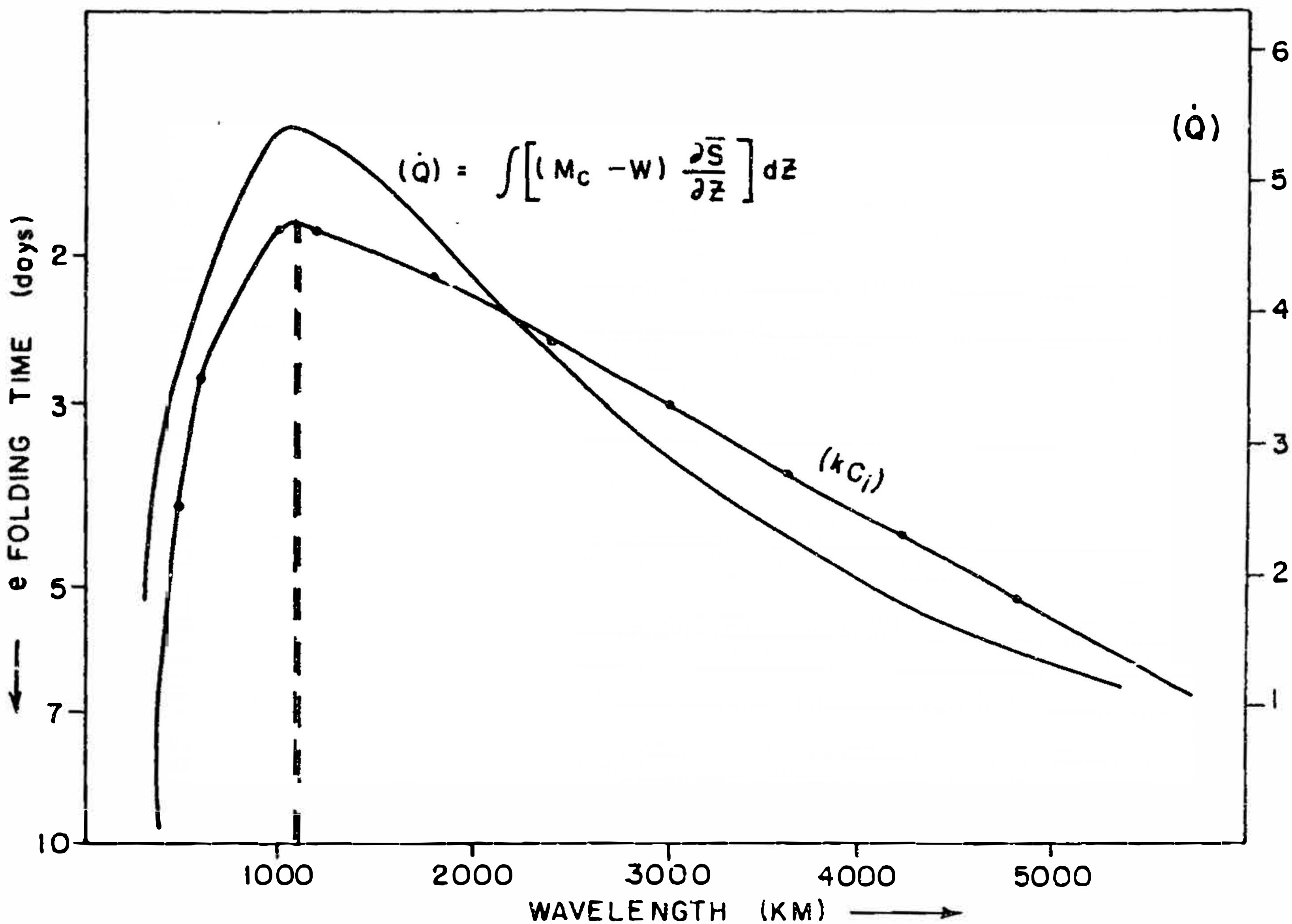

Figure 4.9 e- folding time and vertically integrated net heating (arbitrary units) versus wavelength for the three-layer resting atmosphere.

This shows that in the absence of surface friction there is no mechanism to generate the internal vertical velocity and therefore, there is no possibility of cumulus heating. If $\beta \neq 0$, W_2^H and W_4^H may have non-zero values, but their magnitudes are very small and therefore, the associated cumulus heating is very small, and therefore, the computed growth rates are found to be extremely small (growth rate $\approx 10^{-21} sec^{-1}$). In the presence of surface friction, the frictional convergence associated with the infinitesimal perturbation, is sufficient to generate an internal vertical velocity which, in turn, produces heating. Thus, there is a possibility that the perturbations may grow.

The situation is different, however, in the case of vertically shearing flows. In this case, differential vorticity advection and thickness advection may generate the internal vertical velocity. Thus, there is a possibility that cumulus heating may take place. Whether the net heating is accomplished or not would, however, depend upon the structure of the vertical velocity field. The vertical velocity field, obtained by solving the quasi-geostrophic omega equation, would now be the one which is consistent with the hydrostatic and geostrophic assumptions and the parameterized form of cumulus heating.

4.6.3 Wave-CISK versus QEA

As it was pointed out in Chapter 2, in some empirical parameterizations, the cumulus heating is parameterized in terms of the vertical velocity at the top of the lowest layer and the vertical distribution function is arbitrary. We have referred to such parameterization as wave-CISK type.

For the three-layer model, the wave-CISK parameterization corresponds to:

$$\left.\begin{aligned} M_2 &= \eta_1 W_2 \\ M_4 &= \eta_2 W_2 \end{aligned}\right\} \qquad (4.6.3.1)$$

where η_1 and η_2 are arbitrary.

For the case of the three-layer model in a resting atmosphere, we may derive the equivalent η profile for the parameterization with QEA and we may show the essential differences between the parameterization of (4.6.3.1) and equivalent η profile of QEA.

Since $$M_2 = B_{22} W_2 + B_{24} W_4$$

and $$M_4 = B_{42} W_2 + B_{44} W_4$$

the expressions for M_2 and M_4 may be rewritten as:

$$\left.\begin{aligned} M_2 &= \eta_1^* W_2 \\ \text{and} \quad M_4 &= \eta_2^* W_2 \end{aligned}\right\} \qquad (4.6.3.2)$$

because W_2 and W_4 are interrelated.

In order to demonstrate this point with the simplest possible model, we have considered the three-layer 'balanced cyclone model' studied by Arakawa and Chao (1975).

Following the notations of this chapter, the dynamical equations of this model may be written as:

$$\frac{\partial}{\partial t}\frac{\partial^2 \psi_5'}{\partial x^2} = -f_0 \frac{W_4}{\Delta z_5} \tag{4.6.3.3}$$

$$\frac{\partial}{\partial t}\frac{\partial^2 \psi_3'}{\partial x^2} = f_0 \frac{W_4 - W_2}{\Delta z_3} \tag{4.6.3.4}$$

$$\frac{\partial}{\partial t}\frac{\partial^2 \psi_1'}{\partial x^2} = \frac{f_0}{R}\frac{W_2}{\Delta z_1} \tag{4.6.3.5}$$

where R is the coefficient of Rayleigh friction in the lowest layer where the frictional and coriolis forces are assumed to be in balance. Equations for S' and the hydrostatic equations are the same as given in section 4.2.1.

Making use of the hydrostatic relationship:

$$\psi_5' - \psi_3' = \alpha_3 S_3' + \alpha_5 S_5'$$

we may find a relationship between W_2 and W_4. By using (4.6.3.3) and (4.6.3.4) and putting

$$\frac{\partial^2}{\partial x^2} = -k^2$$

it is found that:

$$W_4 = \frac{C_2}{C_4} W_2 \tag{4.6.3.6}$$

where C_2 and C_4 are the constants determined by the vertical structure of the atmosphere, k and f_0 .

Substituting for W_4 in the expressions for M_2 and M_4, we find:

$$M_2 = \eta_1^* W_2$$

$$M_4 = \eta_2^* W_4$$

where

$$\eta_1^* = \begin{bmatrix} B_{22} f_0^2 (R_3 + R_5) - k^2 \{ B_{22} (B_{44} - 1)(a^* + b^*) \\ + B_{22} B_{24} c^* - B_{22} e^* A_{s4} \} + B_{24} f_0^2 R_3 \\ + k^2 \{ B_{24} B_{42} (a^* + b^*) + B_{24} (B_{22} - 1) c^* - B_{24} e A_{s2} \} \end{bmatrix}$$

$$\eta_2^* = \begin{bmatrix} B_{42} f_0^2 (R_3 + R_5) - k^2 \{ B_{42} (B_{44} - 1)(a^* + b^*) \\ + B_{42} B_{24} c^* - B_{42} e^* A_{s4} + B_{44} f_0^2 R_3 \\ + k^2 \{ B_{44} B_{42} (a^* + b^*) + B_{44} (B_{22} - 1) c^* - B_{44} e^* A_{s4} \end{bmatrix} \qquad (4.6.3.7)$$

where $R_j = \dfrac{f_0}{\rho_j \Delta z_j} \quad (j = 1, 3, 5) \quad ; \quad a^* = \dfrac{g}{2 c_p \bar{T}_5 \rho_5} (\bar{S}_5 - \bar{S}_4)$

$$b^* = \frac{g}{2 c_p \bar{\bar{T}}_3 \rho_3} (\bar{S}_4 - \bar{S}_3) \quad ; \quad c^* = b^* \frac{(\bar{S}_3 - \bar{S}_2)}{(\bar{S}_4 - \bar{S}_3)}$$

$$e^* = \eta_{s,3} \, l_{s,3} \, L \, \frac{g}{2 c_p \bar{\bar{T}}_3 \rho}$$

(Other notations have the same meaning as defined before)

Comparison of (4.6.3.1) and (4.6.3.7) clearly brings out the novel feature of the QEA that the coefficients η_1^*, η_2^* are not arbitrary constants, but are determined by the vertical structure of the atmosphere and the wavelength of the perturbation. One of the most discomforting aspects of the empirical specification of η is that the values of η remain the same for all the horizontal scales. In the QEA parameterization, the values of η_1^* and η_2^* are determined by the wavelength of the perturbations.

Incidentally, it may be remarked that we have performed the numerical integration of this 'balanced cyclone model' to test the correctness of our numerical procedure to make the instability analysis, by initial value approach. The initial value approach and the eigenvalue approach gave the same results.

4.6.4 Maximum Growth Rate and Maximum Potential for Dominance

In interpreting the results of instability analysis, it is generally assumed that the wave having maximum growth rate would eventually dominate over the rest of the growing waves. The synoptic waves appearing on the weather charts are recognized as the possible manifestations of the fastest growing mode of the instability analysis.

In the case of barotropic or baroclinic instability, it may be reasonable to assume that the perturbations having the maximum growth rate will eventually dominate because they would 'consume' most of the available kinetic or available potential energy. It is not clear if this would be so in the case of instabilities driven by moist convection because in this case, the extent to which a perturbation of a given wavelength may grow would be determined by the availability of moisture on the scale of that perturbation. Although the growth rate of the small-scale waves may be large, if the period of such waves is small, the total moisture evaporated over one period of the wave may not be sufficient to sustain the precipitation and therefore the maximum growth of the wave may not take place.

The actual equilibration mechanism for the tropical waves, which are driven primarily by cumulus heating, is not quite clear. Because of the nonlinearity connected with real condensational heating, an arbitrary flow may not be expressed as a superposition of linear eigenmodes, and therefore it may not be possible to apply a selection principle based on these considerations; i.e., the mode with the greatest growth rate does not necessarily dominate. We do not fully understand the roles of the mean motion and the availability of moisture in determining either the maximum possible amplitude of the tropical waves or the selection mechanism due to which the synoptic waves appear on the weather charts. Hayashi (1971) has hypothesized that the heating decreases with the increasing frequency of the waves so that the high frequency waves are stabilized. Lindzen (1974) has suggested that the equilibration of tropical waves may be determined by the way the waves modify the environment. The cumulus heating may modify the basic state in such a way that the most unstable modes may become neutral with respect to the modified environment. Although the gravity waves of the smallest scales had maximum growth rate in Lindzen's analysis, he hypothesized that the instability would not prove effective for those waves whose time scales are shorter than the life cycle of a hot tower.

In order to explain the appearance of synoptic-scale waves on the daily weather charts (even if the instability analysis may give the maximum growth rate for the smallest scale), we hypothesize that only those waves would 'dominate' (and hence appear on the synoptic chart) for which the ratio of their period to their e- folding time is maximum. Since the upper limit on the amplitude of a wave may be determined by its ability to utilize the available moisture, a wave may not dominate just because it has large growth rate. A large growth rate would only imply that it would equilibrate faster than other waves. The waves having larger periods may have the potential to dominate among all the growing waves.

We have, therefore, defined a quantity $\flat$, denoting the 'potential for dominance' and is given as the ratio of the imaginary and the real parts of the complex phase speed. ($\flat = C_i / C_r$).

We will calculate the values of $\flat$ for a range of wavelengths and, according to our hypothesis, the perturbation of that wavelength would have maximum potential for dominance for which $\flat$ is maximum.

We have calculated the values of $\flat$ for the model described in section 4.6.1. The result is shown in Figure 4.10. The values of growth rate for a range of wavelengths is also shown in the same figure. It is found that the maximum growth rate and the maximum potential for dominance occur for nearly the same wavelength. We have presented similar results for vertically shearing flows in the next section.

We would like to emphasize that the above criteria, based on the ratio (C_i / C_r), to determine the most dominant perturbation is only a hypothesis. This criteria breaks down for $C_r = 0$. It is possible that for certain structures of the mean state, none of the criteria mentioned above suggest a dominant mode. In such a situation, we propose to examine

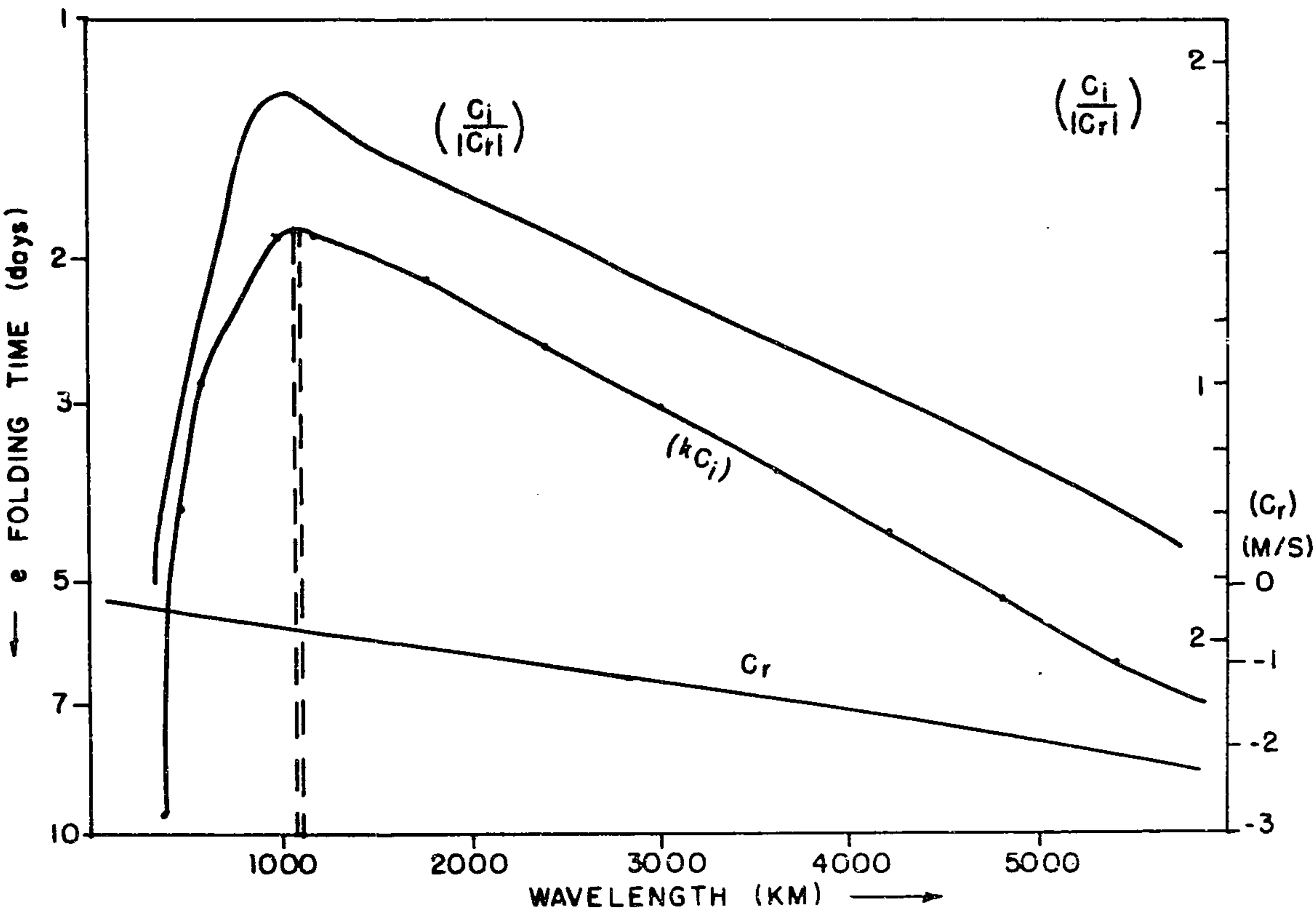

Figure 4.10 Growth rate (kCi), phase speed (Cr) and the ratio (Ci/Cr) versus wavelength for the three-layer resting atmosphere.

the structure of those perturbations whose wavelength corresponds to that of the observed synoptic disturbances. A more rigorous criteria to explain the scale of the observed tropical waves awaits a clearer understanding of the equilibration mechanism for the tropical waves and their interaction with the mean motion.

4.7 The Three-layer Model with Vertical Shear

The governing equations for the three-layer model with vertical shear are the same as given by (4.2.14) through (4.2.25) with the added simplifications that

$$\nabla^2 = -k^2 \quad , \quad \frac{\partial \bar{U}}{\partial y} = 0$$

The procedure for performing the instability analysis in this case consists of the following steps:

i) Derive the expressions for $m_8(s)$ and $m_8(d)$ using the QEA in terms of ψ_j' , s_j' and h_j' for j = 1,3,5 (see Equations A.8 and A.9).

ii) Derive the expressions for M_2 and M_4 from A.10 and A.11.

iii) Substitute the expressions for $M_2, M_4, D_3, D_5, \ell_{5,3}$ in (4.2.12) and derive the expressions for W_2 and W_4 in terms of ψ_j', s_j', h_j' (j = 1,3,5). (See Equations 4.2.24 and 4.2.25).

iv) Substitute the expressions for W_2 and W_4 in (4.2.14) through (4.2.22). This would give us nine equations for nine variables:

$$\psi_1', \psi_3', \psi_5', s_1', s_3', s_5', h_1', h_3', h_5'.$$

Let us assume that all the perturbation quantities are of the form:

$$\begin{Bmatrix} \psi' \\ s' \\ h' \end{Bmatrix} = Re \begin{Bmatrix} \psi \\ s \\ h \end{Bmatrix} e^{ik(x-ct)} \qquad (4.7.1)$$

where c is the complex phase speed (= $c_r + i c_i$).

Substitution of (4.7.1) in (4.2.14) through (4.2.22) and application of the boundary conditions given in (4.6.1.2) yields the following eigenvalue problem:

$$\begin{bmatrix} (A_{11}-c) & A_{21} & A_{31} & A_{41} & A_{51} & A_{61} & A_{71} & A_{81} & A_{91} \\ A_{12} & (A_{22}-c) & A_{32} & A_{42} & A_{52} & A_{62} & A_{72} & A_{82} & A_{92} \\ A_{13} & A_{23} & (A_{33}-c) & A_{43} & A_{53} & A_{63} & A_{73} & A_{83} & A_{93} \\ A_{14} & A_{24} & A_{34} & (A_{44}-c) & A_{54} & A_{64} & A_{74} & A_{84} & A_{94} \\ A_{15} & A_{25} & A_{35} & A_{45} & (A_{55}-c) & A_{65} & A_{75} & A_{85} & A_{95} \\ A_{16} & A_{26} & A_{36} & A_{46} & A_{56} & (A_{66}-c) & A_{76} & A_{86} & A_{96} \\ A_{17} & A_{27} & A_{37} & A_{47} & A_{57} & A_{67} & (A_{77}-c) & A_{87} & A_{97} \\ A_{18} & A_{28} & A_{38} & A_{48} & A_{58} & A_{68} & A_{78} & (A_{88}-c) & A_{98} \\ A_{19} & A_{29} & A_{39} & A_{49} & A_{59} & A_{69} & A_{79} & A_{89} & (A_{99}-c) \end{bmatrix} \begin{bmatrix} \psi_1 \\ \psi_3 \\ \psi_5 \\ S_1 \\ S_3 \\ S_5 \\ h_1 \\ h_3 \\ h_5 \end{bmatrix} = 0 \quad (4.7.2)$$

where the matrix A_{ij} ($i = 1,9$ and $j = 1,9$) is complex. It may be recalled that in the case of resting atmosphere we have solved only a 3 x 3 matrix because the cloud mass flux is determined in terms of W_2 and W_4 only.

In the case of shearing zonal flow, the cloud mass flux also depends upon the advections of s' and h' by the mean motion and the advections of $\bar{s}$ and $\bar{h}$ by the perturbation stream function ψ' . We therefore must consider the time variations of ψ' , s' and h' in a coupled way.

The expressions for all the elements of the complex matrix are given below: (We would use the notation $m = \sqrt{-1}$)

$$A_{11} = \left(U_1 - \frac{\beta}{k^2} + F_1 A_1 \right) + m \left(F_1 A_1' - \frac{\epsilon_p}{k} \right),$$

$$\text{where} \quad F_j = \frac{f_0}{k^2 \rho_j \Delta z_j}, \quad j = 1, 3, 5.$$

and

$$A_{i1} = F_1 A_i \quad \text{for} \quad i = 2, 9$$

(Imaginary parts of all the elements A_{ij} for i = 2,9, and j = 1,9 would be equal to zero. This is because the imaginary parts of the matrix A_{ij} appear due to the terms involving the Ekman pumping and the Ekman pumping is proportional to Ψ_1 only.)

$$A_{12} = F_3 (B_1 - A_1) + m \left\{ F_3 (B_1' - A_1') \right\}$$

$$A_{22} = U_3 - \frac{\beta}{k^2} + F_3 (B_2 - A_2)$$

$$A_{i2} = F_3 (B_i - A_i) \qquad \text{for } i = 3,9$$

$$A_{13} = F_5 (B_1 - m B_1')$$

$$A_{23} = F_5 B_2$$

$$A_{33} = U_5 - \frac{\beta}{k^2} + F_5 B_3$$

$$A_{i3} = F_5 B_i \qquad \text{for } i = 4,9$$

$$A_{14} = \left[\frac{\partial \bar{s}_1}{\partial y} - \frac{\bar{s}_2 - \bar{s}_1}{\rho_1 \Delta z_1}\left\{(B_{22}-1)\ A_1' + B_{24}B_1 + a_1 + b_1\right\}\right]$$
$$+ m\left[\frac{\bar{s}_1 - \bar{s}_2}{\rho_1 \Delta z_1}\left\{(B_{22}-1)\ A_1' + B_{24}B_1'\right\}\right]$$

$$A_{i4} = \left(\frac{\bar{s}_1 - \bar{s}_2}{\rho_1 \Delta z_1}\right)\left\{(B_{22}-1)\ A_i + B_{24}B_i + a_i + b_i\right\}$$

for $i = 2, 3, 5, 6, 7, 8, 9.$

$$A_{44} = \left(\frac{\bar{s}_1 - \bar{s}_2}{\rho_1 \Delta z_1}\right)\left\{(B_{22}-1)\ A_4 + B_{24}B_4 + a_4 + b_4\right\} + U_1$$

$$A_{15} = \left\{\gamma_1 A_1 + \gamma_2 B_1 - \gamma_3 (a_1 + b_1) - \gamma_4 \eta_{d,4} b_1 + \gamma_5 a_1\right\}$$
$$+ m\left\{\gamma_1 A_1' + \gamma_2 B_1'\right\}$$

where,

$$\gamma_1 = -\left[(B_{22}-1)\ \frac{\bar{s}_3 - \bar{s}_2}{\rho_1 \Delta z_3} + B_{42}\frac{\bar{s}_4 - \bar{s}_3}{\rho_3 \Delta z_3} - \eta_{s,3}\frac{L\ell_{s,3}}{\rho_3 \Delta z_3} A_{s2}\right]$$

$$\gamma_2 = -\left[B_{24}\frac{\bar{s}_3 - \bar{s}_2}{\rho_3 \Delta z_3} + (B_{44}-1)\ \frac{\bar{s}_4 - \bar{s}_3}{\rho_3 \Delta z_3} - \eta_{s,3}\frac{L\ell_{s,3}}{\rho_3 \Delta z_3} A_{s4}\right]$$

$$\gamma_3 = (\bar{s}_3 - \bar{s}_2)\ /\ \rho_3 \Delta z_3$$

$$\gamma_4 = (\bar{s}_4 - \bar{s}_3)\ /\ \rho_3 \Delta z_3$$

$$\gamma_5 = \eta_{s,3}\ \frac{L\ell_{s,3}}{\rho_3 \Delta z_3}$$

$$A_{25} = \left\{\gamma_1 A_2 + \gamma_2 B_2 - \gamma_3 (a_2 + b_2) - \gamma_4 \eta_{d,4} b_2\right.$$
$$\left. + \gamma_5 a_2\right\} + \frac{\partial \bar{s}_3}{\partial y}$$

$$A_{55} = \left\{\gamma_1 A_5 + \gamma_2 B_5 - \gamma_3 (a_5 + b_5) - \gamma_4 \eta_{d,4} b_5\right.$$
$$\left. + \gamma_5 a_5\right\} + \bar{U}_3$$

$$A_{i6} = - \left\{ B_{42} A_i + (B_{44}-1) B_i + \eta_{d,4} b_i \right\} \left(\frac{\bar{s}_5 - \bar{s}_4}{\rho_5 \Delta z_5} \right)$$

for $i = 1, 2, 4, 5, 7, 8, 9.$

$$A_{36} = - \left\{ B_{42} A_3 + (B_{44}-1) B_3 + \eta_{d,4} b_3 \right\} \left(\frac{\bar{s}_5 - \bar{s}_4}{\rho_5 \Delta z_5} \right) + \frac{\partial \bar{s}_5}{\partial y}.$$

$$A_{66} = - \left\{ B_{42} A_6 + (B_{44}-1) B_6 + \eta_{d,4} b_6 \right\} \left(\frac{\bar{s}_5 - \bar{s}_4}{\rho_5 \Delta z_5} \right) + \bar{U}_5$$

$$A_{16} = - \left[\left\{ B_{42} A_1 + (B_{44}-1) B_1 + \eta_{d,4} b_1 \right\} + m \left\{ B_{42} A_1' + (B_{44}-1) B_1' \right\} \right] \frac{\bar{s}_5 - \bar{s}_4}{\rho_5 \Delta z_5}$$

$$A_{17} = \left[\frac{\partial \bar{h}_1}{\partial y} - \frac{\bar{h}_2 - \bar{h}_1}{\rho_1 \Delta z_1} \left\{ (B_{22}-1) A_1 + B_{24} B_1 + a_1 + b_1 \right\} \right] + m \left[- \frac{\bar{h}_2 - \bar{h}_1}{\rho_1 \Delta z_1} \left\{ (B_{22}-1) A_1' + B_{24} B_1' \right\} \right]$$

$$A_{i7} = - \frac{\bar{h}_2 - \bar{h}_1}{\rho_1 \Delta z_1} \left\{ (B_{22}-1) A_i + B_{24} B_i + a_i + b_i \right\}$$

for $i = 2, 3, 4, 5, 6, 8, 9.$

$$A_{77} = - \left(\frac{\bar{h}_2 - \bar{h}_1}{\rho_1 \Delta z_1} \right) \left\{ (B_{22}-1) A_7 + B_{24} B_7 + a_7 + b_7 \right\} + U_1$$

$$A_{18} = \left\{ X_1 A_1 + X_2 B_1 - X_3 (a_1 + b_1) - X_4 \eta_{d,4} b_1 + X_5 a_1 \right\} + m \left\{ X_1 A_1' + X_2 B_1' \right\}$$

where,

$$X_1 = - \left[(B_{22}-1) \frac{\bar{h}_3 - \bar{h}_2}{\rho_3 \Delta z_3} + B_{42} \frac{\bar{h}_4 - \bar{h}_3}{\rho_3 \Delta z_3} + \eta_{s,3} \frac{\bar{h}_3^* - \bar{h}_3}{\rho_3 \Delta z_3} A_{s2} \right]$$

$$X_2 = -\left[B_{24}\frac{\bar{h}_3-\bar{h}_2}{\rho_3\Delta z_3} + (B_{44}-1)\frac{\bar{h}_4-\bar{h}_3}{\rho_3\Delta z_3} + \eta_{s,3}\frac{\bar{h}_3^*-\bar{h}_3}{\rho_3\Delta z_3}A_{s4}\right]$$

$$X_3 = (\bar{h}_3-\bar{h}_2)/\rho_3\Delta z_3$$

$$X_4 = (\bar{h}_4-\bar{h}_3)/\rho_3\Delta z_3$$

$$X_5 = -\eta_{s,3}\frac{\bar{h}_3^*-\bar{h}_3}{\rho_3\Delta z_3}$$

$$A_{i8} = \left\{X_1A_i + X_2B_i - X_3(a_i+b_i) - X_4\eta_{d,4}b_i + X_5a_i\right\}$$

for i = 3,4,5,6,7,9

$$A_{28} = \left\{X_1A_2 + X_2B_2 - X_3(a_2+b_2) - X_4\eta_{d,4}b_2 + X_5a_2\right\} + \frac{\partial\bar{h}_3}{\partial y}$$

$$A_{88} = \left\{X_1A_8 + X_2B_8 - X_3(a_8+b_8) - X_4\eta_{d,4}b_8 + X_5a_8\right\} + \bar{U}_3$$

$$A_{19} = (x_1A_1 + x_2B_1 + x_3\eta_{d,4}b_1 + x_4b_1)$$

$$+ m(x_1A_1' + x_2B_1')$$

where
$$x_1 = -\left(B_{42}\frac{\bar{h}_5-\bar{h}_4}{\rho_5\Delta z_5} + \eta_{d,5}\frac{\bar{h}_5^*-\bar{h}_5}{\rho_5\Delta z_5}A_{D2}\right)$$

$$x_2 = -\left\{(B_{44}-1)\frac{\bar{h}_5-\bar{h}_4}{\rho_5\Delta z_5} + \eta_{d,5}\frac{\bar{h}_5^*-\bar{h}_5}{\rho_5\Delta z_5}A_{D4}\right\}$$

$$x_3 = -\frac{\bar{h}_5-\bar{h}_4}{\rho_5\Delta z_5}$$

$$x_4 = -\frac{\bar{h}_5^*-\bar{h}_5}{\rho_5\Delta z_5}\eta_{d,5}$$

$$A_{i9} = (\alpha_1 A_i + \alpha_2 B_i + \alpha_3 \eta_{d,4} b_i + \alpha_4 b_i) \quad \text{for } i = 2,4,5,6,7,8$$

$$A_{39} = (\alpha_1 A_3 + \alpha_2 B_3 + \alpha_3 \eta_{d,4} b_3 + \alpha_4 b_3) + \frac{\partial \bar{h}_s}{\partial y}$$

$$A_{99} = (\alpha_1 A_9 + \alpha_2 B_9 + \alpha_3 \eta_{d,4} b_9 + \alpha_4 b_9) + \bar{U}_s$$

where a_j, b_j (for j = 1,9), B_{22}, B_{24}, B_{42}, B_{44}, A_{s2}, A_{s4}, A_{D2}, A_{D4}, $\ell_{s,3}$, $\eta_{d,4}$, $\eta_{d,5}$ are given in Appendix A.

A_j, B_j, A_1', B_1' are given as follows:

$$A_j = (DST)\, AA_j - (BST)\, BB_j$$

$$B_j = (AST)\, BB_j - (CST)\, AA_j$$

where
$$(AST) = (WA)\,(ADBC)$$
$$(BST) = (WB)\,(ADBC)$$
$$(CST) = (WC)\,(ADBC)$$
$$(DST) = (WD)\,(ADBC)$$

where
$$WA = \frac{f_0}{\rho_3 \Delta z_3} - k^2 A$$
$$WB = \left(-\frac{f_0}{\rho_3 \Delta z_3} - \frac{f_0}{\rho_5 \Delta z_3}\right) - k^2 B$$
$$WC = \left(-\frac{f_0}{\rho_1 \Delta z_1} - \frac{f_0}{\rho_3 \Delta z_3}\right) - k^2 A^*$$
$$WD = \frac{f_0}{\rho_3 \Delta z_3} - k^2 B^*$$

(A , B , A^* , B^* are defined after 4.2.25)

and $ADBC = \{(WA)(WD) - (WB)(WC)\}^{-1}$

and AA_j , BB_j are given as follows:

$$AA_1 = k^2 \{ - t_1 \eta_{d,4} b_1 - t_2 (a_1 + b_1) + t_3 a_1 \}$$

where $t_1 = \alpha'$; $t_2 = \alpha_3 \dfrac{\bar{S}_3 - \bar{S}_2}{\rho_3 \Delta z_3}$; $t_3 = \alpha''$.

$$AA_2 = k^2 \{ \bar{U}_3 - \frac{\beta}{k^2} - t_1 \eta_{d,4} b_2 + \alpha_3 \frac{\partial \bar{S}_3}{\partial y} - t_2 (a_2 + b_2) + t_3 a_2 \}$$

$$AA_3 = k^2 \{ \bar{U}_5 - \frac{\beta}{k^2} - t_1 \eta_{d,4} b_3 + \alpha_5 \frac{\partial \bar{S}_5}{\partial y} - t_2 (a_3 + b_3) + t_3 a_3 \}$$

$$AA_4 = 0$$

$$AA_5 = k^2 \{ - t_1 \eta_{d,4} b_5 - t_2 (a_5 + b_5) + t_3 a_5 + \alpha_3 \bar{U}_3 \}$$

$$AA_6 = k^2 \{ - t_1 \eta_{d,4} b_6 - t_2 (a_6 + b_6) + t_3 a_6 + \alpha_5 \bar{U}_5 \}$$

$$AA_i = k^2 \{ - t_1 \eta_{d,4} b_i - t_2 (a_i + b_i) + t_3 a_i \} \quad \text{for } i = 7, 8, 9.$$

$$BB_1 = k^2 \{ \bar{U}_1 - \frac{\beta}{k^2} - q_1 (a_1 + b_1) - q_2 \eta_{d,4} b_1 + q_3 a_1 + \alpha_1 \frac{\partial \bar{S}_1}{\partial y} \}$$

$$BB_2 = k^2 \{ - \bar{U}_3 + \frac{\beta}{k^2} - q_1 (a_2 + b_2) - q_2 \eta_{d,4} b_2 + q_3 a_2 + \alpha_3 \frac{\partial \bar{S}_3}{\partial y} \}$$

$$BB_3 = k^2 \{ - q_1 (a_3 + b_3) - q_2 \eta_{d,4} b_3 + q_3 a_3 \}$$

$$BB_4 = k^2 \alpha_1 \bar{U}_1$$

$$BB_5 = k^2 \{ -q_1 (a_5 + b_5) - q_2 \eta_{d,4} b_5 + q_3 a_5 + \alpha_3 v_3 \}$$

$$BB_i = k^2 \{ -q_1 (a_i + b_i) - q_2 \eta_{d,4} b_i + q_3 a_i \} \quad \text{for } i = 6, 7, 8, 9.$$

where $\quad q_1 = \alpha^* \quad ; \quad q_2 = \alpha_3 \dfrac{\bar{s}_4 - \bar{s}_3}{\rho_3 \Delta z_3} \quad ; \quad q_3 = \alpha''$

(For definition of α_1, α_5, α_5, α', α'', α^* see section 4.2)

$$A_1' = -(BBT)\ BB_1'$$

$$B_1' = (AST)\ BB_1'$$

where $\quad BB_1' = -k(\epsilon_p)$

Since all the 81 elements of the complex matrix A_{ij} are nonsimple, it has not been possible to derive simple algebraic expressions for the eigenvalue C. We have, therefore, solved the equations (4.7.2) numerically. We have used the standard subroutines (available at the computation centre) for finding the eigenvalues of a complex matrix.

Figure 4.11 shows the plots of growth rate (kc_i), phase speed (c_r) and the ratio (c_i/c_r) for a range of wavelengths for the mean tropical atmosphere. The temperature and moisture structure are shown in Figure 4.6 and the structure of the zonal wind is shown in Figure 4.12. If we follow the conventional criterion that the fastest growing modes may be the most dominant perturbation, two peaks in the growth rate curve are found for wavelengths of about 1000 km and 5000 km. Wavelength of typical easterly waves is in the range of 2000-3000 km. If we follow the criterion defined in the earlier section, the wavelength of the perturbation having

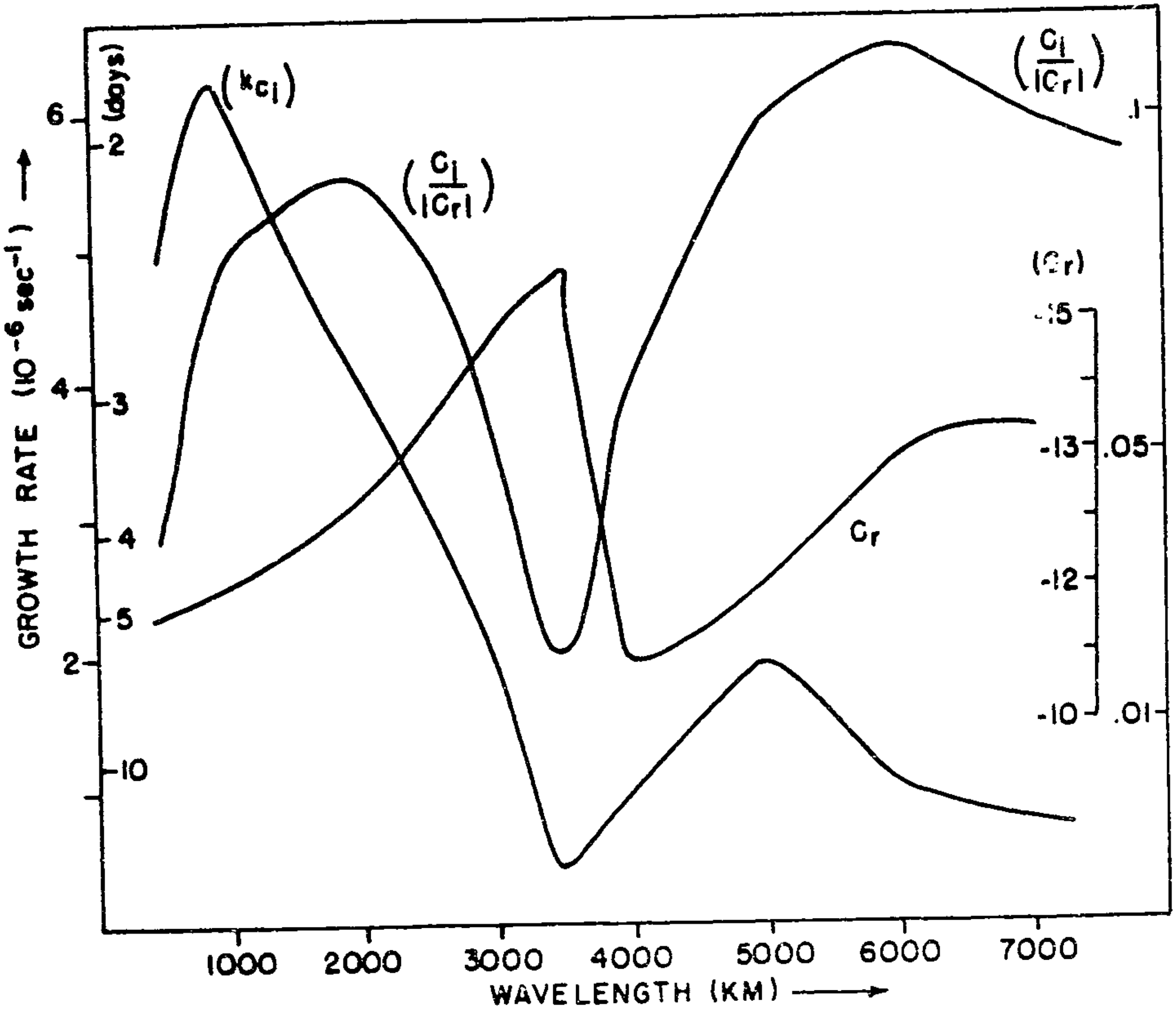

Figure 4.11 Growth rate (kCi), phase speed (Cr) and the ratio (Ci/Cr) versus wavelength for the observed zonal wind profile in the Caribbean.

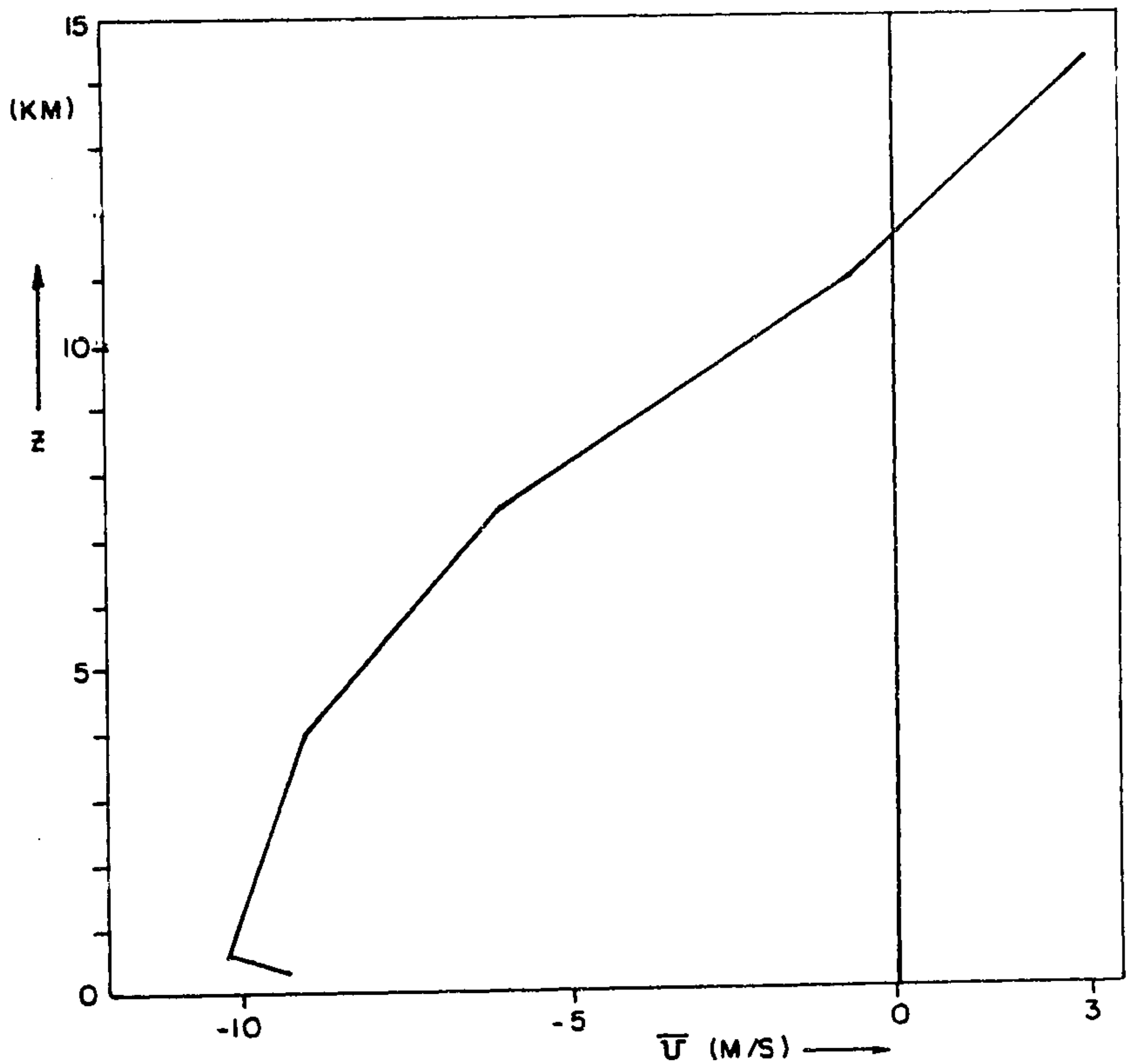

Figure 4.12 Vertical profile of the mean monthly (July) zonal wind in Caribbean at 12°35'N, 81°40'W.

maximum potential for dominance is about 6000 km. There is a secondary maxima at 2000 km which is close to the wavelength of the observed easterly waves. The amplitude of the 2000 km perturbation has a maximum at the middle level. Although the wavelength and the phase speed are in the proper range, the detailed structure of the analytical perturbation having the wavelength of 2000 km does not agree well with the structure of the observed easterly waves. The computed perturbation slopes towards the west in the vertical and the slope is very large. The rising motion occurs ahead (west) of the trough at the higher levels and behind the trough at the lower levels. In order to get a realistic structure for the easterly waves, it may be necessary to include the effects of horizontal shear.

The purpose of this calculation was to test the performance of the criterion based on the ratio (C_i/C_r) for the case of mean tropical atmosphere over the Caribbean.

Although this criterion has been presented only as a hypothesis and we have no rigorous proof for its validity, we feel that this criterion offers a reasonable basis to determine the most dominant mode.

We have made the computations of growth rate for a range of values of vertical wind shear. One of the striking features of all the calculations (see, for example, Fig. 5.2) was the occurrence of maximum growth rate for the smallest scale. This nature of the growth rate curve did not change when the effects of vorticity transport by the cumulus clouds was added. In the present linear model, mean cloud mass flux is assumed to be zero and therefore only the perturbation cloud mass flux acts to transport the vorticity of the mean field. In the absence of horizontal shear, this effect does not appear in a quasi-geostrophic model.

The occurrence of maximum growth rate for the smallest scale may be either due to inadequate treatment of the subcloud layer or due to the parameterization of cumulus heating by the quasi-equilibrium assumption. In reality, for cumulus convection to take place, the boundary layer convergence must be sufficient to lift the low level air up to the lifting condensation level. The scale of the vertical circulations, associated with small horizontal scales, is also very small. The small-scale perturbations may not provide the necessary lifting needed to set in the cumulus convection. Therefore, all the perturbations with the horizontal scale smaller than the Rossby radius of deformation, corresponding to the vertical scale of the height of the lifting condensation level, should be stable. In the present model, the treatment of the subcloud layer is very simple. The vertical resolution is not adequate to identify the top of the mixed layer and the lifting condensation level. A more realistic treatment of the mixed layer, including the time variations of the depth of the mixed layer and the height of the cloud base, is beyond the scope of this thesis. A time dependent mixed layer introduces a constraint on the intensity of convection.

It may be recalled from (4.3.34) and (4.3.35) that in the presence of vertical shear the cloud mass flux is found to be inversely proportional to the wavelength of the perturbation. Since heating is proportional to M_c' in the QEA parameterization and the vertical velocity is determined by heating and large-scale vorticity and temperature advections, the vertical velocity, and therefore the heating, is found to be maximum for the smallest scale. This was confirmed by examining the eigenfunctions for the largest eigenvalues for a range of wavelengths. This may explain the occurrence of maximum growth rate for the smallest scale. An exception may occur for those perturbations for which the vertical structures of the perturbations (ψ' , s' , h') and the mean state ($\bar{U}$, $\bar{S}$, $\bar{h}$) are such that the vertically integrated generation of the cloud work function by including the horizontal advections is equal to zero.

In the next chapter, we have performed the instability analysis of horizontally and vertically shearing monsoon flow.*

It should be noted that the instability analysis presented in this chapter was based on a vertical differencing scheme in which the stream function and the temperature were defined at the same Z levels. The same analysis was repeated for a three-layer (χ-p) model in which the temperature and vertical velocity (dp/dt) were defined at the same levels. The results were quantitatively similar for both the cases.

In order to check the correctness of the computer program and the algebra involved, which was quite considerable, calculations were made with $\bar{U} \equiv 0$ and $\bar{U} \equiv$ constant. (4.7.2) reduced to a (3x3) system in the former and (9x9) system in the latter case. The values of the growth rates remained exactly the same in both the cases, and the changes in the phase speed were exactly equal to the constant $\bar{U}$. For the case of vertical shear, the initial value approach and the eigenvalue approach gave the same results.

*If $\partial U/\partial z = 0$, for a horizontally shearing flow considered in the next chapter, the maximum growth rate occurred for a wavelength of intermediate scale (see section 5.3.1).

CHAPTER 5. INSTABILITY OF HORIZONTALLY AND VERTICALLY SHEARING MONSOON FLOW WITH PARAMETERIZATION OF MOIST-CONVECTIVE HEATING BY QUASI-EQUILIBRIUM ASSUMPTION

In this chapter, we will perform the instability analysis of the observed monsoon flow. The vertical temperature and moisture structure of the mean monsoon atmosphere has been given in Figure 1.3. This vertical structure has been obtained from Saha and Singh (1972), Koteswaram (1974) and 'Forecasting Manual' (1971) published by India Meteorological Department. We have used the three-layer quasi-geostrophic model described in section 4.2. We have used the quasi-equilibrium assumption, described in section 4.1, to parameterize the effects of cumulus heating. The cloud base is assumed to be at 450 meters, which corresponds to the lifting condensation level at 950 mb during the monsoon season. The level of detrainment for the deep clouds is at 10.05 km. It has been assumed that the deep clouds are fully precipitating. This assumption may be justified from a study of Ramanamurty et. al (1960), whose observations suggest that during the monsoon season, most of the precipitation comes from the deep clouds.

5.1 The Case of Resting Atmosphere

Figure 5.1 shows the plots of growth rate versus wavelength for a resting atmosphere. The horizontal wavelength of the fastest growing mode is found to be about 2000 km, with an e- folding time of 2.2 days. The westward phase speed of the perturbation is found to be 1.4 m/s. These results are similar to the ones presented in section 4.6. The structure of the fastest growing perturbations was found to be the same

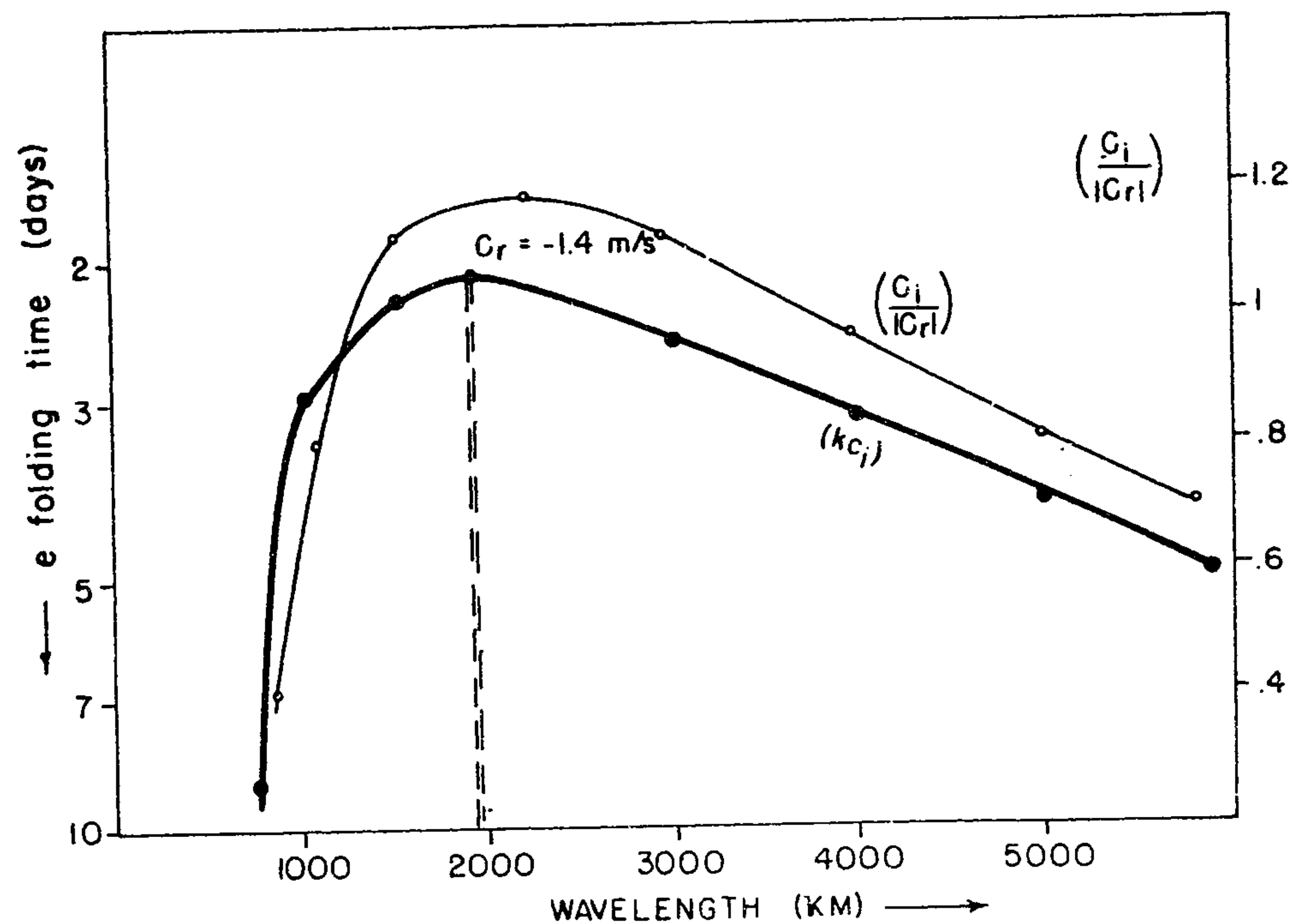

Figure 5.1 Growth rate (kCi) and ratio (Ci/Cr) versus wavelength for mean monsoon atmosphere for U = 0.

as given in Figure 4.8. Since the growth rate versus wavelength curve remained essentially the same for two-cloud types as for deep clouds only, we will use only the deep cloud model for the later analysis.

Figure 5.1 also shows the plot of (c_i/c_r) versus wavelength and growth rate versus wavelength for the case when the heating was provided by the deep clouds only. The wavelength of the perturbation having maximum growth rate is about 2000 km and the wavelength of the perturbation having maximum potential for dominance is 2200 km. The westward phase speed for the perturbation of 2200 km is 1.6 m/s and e- folding time is 2.22 days. Thus, it is seen that the criterion based on the maximum value of the growth rate and the criterion based on the maximum potential for dominance yield nearly the same values of horizontal wavelength, phase speed and e- folding time for the most dominant perturbation.

5.2 The Case of Vertical Shear

The procedure for these calculations was exactly the same as described in section 4.7. Figure 1.3 shows the vertical profile of the zonal wind, which has been used to perform the instability analysis of the monsoon zonal flow. This profile is obtained by averaging the observed zonal winds between the latitudes 20N and 30N at each vertical level. Figure 5.2 shows the plots of growth rate (kc_i), phase speed (c_r) and the ratio (c_i/c_r) for a range of wavelengths. The growth rate is found to be maximum for the smallest scale. From the criteria based on the ratio (c_i/c_r), the wavelength of the most dominant mode is found to be about 2500 km. The westward phase speed for this mode is about 4 m/s. These values of the wavelength and the phase speed are in

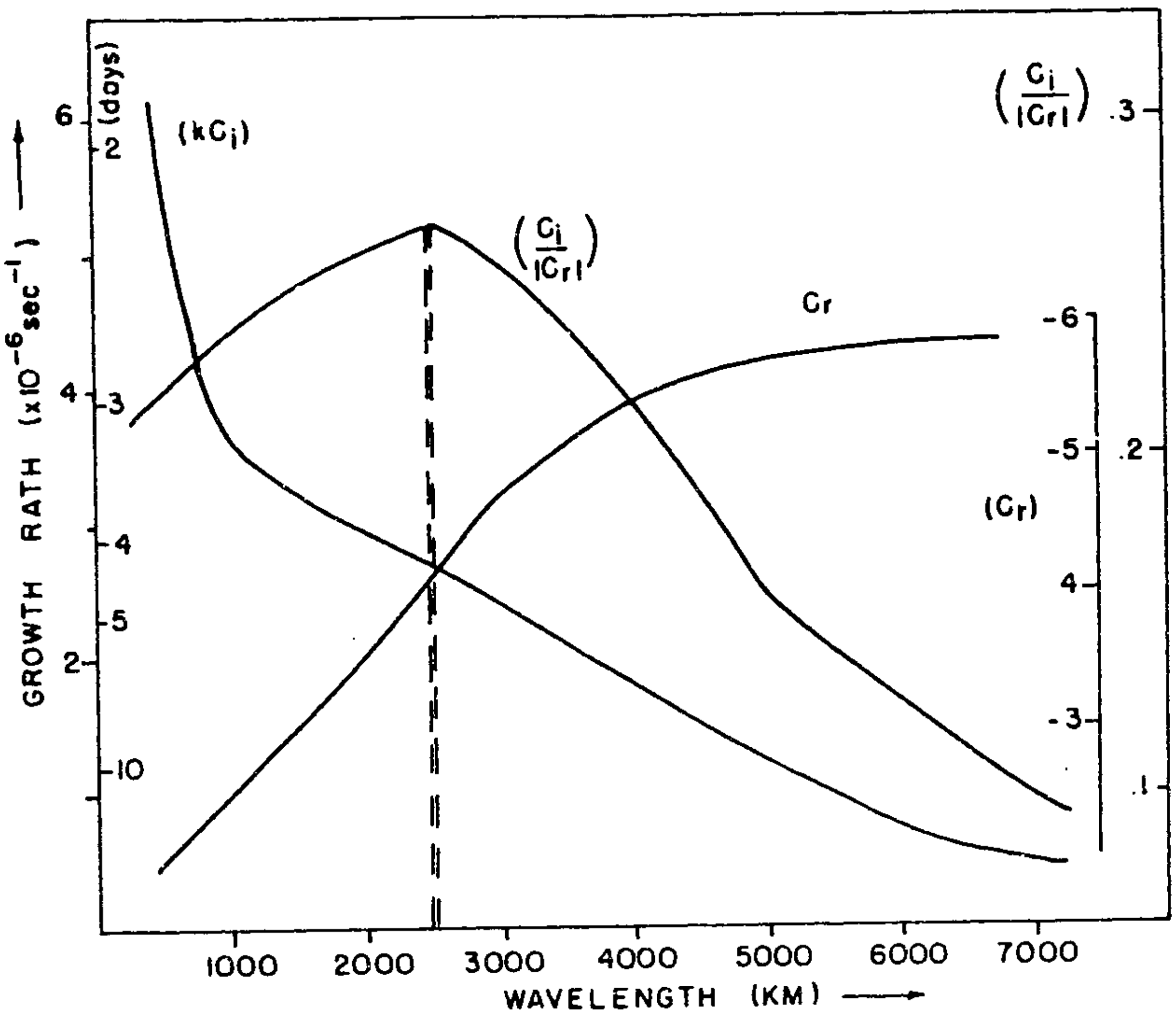

Figure 5.2 Growth rate (kCi), phase speed (Cr) and ratio (Ci/Cr) versus wavelength for the observed vertical zonal wind profile during monsoon.

reasonable agreement with the wavelength and the phase speed of the observed monsoon depressions.

The amplitude and phase structure of ψ for the most dominant mode (wavelength = 2500 km) is shown in Figure 5.3. The amplitude is maximum in the middle level. The amplitude at the lowest level is only half of its maximum value at the middle level. At the lower levels, the amplitude structure of the analytical perturbation is not in agreement with the structure of the observed monsoon depressions. The maximum amplitude of the observed monsoon depressions is found to be in the lowest layers. This discrepancy is removed when we consider the observed profile of mean zonal wind, $\bar{U}(y,z)$, which has horizontal and vertical shears.

5.3 The Case of Horizontal and Vertical Shear

For making the instability analysis of the horizontally and vertically shearing monsoon flow, $\bar{U}(y,z)$, we have followed the initial value approach described in Chapter 2. Cumulus heating by the deep clouds is parameterized by the quasi-equilibrium assumption described in Chapter 4.

The step wise procedure for making these calculations may be briefly stated as follows:

i) Calculate the values of $\lambda_1, A_{D2}, A_{D4}, B_{22}, B_{24}, B_{42}, B_{44}, \eta_{d,4}, \eta_{d,5}$ for the mean monsoon atmosphere. The mathematical expressions for these quantities is given in Appendix A.

ii) Assume an arbitrary perturbation of $\psi(y,z) = 1$

iii) Solve the equations (4.2.24) and (4.2.25) to obtain W_2 and W_4

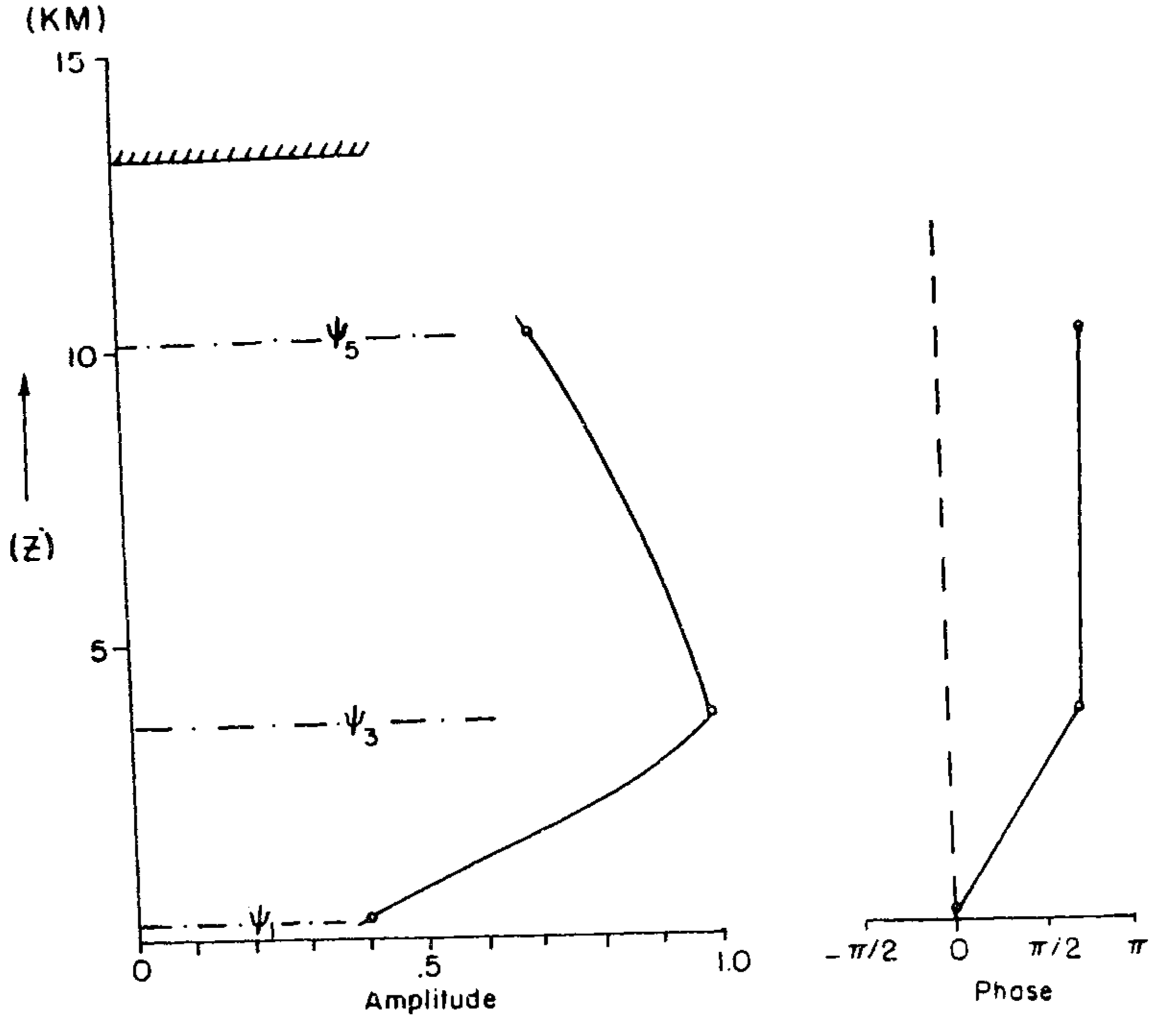

Figure 5.3 Amplitude and phase structure of the perturbation of wavelength 2500 km.

We have used a matrix inversion subroutine to solve this system of coupled elliptic equations.

iv) Obtain the values of M_2, M_4 and D_5 from (4.3.35) and (4.3.36).

v) Integrate the equations (4.2.14) through (4.2.22). The numerical scheme for integrating these equations was exactly the same as described in Chapter 2. The meridional extent of the domain was between 5N and 28.75N. No inflow or outflow was permitted through the northern and southern boundaries of the domain.
The boundary conditions on the vertical velocity were
(see Figure 4.1):

$$W_0 = W_E$$

$$M_0 = W_6 = M_6 = 0$$

vi) Repeat the steps iii) through v) for 100 time steps.

vii) Calculate the values of growth rate, ν , and phase speed, C , at each grid point, using the expressions given by (2.5) and (2.6).

viii) Check for the convergence of the values of growth rate, ν , and phase speed, C , for the whole domain. If ν and C have not converged, go back to step iii) and continue the integration. If ν and C have converged to their constant values at all the grid points, further integration is discontinued.

Figure 5.4a shows the plots of growth rate, (kC_i), phase speed, (C_r) , and the ratio (C_i/C_r) for a range of wavelengths. Maximum values of growth rates are found for the smallest values of the horizontal wavelengths. The criteria based on the ratio (C_i/C_r) suggests that the perturbation with the wavelength of 3000 km may be the most dominant perturbation. The maximum value of (C_i/C_r) for the 3000 km perturbation occurs due to very small value of its phase speed. In this case, the application of the criteria based on the ratio (C_i/C_r) may be questionable.

For the case of Ekman pumping = 0, plots of (kC_i), (Cr) and (C_i/C_r) are shown in Figure 5-4b. In this case, growth rate (kC_i) and the ratio (C_i/C_r) are maximum for the smallest scale. Comparison of Figure 5.4a and 5.4b suggests that the reduction in the phase speeds of the perturbations may be due to the addition of the Ekman pumping at the lowest boundary. It may be recalled from section 4.6 that, in the case of the resting atmosphere, surface friction is essential for the existence of growing modes. For vertically shearing flow, the structure of the divergence field depends upon the phase relationships among the internal vertical velocities generated by: a) The differential vorticity advection and thermal advection, b) surface friction, and c) cumulus heating. Since the structure of these vertical velocity fields is wavelength dependent, the magnitudes of the growth rate and the phase speed depend upon: a) Structure of the mean state (i.e., $\overline{U}$, $\partial\overline{U}/\partial z$, $\partial\overline{S}/\partial z$), and b) wavelength of the perturbation. Due to the complexity of the QEA parameterization, it has not been possible to isolate the effects of each factor in analytical form, and therefore, we have presented the results of numerical integrations of linearized perturbation equations.

Since the wavelength of the monsoon depressions is in the range 2000-3000 km, we have made a detailed analysis of the structure and energetics of the computed perturbations for the wavelength 2000 km, 2500 km

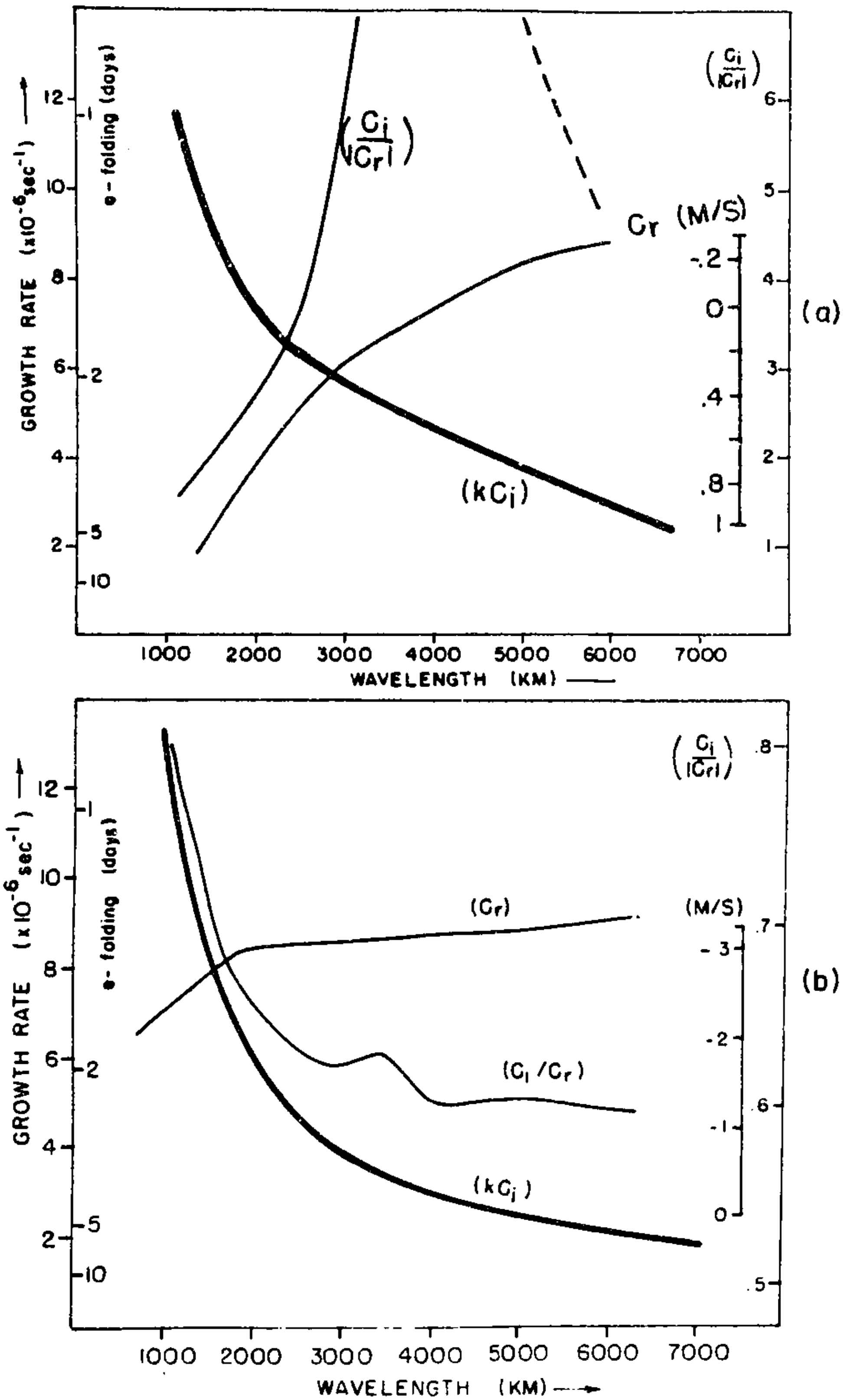

Figure 5.4. Growth rate (kCi), phase speed (Cr) and ratio (Ci/Cr) for the observed monsoon zonal wind U(y,z). (a) with Ekman pumping, (b) without Ekman pumping.

and 3000 km. The structure and energetics for the perturbations of these wavelengths were found to be nerarly the same. For the case of the Ekman pumping = 0, we have presented, in the following section, the structure and energetics for the 2500 km perturbation.

5.3.1 Structure of the computed perturbation

Figure 5.5 shows the latitude-height cross-section of the amplitude of ψ . The perturbation has appreciable vertical structure up to 10 km in vertical. The amplitude maximum is close to the observed location of the monsoon depressions. Vertical amplitude structure is also in agreement with the observations of Krishnamurti et.al. (1975). The westward phase speed of the computed perturbations is comparable to the observed phase speed of the monsoon depressions.

In order to understand the possible mechanisms which produce maximum amplitude between 20N and 25N, we carried out the barotropic instability analysis of the zonal wind at each level. It was found that for the case of $\frac{\partial U}{\partial z} = 0$ and $U(y)$ at each level equal to $U(y)$ at z_3 (3.64 km), the maximum amplitude occurred between 20N and 25N. The results of a combined CISK-barotropic instability analysis of the zonal wind at z_3 also showed that the amplitude was a maximum between 20N and 25N. It may therefore be suggested that the occurrence of maximum amplitude between 20N and 25N may be primarily due to the barotropic instability of the flow at 3.64 km. However, for the barotropic case and the CISK-barotropic case, the amplitude, at a given latitude, was a maximum at the highest level z_5 . The amplitude structure shown in Figure 5.5, which is similar to the structure of the observed monsoon depressions, occurred only when we considered the combined CISK-barotropic-baroclinic instability.

Figure 5.6 shows the longitude-height cross-section of the structure of the perturbation of wavelength 2500 km. The maxima of vertical velocity is found to be ahead (west) of the trough. This agrees with the conclusions of Krishnamurti et.al. (1975). The trough and the ridge lines slope towards the east in the vertical, which is also in agreement with the observed slope of the monsoon depressions. Krishnamurti et.al. (1975) have shown that the monsoon depression has a cold-core in the lower layers and a warm-core in the upper layers. The computed perturbations do not have such thermal structure. Warm advection takes place ahead (west) of the trough and the rising motions occur in the warmer sector of the wave. We believe that the observed low-level cold-core may be due to the cooling caused by the evaporation of the falling rain. We have not included this effect in our model.

It may be recalled from the sections 4.7 and 5.3 that if cumulus heating is parameterized by QEA, in the presence of vertical shear, maximum growth rate occurs for the smallest scale. However, if $\frac{\partial U}{\partial z} = 0$ and heating was parameterized by QEA, for the horizontally shearing flow at z_3, the maximum growth rate occurred for a wavelength of intermediate scale (wavelength = 2000 km).

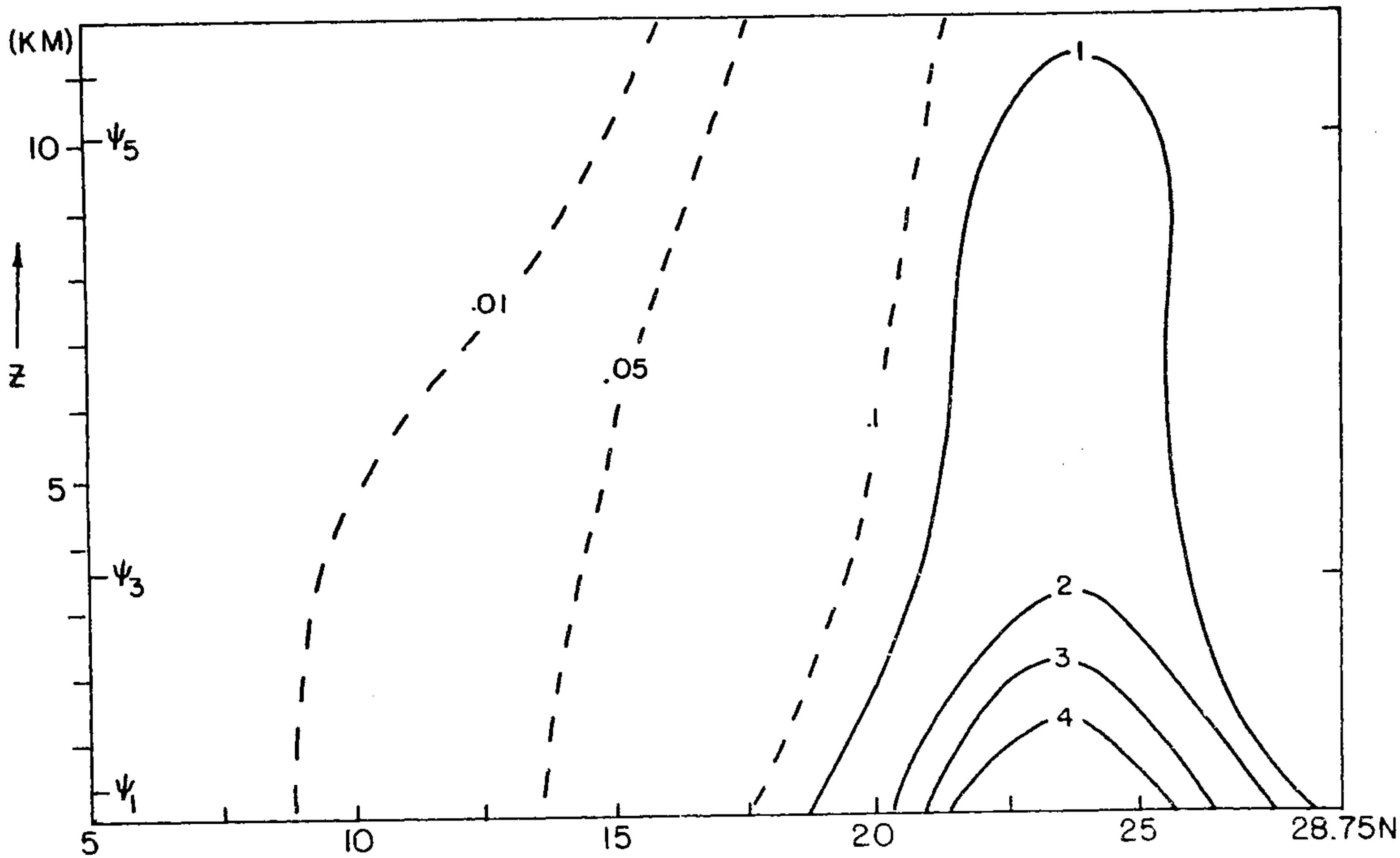

Figure 5.5 Latitude-height cross-section of the amplitude of (ψ) for the perturbation of wavelength 2500 km.

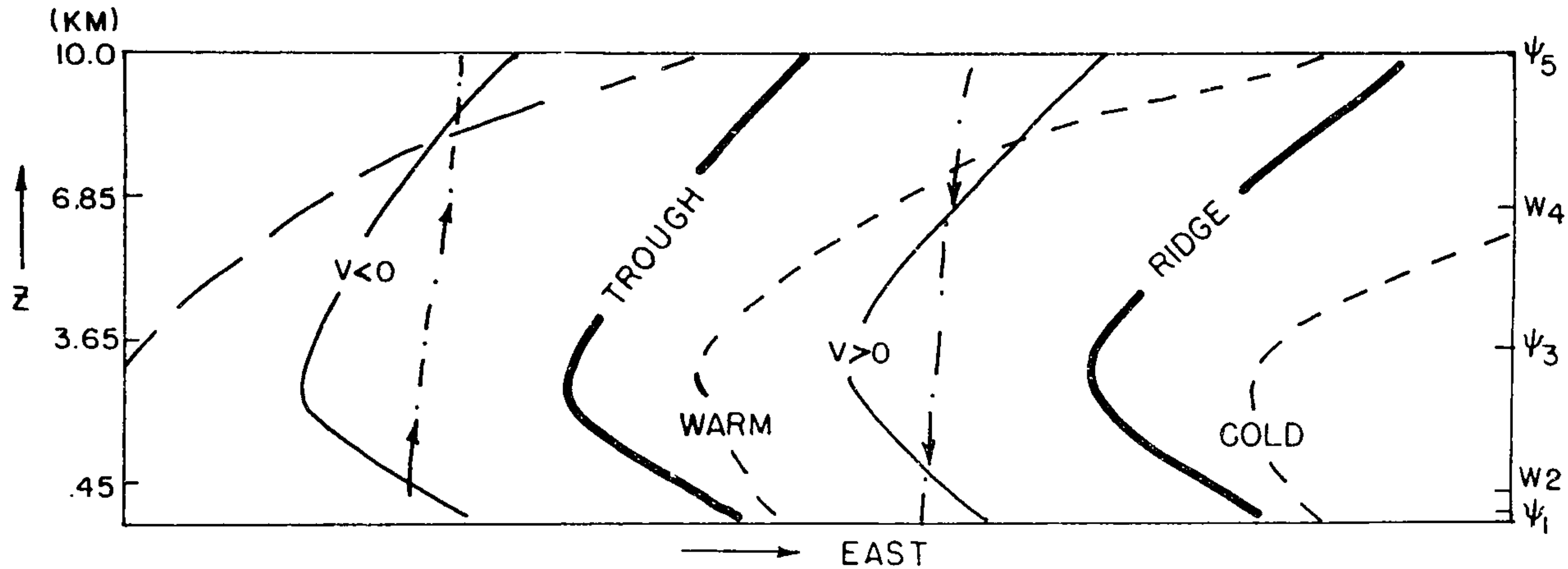

Figure 5.6 Longitude-height cross-section for the perturbation of wavelength 2500 km.

5.3.2 Energetics of the computed perturbation

For the three-layer model described in section 4.2.1, energy equations may be given as:

$$\frac{\partial K'}{\partial t} = C(KZ, KE) + C(AE, KE) - \mathcal{E}$$

$$\frac{\partial P'}{\partial t} = C(AZ, AE) - C(AE, KE) + C(QE, AE)$$

where K' is the eddy kinetic energy, P' is the eddy potential energy, $\mathcal{E}$ is the dissipation of eddy kinetic energy and $C(QE, AE)$ is the conversion from heating to the eddy available potential energy. Other symbols are the same as defined in section 4.2.1. 'r' and 'i' are subscripts for real and imaginary values.

$$K' = \frac{1}{2D}\int\left[\int\left\{k^2\left(\Psi_{rj}^2 + \Psi_{ij}^2\right) + \left(\frac{\partial \Psi_{rj}}{\partial y}\right)^2 + \left(\frac{\partial \Psi_{ij}}{\partial y}\right)^2\right\}\rho_j\, dz_j\right]_{j=1,3,5} dy$$

$$P' = \frac{f_0}{2D}\int\left[\int\left\{d_j\left(\bar{S}_{j+1} - \bar{S}_j\right)^{-1}\left(S_{rj}^2 + S_{ij}^2\right)\right\}\rho_j\, dz_j\right]_{j=1,3,5} dy$$

$$C(KE, KZ) = \frac{k}{2D}\int\left\{\frac{\partial \bar{U}_j}{\partial y}\left(\Psi_{ij}\frac{\partial \Psi_{rj}}{\partial y} - \Psi_{rj}\frac{\partial \Psi_{ij}}{\partial y}\right)\rho_j\, dz_j\right\}_{j=1,3,5} dy$$

$$C(AZ, AE) = \frac{f_0 k}{2D}\int\left[\int\left\{d_j\frac{\partial \bar{S}_j}{\partial y}\left(\bar{S}_j - \bar{S}_{j+1}\right)^{-1}\left(\Psi_{rj} S_{ij} - \Psi_{ij} S_{rj}\right)\right\}\rho_j\, dz_j\right]_{j=1,3,5} dy$$

$$\mathcal{E} = \frac{f_0 \epsilon_p}{2D}\int\left\{k^2\left(\Psi_{r1}^2 + \Psi_{i1}^2\right) + \left(\frac{\partial \Psi_{r1}}{\partial y}\right)^2 + \left(\frac{\partial \Psi_{i1}}{\partial y}\right)^2\right\}_{j=1,3,5} dy$$

$$C(AE,KE) = \frac{f_0}{2D}\int\left\{\begin{aligned} &W_{r2}\left(\alpha_1 S_{r1} + \alpha_3 S_{r3}\right) + W_{i2}\left(\alpha_1 S_{i1} + \alpha_3 S_{i3}\right) \\ &+ W_{r4}\left(\alpha_3 S_{r3} + \alpha_5 S_{r5}\right) + W_{i4}\left(\alpha_3 S_{i3} + \alpha_5 S_{i5}\right)\end{aligned}\right\} dy$$

$$C(QE,AE) = \frac{f_0}{2D}\int\left\{\begin{aligned} &M_{r2}\left(\alpha_1 S_{r1} + \alpha_3 S_{r3}\right) + M_{i2}\left(\alpha_1 S_{i1} + \alpha_3 S_{i3}\right) \\ &+ M_{r4}\left(\alpha_3 S_{r3} + \alpha_5 S_{r5}\right) + M_{i4}\left(\alpha_3 S_{i3} + \alpha_5 S_{i5}\right)\end{aligned}\right\} dy$$

Figure 5.7a shows the energy diagram for the computed perturbation of 2500 km wavelength. Figure 5.7b shows the energy diagram presented by Krishnamurti et.al. (1975). These authors have stated that the presently available network was found to be inadequate for the computation of the energy transformations from the observations of a single case study. The energy diagram of Figure 5.7b was prepared from the data generated by numerical weather prediction from a multi-level primitive equation model. The primary difference between the energetics of the computed linear perturbations and the energetics based on the results of integration of multi-level model, is found in the baroclinic conversions. The computed perturbations are found to be baroclinically damped, whereas the energy diagram given by Krishnamurti et.al. shows that the zonal available potential energy is transformed to the eddy available potential energy. The energy transformations from eddy available potential energy to eddy kinetic energy and from zonal kinetic energy to eddy kinetic are nearly the same in Figures 5.7a and 5.7b. The largest conversions occur from eddy available potential energy to eddy kinetic energy. The dominant energy source for the generation of the eddy available potential energy is the condensational heating.

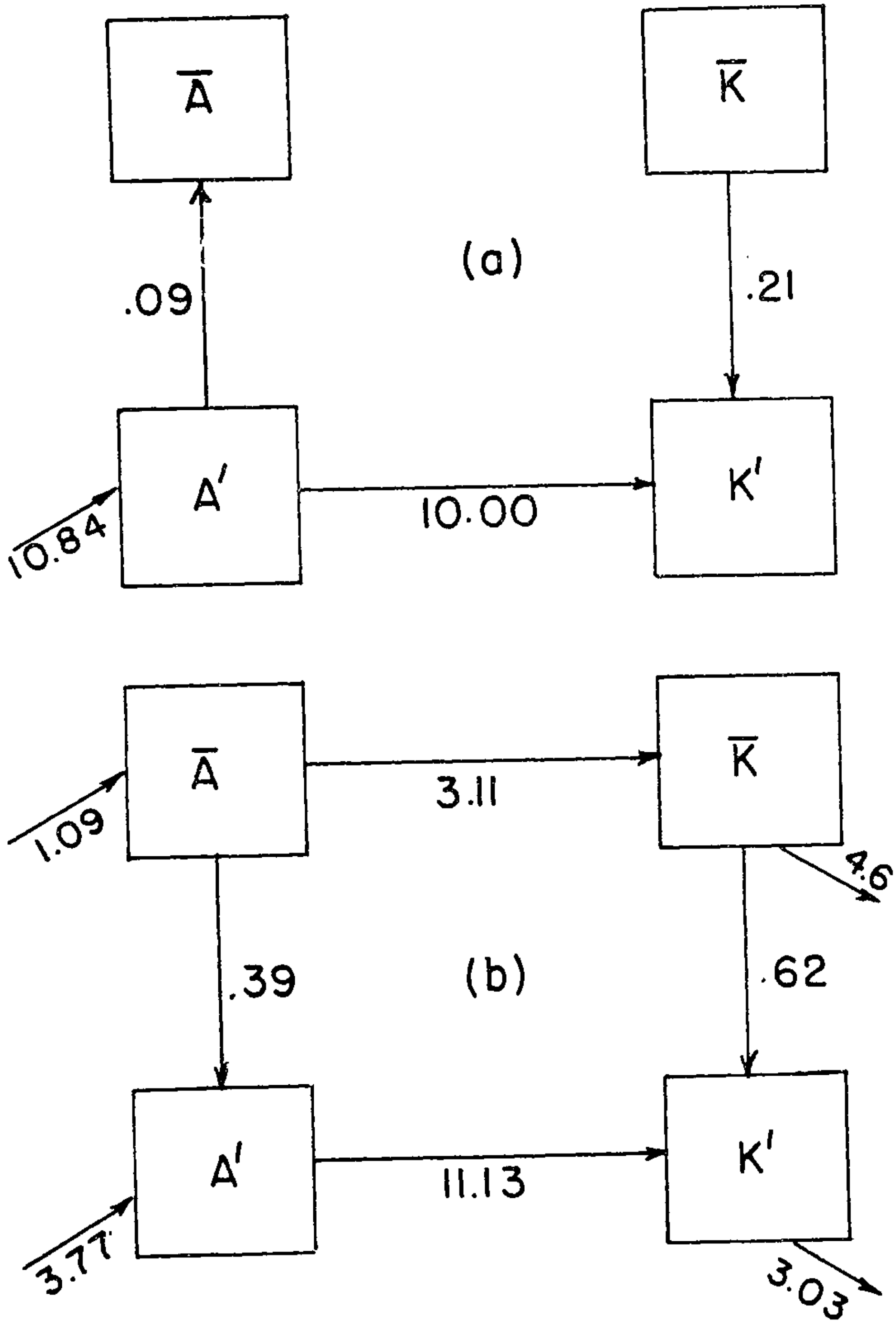

Figure 5.7 Energy transformations for (a) computed perturbation of wavelength 2500 km, and (b) results of Krishnamurti et. al (1975).

The conversion from zonal kinetic energy to eddy kinetic energy is relatively small in both the cases. Comparison between Figures 2.6 and 5.7 highlights the important role of moist-convective heating for the energetics of the monsoon depressions.

CHAPTER 6. SUMMARY AND CONCLUSIONS

The monsoon depressions which form during the monsoon season over the Bay of Bengal and move westward over India, are one of the most important components of the monsoon circulation. Their wavelength is about 2000-3000 km, and they move towards the west with a phase speed of about 3 m/s. They account for the major portion of the monsoon rainfall. The purpose of this thesis is to investigate instability mechanisms which may be responsible for the growth and maintenance of these depressions.

The mean monsoon zonal flow has appreciable horizontal and vertical shear, and the potential vorticity of the flow has maxima on isentropic surfaces, indicating the possibility of internal jet instability. We have examined the barotropic-baroclinic instability of the monsoon zonal flow, using a ten-layer quasi-geostrophic model. It is found that the most unstable mode has a wavelength of 3000 km and a westward phase speed of 15 m/s. The amplitude of the perturbation is confined only at 150 mb, and falls off rapidly at the lower levels. Computations of energy conversion have shown that most of the conversion is from KZ to KE and very small conversion from AZ to AE , thus indicating the importance of barotropic instability to the dominance of such perturbations. In fact, the barotropic instability analysis of the 150 mb zonal wind alone, yields a growth rate versus wavelength curve which is similar to the combined barotropic-baroclinic analysis of $\overline{U}(y, p)$. This result indicates that, in the absence of condensation, the fastest growing perturbation corresponds to the most unstable mode of the barotropically unstable upper level zonal wind. Since the amplitude of the perturbation is concentrated at the upper levels only, the scale and the structure of the perturbations remain the same whether in the model a vertical wall is put at 28.75N, or is put at 40N, together with a 600 mb high Himalayan plateau between 28.75N and 40N.

The results of the perturbation analysis explain the occurrence of the westward-moving waves at 200 mb. They also demonstrate that barotropic-baroclinic instability alone cannot explain the formation of the monsoon depressions, whose amplitude maxima are at the lower levels and which have appreciable amplitude in lower troposphere.

The next step in the study is an exploration of the role of the CISK mechanism in conjunction with barotropic and/or baroclinic instability mechanisms, because the latent heat of condensation may be the primary driving mechanism for monsoon depressions. We are thus faced with the important, but yet unresolved, problem of the parameterization of the effects of moist convection and consideration of the interactions between the large-scale circulation and cumulus convection.

We have examined the instability characteristics of a vertically-sheared mean monsoonal flow, using empirical vertical distributions of CISK-type heating. In this formulation, heating is made proportional to the Ekman pumping, or to the vertical velocity at the top of the lowest layer. In either case, the wavelength of the fastest growing mode depends upon the vertical distribution function for cumulus heating (the so-called η profile). We have experimented with several vertical distribution functions. One of the noteworthy results is that the horizontal scale of the most unstable mode is larger for those η profiles that provide heating to the larger vertical depths of the atmosphere. This is seen to be consistent with the concept of the Rossby radius of deformation in the theory of geostrophic adjustment, in which it is shown that the scales of the horizontal and the vertical circulations are interrelated through static stability and rotation.

In order to make the intercomparison among different η profiles, η values were scaled in such a way that the total heating realised by the atmosphere remained the same in each case, and thus, we could compare the effects of changing only the vertical distribution. It was also found that when heating was made proportional to the vertical velocity at the top of the lowest layer, the magnitude of the growth rates was increased when we added the Ekman pumping at the lowest level.

The purpose of these calculations was not so much to simulate the growth of the monsoon depressions as to point out that one can simulate several kinds of tropospheric tropical disturbances by choosing suitable η profiles. Since the choice of η is largely arbitrary, it points to the need of a theory for deducing the effects of the moist convection.

We have applied the quasi-equilibrium assumption of Arakawa and Schubert to parameterize the effects of moist convection. This scheme involves some questionable assumptions concerning the interaction of the large-scale with the cumulus ensemble, and concerning the structure and life cycle of the cumulus clouds. It offers, nonetheless, a rational closure hypothesis to determine, from the large-scale variables, the effects of a cumulus ensemble. Therefore, the application of this scheme merits discussion.

We have described the actual procedure used to calculate the cloud mass flux from the large-scale variables. We have considered only two kinds of clouds: (a) the non-precipitating, liquid water-detraining shallow clouds, and (b) the fully precipitating deep clouds. We have used a three-layer quasi-geostrophic model to perform the instability analysis. Since a cloud type, in a discrete model, is characterized by its level of detrainment, we can only consider two kinds of clouds in a three-layer model. The integral equation for the mass flux at the base of the clouds is now reduced to two algebraic equations, the solution for which gives the mass flux at the base of the shallow and the deep clouds.

Instability analysis of a resting atmosphere with the three-layer quasi-geostrophic model has shown that the growth rate versus wavelength curve remains essentially the same for two cloud types as for deep clouds only. The effect of the shallow clouds, which detrain moisture and liquid water in the lower layer, is only to change the structure of the eigenfunctions. For most of the later analysis, only the deep cloud model is used.

We have also studied the growth of perturbations in a two-layer model. In this case, the application of the quasi-equilibrium assumption determines the mass flux at the base of the cloud. The mass flux is found to be proportional to the vertical velocity at the middle level. The constant of proportionality (η) depends upon the temperature and moisture structures of the atmosphere. If $\eta > 1$, the wavelength of the fastest growing mode is proportional to the Rossby radius of deformation; the constant of proportionality is $(\eta - 1)$. To state this result in another way, the wavelength of the fastest growing mode is the Rossby radius of deformation itself. However, due to cumulus heating, the Brunt-Vaisalla frequency, N^2, (which is a measure of the vertical stratification) is now scaled by $(\eta - 1)$. The actual value of the growth rate of the fastest growing mode, however, is found to be infinite. Since a two-layer model has only one vertical scale, there is only one corresponding horizontal scale which is the Rossby radius of deformation, which corresponds to the horizontal scale of the most unstable mode. For this mode, due to the effects of cumulus heating, the internal vertical velocity at the mid-level becomes infinite, and the assumptions of hydrostatic balance and quasi-geostrophic balance break down.

In all the analyses presented in the thesis, heating is considered a perturbation variable and is assumed to have a sinusoidal variation in the longitudinal direction. This is certainly a shortcoming of the study, because in observed synoptic waves precipitation is confined mainly to the convergent regions of the waves. This assumption has been made to simplify the mathematical analysis, because the specification of heating over only a certain portion of the wave, and no specification of heating over the remaining portion of the wave makes the problem nonlinear, and would be difficult to incorporate in a linear stability analysis. Due to the assumption of sinusoidal heating, the horizontal scale of the region over which heating occurs is only half that of the wavelength of the perturbation. An equal amount of cooling takes place over the remaining half of the wavelength. The effect of this assumption, therefore, may be to enhance the rate of generation of available potential energy and therefore, to overestimate the magnitude of the growth rate. This model shortcoming may be partly corrected by introducing a mean heating term, which can compensate for the cooling effects of the sinusoidal heating perturbation. However, the incorporation of mean heating would involve the determination of the mean meridional Hadley circulation and the parameterization of the mean cloud mass flux $\overline{M}_c$. This aspect of the study is beyond the scope of the thesis.

Following Charney (1971), in one case we have considered a two-layer model with heating parameterized by the QEA in which the heating is confined to a finite region, and no heating occurs outside this region. For a resting atmosphere, the results are similar to the case when the heating is sinusoidal insofar as the character of the growth rate curve is concerned, but the horizontal scale of the growing perturbation is reduced in the former case.

Our analysis has clarified the earlier results of Charney and Eliassen (1964) and of Israeli and Sarachik (1973). We have concluded that for a two-layer model where heating is made proportional to the Ekman pumping, the smallest scale would be the fastest growing mode, whereas if the heating is made proportional only to the internal vertical velocity, the maximum growth rate would occur for a finite scale, but the magnitude of the growth rate would be infinite. Since Charney and Eliassen took the heating to be proportional to a linear combination of the Ekman pumping and the internal vertical velocity, they obtained both branches of the growth rate curves. It may, of course, be possible to obtain a short wave cut-off, when the heating is proportional to the Ekman pumping, by an artificial choice of the η profile; i.e., where $\eta = 0$ in the lowest layer. This was done by Chang and Williams (1975). It was pointed out by Charney (1973) that the small scales are stabilized due to the 'inefficiency' of the Ekman pumping at the very small scales.

We have also pointed out the inadequacy of two-layer models to study the dynamics of disturbances which have significant moist convection associated with them. We have examined the equivalence of the so-called wave-CISK parameterization (in which the heating is parameterized in terms of the vertical velocity at the top of the lowest layer, and is arbitrarily distributed in the vertical) with the parameterization by the QEA. For a three-layer model of the resting atmospheres, we are able to derive an equivalent η profile for the QEA parameterization. The novel feature of the QEA parameterization turns out to be that the heating function is mode-dependent, whereas that for arbitrary η profiles it remains the same for all wavelengths.

It was also found that, for a resting atmosphere, if cumulus heating was parameterized by QEA, there were no growing solutions in the absence of Ekman pumping or in the absence of Rayleigh friction in the lowest layer. If there is no surface friction, and if the disturbance is not propagating, it is not possible to generate internal vertical velocities in a resting atmosphere. Since heating is parameterized in terms of internal vertical velocity, heating is not realized in the absence of surface friction, and thus, there are no growing modes. However, in the presence of surface friction, the frictional convergence associated with the infinitesimal perturbations produces Ekman pumping and internal vertical velocity. Since heating is parameterized in terms of internal vertical velocity, a perturbation may grow if the vertical structure of the internal vertical velocity of the perturbation is such that the application of QEA leads to a net heating of the atmosphere.

We have studied the instability of a resting atmosphere with a three-layer quasi-geostrophic model where cumulus heating is parameterized by QEA and Ekman pumping specifies the lower boundary condition for vertical velocity. It is found that the maximum growth rate occurs for a wavelength of intermediate scale. Maximum growth rate occurs for that scale for which the vertically integrated net heating is a maximum.

We have also studied the instability of a shearing flow with the QEA parameterization. In the presence of vertical shears, the cloud mass flux depends on the internal vertical velocity, and the horizontal advections of temperature and moisture. The cloud mass flux (and therefore, the heating) becomes inversely proportional to the wavelength of the perturbation, and therefore we obtain maximum growth rate for the smallest scales. Only in the unlikely case that the contribution of the horizontal advection of entropy to the cloud work function vanishes, will maximum growth rates occur at intermediate scales.

We have hypothesized that among all the growing modes the most dominant perturbation will be the one for which the ratio of the period and the e- folding time is a maximum. The horizontal scale of the perturbation, which is found to be most dominant according to this criteria, agrees reasonably well with the horizontal scale of the observed tropical waves.

Finally, we examine the instability of horizontally and vertically shearing monsoonal zonal wind, using the QEA parameterization of the moist convection in a three-layer quasi-geostrophic model. Due to the non-separability of the perturbation equations, we follow the initial value approach to the instability analysis in which the linearized perturbation equations are numerically integrated in time. We have examined those waves which have horizontal scales in the range 2500–3500 km, which is a reasonable scale for monsoon depressions. We have compared the structure and the energetics of the computed perturbations and the observed monsoon depression by Krishnamurti, et.al. (1975). In the absence of the Ekman pumping, the westward phase speeds of the computed perturbations are comparable to the actual phase speeds of observed monsoon depressions. However, when the effect of the Ekman pumping is added, the phase velocity is reduced. The amplitudes of the computed perturbations are a maximum between 20N and 25N, which is reasonably close to the observed location of the most cyclogenetic area in the Bay of Bengal. The model perturbations have significant amplitudes up to 10 km, and the amplitudes are maximum in the lowest layers. This is in reasonable agreement with the observed amplitude structure of the monsoon depressions. The computed perturbations are found to have a warm-core, whereas the observed monsoon depressions studied by Krishnamurti, et.al. (1975) are found to have a cold-core in the lower layers, and a warm-core in the upper layers. If the cold-core exists -- and there is some doubt that it does (Sikka, personal communication) -- it may be due to the cooling caused by the evaporation of the falling rain. This effect has not been included in our model.

The dominant energy transformation for the computed perturbations is found to be from eddy available potential energy to eddy kinetic energy. The primary source of energy is condensational heating. The transformation from zonal available potential energy to eddy available potential energy is small but negative, indicating that baroclinic instability is not important. For the computed perturbations, which are being driven primarily by cumulus heating, the barotropic conversion is found to be from zonal kinetic energy to eddy kinetic energy. Krishnamurti, et.al, also found that the major energy exchange is from eddy available potential energy to eddy kinetic energy and the conversion from zonal available potential energy to eddy available potential is relatively small. The barotropic energy exchange in their case also was from zonal kinetic energy to eddy kinetic energy.

The structures of the computed perturbations suggest that the barotropic instability of the middle layer may be responsible for the initial growth of the perturbation and subsequently condensational heating becomes the dominant forcing. The results further suggest that the magnitudes of the growth rates and the dominant energy transformations are determined by the CISK, the horizontal amplitude structure is determined by the horizontal shears, and the vertical amplitude structure is determined by the combined effects of vertical shear and condensational heating. These suggestions are made on the basis of the results of a linear perturbation model and further observational and theoretical studies will be needed to explain actual cyclogenesis over the Bay of Bengal. In particular, it may be desirable to investigate the moisture supply provided by the Bay of Bengal, as well as the details of the surrounding topography to arrive at an actual explanation.

From the results of the present study, it may be hypothesized that the primary role of the terrain is to produce a mean circulation (viz., monsoon trough at the foothills of the Himalayas) which is barotropically unstable at the lower levels and which thus provides the 'triggering' mechanism for the monsoon depressions. These, however, are amplified and maintained by latent heat of condensation.

Reasonable agreement in structure and energetics between the computed and the observed perturbations suggests that Conditional Instability of the Second Kind is the primary driving mechanism for the growth of monsoon depressions.

Appendix A

Equations (4.3.19) and (4.3.24) may be written as:

$$\frac{\partial h_1'}{\partial t} - \frac{\partial h_3^{*\prime}}{\partial t} = 0 \tag{A.1}$$

$$f_1 \frac{\partial h_1'}{\partial t} + f_2 \frac{\partial h_3'}{\partial t} + f_3 \frac{\partial h_3^{*\prime}}{\partial t} + f_4 \frac{\partial h_5'}{\partial t} + f_5 \frac{\partial h_5^{*\prime}}{\partial t} = 0 \tag{A.2}$$

Since $\quad \dfrac{\partial h_3^{*\prime}}{\partial t} = (1+\gamma_3)\, \dfrac{\partial S_3'}{\partial t}$

and $\quad \dfrac{\partial h_5^{*\prime}}{\partial t} = (1+\gamma_5)\, \dfrac{\partial S_5'}{\partial t}$

we may write (A.1)and (A.2) from (4.2.9) and (4.2.10) for the discrete model given in Fig. 4.1:

$$\left[\left\{(m_B(s) + m_B(d)) - W_2'\right\}\left(\frac{\bar{h}_2 - \bar{h}_1}{\rho_1 \Delta z_1}\right) - \bar{U}_1 \frac{\partial h_1'}{\partial x} - \frac{\partial \bar{h}_1}{\partial y}\frac{\partial \psi_1'}{\partial x}\right]$$

$$-(1+\gamma_3)\left[\frac{\left\{(m_B(s) + m_B(d)) - W_2'\right\}(\bar{S}_3 - \bar{S}_2) + \left\{\eta_{d,4}\, m_B(d) - W_4'\right\}(\bar{S}_4 - \bar{S}_3) - D_3 L\, \ell_{s,3}}{\rho_3 \Delta z_3}\right]$$

$$+ \bar{U}_3 \frac{\partial S_3'}{\partial x} - \frac{\partial \bar{S}_3}{\partial y}\frac{\partial \psi_3'}{\partial x} = 0 \tag{A.3}$$

where $D_3 = \eta_{s,3}\, m_B(s)$

which may be simplified as:

$$K_{ss}\, m_B(s) + K_{sd}\, m_B(d) = \left[W_2 K_{22} + W_4 K_{24}\right. \tag{A.4}$$

$$+ f_5(1+\gamma_5)\left[\left\{m_B(d)\,\eta_{d,4} - W_4'\right\}\frac{(\bar{S}_5-\bar{S}_4)}{\rho_5\,\Delta z_5} - \bar{U}_5\frac{\partial S_5'}{\partial x} - \frac{\partial \bar{S}_5}{\partial y}\cdot\frac{\partial \psi_5'}{\partial x}\right] = 0 \quad (A.6)$$

Rearranging the terms we get:

$$m_B(s)\,K_{ds} + m_B(d)\,K_{dd} = K_{42}\,W_2 + K_{44}\,W_4 + XB \quad (A.7)$$
$$\equiv F_d$$

where
$$K_{42} = \frac{f_1(\bar{h}_2-\bar{h}_1)}{\rho_1\,\Delta z_1} - \frac{f_2(\bar{h}_3-\bar{h}_2)}{\rho_3\,\Delta z_3} - \frac{f_3(1+\gamma_3)(\bar{S}_2-\bar{S}_3)}{\rho_3\,\Delta z_3}$$

$$K_{44} = \frac{f_2(\bar{h}_4-\bar{h}_3)}{\rho_3\,\Delta z_3} + \frac{f_3(1+\gamma_3)(\bar{S}_4-\bar{S}_3)}{\rho_3\,\Delta z_3} - \frac{f_4(\bar{h}_4-\bar{h}_5)}{\rho_5\,\Delta z_5}$$
$$+ \frac{f_5(1+\gamma_5)(\bar{S}_5-\bar{S}_4)}{\rho_5\,\Delta z_5}$$

$$XB = \left[f_1\left(\bar{U}_1\frac{\partial h_1'}{\partial x} + \frac{\partial \bar{h}_1}{\partial y}\frac{\partial \psi_1'}{\partial x}\right) + f_2\left(\bar{U}_3\frac{\partial h_3'}{\partial x} + \frac{\partial \bar{h}_3}{\partial y}\frac{\partial \psi_3'}{\partial x}\right)\right.$$
$$+ f_3(1+\gamma_3)\left(\bar{U}_3\frac{\partial S_3'}{\partial x} + \frac{\partial \bar{S}_3}{\partial y}\frac{\partial \psi_3'}{\partial x}\right) + f_4\left(\bar{U}_5\frac{\partial h_5'}{\partial x} + \frac{\partial \bar{h}_5}{\partial y}\frac{\partial \psi_5'}{\partial x}\right)$$
$$\left. + f_5(1+\gamma_5)\left(\bar{U}_5\frac{\partial S_5'}{\partial x} + \frac{\partial \bar{S}_5}{\partial y}\frac{\partial \psi_5'}{\partial x}\right)\right] \quad (A.8)$$

Expressions for K_{ss}, K_{sd}, K_{ds}, K_{dd}, F_s and F_d are already given in (4.3.30) and (4.3.31).

Solving (A.4) and (A.7) we get $m_B(s)$ and $m_B(d)$:

$$m_B(s) = A_{s2} W_2' + A_{s4} W_4' + A_{ss}$$

where

$$A_{ss} = a_1 \frac{\partial \psi_1'}{\partial x} + a_2 \frac{\partial \psi_3'}{\partial x} + a_3 \frac{\partial \psi_5'}{\partial x} + a_4 \frac{\partial s_1'}{\partial x} + a_5 \frac{\partial s_3'}{\partial x}$$

$$+ a_6 \frac{\partial s_5'}{\partial x} + a_7 \frac{\partial h_1'}{\partial x} + a_8 \frac{\partial h_3'}{\partial x} + a_9 \frac{\partial h_5'}{\partial x} \qquad \text{(A.9)}$$

and

$$m_B(d) = A_{D2} W_2' + A_{D4} W_4' + A_{DD}$$

$$A_{DD} = b_1 \frac{\partial \psi_1'}{\partial x} + b_2 \frac{\partial \psi_3'}{\partial x} + b_3 \frac{\partial \psi_5'}{\partial x}$$

$$+ b_4 \frac{\partial s_1'}{\partial x} + b_5 \frac{\partial s_3'}{\partial x} + b_6 \frac{\partial s_5'}{\partial x}$$

$$+ b_7 \frac{\partial h_1'}{\partial x} + b_8 \frac{\partial h_3'}{\partial x} + b_9 \frac{\partial h_5'}{\partial x} \qquad \text{(A.10)}$$

where $$A_{s_2} = \frac{K_{22} K_{dd} - K_{sd} K_{42}}{K_{ss} K_{dd} - K_{sd} K_{ds}}$$

$$A_{s4} = \frac{K_{24} K_{dd} - K_{sd} K_{44}}{K_{ss} K_{dd} - K_{sd} K_{ds}}$$

$$A_{D2} = \frac{K_{42} K_{ss} - K_{24} K_{ds}}{K_{ss} K_{dd} - K_{sd} K_{ds}}$$

$$A_{D4} = \frac{K_{44} K_{ss} - K_{ds} K_{24}}{K_{ss} K_{dd} - K_{sd} K_{ds}}$$

Let us further define:

$$SS = K_{ss} K_{dd} - K_{sd} K_{ds}$$

$$S^* = K_{dd} / SS$$

$$I^* = K_{ss} / SS$$

$$R^* = K_{ds} / SS$$

$$J^* = K_{sd} / SS$$

$$\frac{\partial}{\partial y}(\bar{h}_j, \bar{S}_j) = (H_{jy}, S_{jy})$$

Then a_j and b_j may be given by:

$$a_1 = S^* H_{0y} - J^* f_1 H_{1y}$$

$$a_2 = -S^*(1+\gamma_3)\,\overline{S}_{3y} - J^* f_2\,\overline{H}_{3y} - J^* f_3 (1+\gamma_3)\,\overline{S}_{3y}$$

$$a_3 = -J^*\left\{ f_4\,\overline{H}_{5y} + f_5 (1+\gamma_5)\,\overline{S}_{5y}\right.$$

$$a_4 = 0$$

$$a_5 = \overline{U}_3 (S^* + J^* f_3)(1+\gamma_3)$$

$$a_6 = \overline{U}_5\, J^* f_5 (1+\gamma_5) \quad ; \quad b_6 = \overline{U}_5 \left\{ I^*(1+\gamma_5) f_5 \right\}$$

$$a_7 = \overline{U}_1 \left\{ S^* - f_1 J^* \right\} \quad ; \quad b_7 = \overline{U}_1 \left\{ f_1 I^* - R^* \right\}$$

$$a_8 = \overline{U}_3 \left\{ -f_2 J^* \right\} \quad ; \quad b_8 = \overline{U}_3 f_2 I^*$$

$$a_9 = \overline{U}_5 \left\{ -f_4 J^* \right\} \quad ; \quad b_9 = \overline{U}_5 f_4 I^*$$

$$b_1 = (I^* f_1 - R^*)\,\overline{H}_{0y} \quad ; \quad b_2 = \left\{ I^* f_2\,\overline{H}_{3y} + I^* f_3 (1+\gamma_3)\,\overline{S}_{3y} + R^*(1+\gamma_3)\,\overline{S}_{3y} \right\}$$

$$b_3 = I^* \left\{ f_4\,\overline{H}_{5y} + f_5 (1+\gamma_5)\,\overline{S}_{5y} \right\} \quad ; \quad b_4 = 0$$

$$b_5 = \overline{U}_3 \left\{ I^* f_3 + R^* \right\} (1+\gamma_3)$$

Since M_2 and M_4 are related to $m_B(s)$ and $m_B(d)$ as given by (4.1.4) and (4.1.5), we may write:

$$M_2 = m_B(s) + m_B(d) \tag{A.11}$$

$$M_4 = \eta_{d,4}\, m_B(d) \tag{A.12}$$

Substituting from (A.9) and A.10) we obtain:

$$M_2 = B_{22} W_2 + B_{24} W_4 + \mu_2 \tag{A.13}$$

$$M_4 = B_{42} W_2 + B_{44} W_4 + \mu_4 \tag{A.14}$$

where

$$\left.\begin{aligned} B_{22} &= A_{S2} + A_{D2} \\ B_{24} &= A_{S4} + A_{D4} \\ B_{42} &= A_{D2}\, \eta_{d,4} \\ B_{44} &= A_{D4}\, \eta_{d,4} \end{aligned}\right\} \tag{A.15}$$

$$\left.\begin{aligned} \mu_2 &= A_{SS} + A_{DD} \\ \mu_4 &= \eta_{d,4}\, A_{DD} \end{aligned}\right\} \tag{A.16}$$

APPENDIX B

For a deep cloud in a two-layer model (see Fig. 4.2), work function may be given as:

$$A(\lambda) = K_1 \eta_2 (h_{c,2} - h_1^*) \frac{\Delta z_1}{4} + K_3 \eta_2 (h_{c,2} - h_3^*) \frac{\Delta z_3}{4} \qquad \text{(B.1)}$$

$$\frac{\partial A}{\partial t} = 0 \qquad \text{gives}$$

$$P_1 \frac{\partial h_1'}{\partial t} + P_1^* \frac{\partial s_1'}{\partial t} + P_3 \frac{\partial h_3'}{\partial t} + P_3^* \frac{\partial s_3'}{\partial t} = 0 \qquad \text{(B.2)}$$

Following a procedure similar to the one in Appendix A, it is found that the expression for the cloud mass flux M_2 may be given as:

$$M_2 = \eta W_2 + \frac{\partial}{\partial x} \left\{ a_1 s_1' + a_2 h_1' + a_3 \qquad + a_4 h_3' + a_5 \psi_1' + a_6 \psi_3' \right\} \qquad \text{(B.3)}$$

where (see Fig. 4.2)

$$\eta = \left\{ 1 + \lambda (z_2 - z_1) \right\} \frac{T}{I}$$

$$a_j = \left\{ \frac{1 + \lambda (z_2 - z_1)}{I} \right\} C_j \qquad ; \quad j = 1, 6$$

$$T = P_1 H_{21} + P_1^* S_{21} + P_3 H_{32} + P_3^* S_{32}$$

$$I = \left\{ 1 + \lambda (z_2 - z_1) \right\} \left\{ P_1 H_{21} + P_1^* S_{21} + P_3 H_{32} + P_3^* S_{32} \right\}$$

$$+ \; P_3 R_3 \left\{ 1 + \lambda (z_3 - z_1) \right\} \left(\overline{h_3^*} - \overline{h_3} \right)$$

$$R_1 = 1/\rho_1 \Delta z_1 \quad , \quad R_3 = 1/\rho_3 \Delta z_3 \quad , \quad H_{21} = (\bar{h}_2 - \bar{h}_1) R_1$$

$$H_{32} = (\bar{h}_3 - \bar{h}_2) R_3 \quad , \quad S_{21} = (\bar{S}_2 - \bar{S}_1) R_1 \quad , \quad S_{32} = (\bar{S}_3 - \bar{S}_2) R_3$$

$$C_1 = U_1 P_1^* \quad , \quad C_2 = U_1 P_1 \quad , \quad C_3 = U_3 P_3^* \quad , \quad C_4 = U_3 P_3$$

$$C_5 = \left(P_1 \bar{H}_{1y} + P_1^* S_{1y} \right) \quad , \quad C_6 = \left(P_3 \bar{H}_{3y} + P_3^* S_{3y} \right)$$

$$P_1 = \frac{U_2}{D} \left(\frac{\eta_3 - \eta_1}{2} \right) + \frac{U_1}{\eta_2} \left\{ a(\eta_2 - \eta_1) + \frac{E}{D} \frac{(\eta_3 - \eta_1)}{2} \right\}$$

$$P_1^* = (1 + \gamma_1) \left[\frac{U_2}{D} + \frac{U_1}{\eta_2} \left\{ 1 + \frac{E}{D} \right\} - K_1 \eta_2 \right]$$

$$P_3 = \frac{U_2}{2D} (\eta_3 - \eta_1) + \frac{U_1}{\eta_2} \left\{ b(\eta_2 - \eta_1) + \frac{E}{D} \left(\frac{\eta_3 - \eta_1}{2} \right) \right\}$$

$$P_3^* = (1 + \gamma_3) \left[-\frac{U_2 \eta_3}{D} - \frac{U_1 \eta_3 E}{\eta_2 D} - K_3 \eta_2 \right]$$

$$K_1 = (g \Delta z_1) / \{ c_p T_1 (1 + \gamma_1) \}$$

$$K_3 = (g \Delta z_3) / \{ c_p T_3 (1 + \gamma_3) \}$$

$$U_1 = (K_1 + K_3) \eta_2 \quad , \quad U_2 = \left\{ K_1 (h_{c,2} - \bar{h}_1^*) + K_3 (h_{c2} - \bar{h}_3^*) \right\}$$

$$D = (z_3 - z_1) \bar{h}_3^* + (z_2 - z_1) \bar{h}_1 + (z_3 - z_2) \bar{h}_3$$

$$E = \left\{ a \bar{h}_1 + b \bar{h}_3 - \bar{h}_{c,2} \right\} (z_2 - z_1)$$

$$a = \left\{ 1 - \Delta z_1 / \left(2(\Delta z_1 + \Delta z_3) \right) \right\}$$

$$b = \left\{ \Delta z_1 / \left(2(\Delta z_1 + \Delta z_3) \right) \right\}$$

$$\eta_j = 1 + \lambda (z_j - z_1) \quad ; \quad j = 1, 3$$

$$\lambda = \left(h_{cB} - \bar{h}_3^* \right) \Big/ \left[\bar{h}_3^* (z_3 - z_1) - \left\{ h_1 (z_2 - z_1) + h_3 (z_3 - z_2) \right\} \right]$$

$$h_{cB} = \mu \bar{h}_1 + (1 - \mu) \bar{h}_1^* \quad ; \quad \mu = \bar{h}_1^* / (\bar{h}_1^* - \bar{h}_1)$$

$$h_{c,2} = \frac{1}{\eta_2} \left\{ h_{cB} + (\eta_2 - \eta_1) \left(a \bar{h}_1 + b \bar{h}_3 \right) \right\}$$

$$\frac{\partial}{\partial y} \left(\bar{h}_j, \bar{S}_j \right) = \left(\bar{H}_{jy}, \bar{S}_{jy} \right) \quad ; \quad j = 1, 3$$

$$\bar{a} = \alpha \left(\alpha_1 S_{21} + \alpha_3 S_{32} \right)$$

$$\alpha = \left\{ \left(1 + \lambda (z_2 - z_1) \right) \frac{T}{I} - 1 \right\} = (\eta - 1)$$

$$\alpha_1 = \frac{g \Delta z_1}{2 c_p T_1 f_0}$$

$$\alpha_3 = \frac{g \Delta z_3}{2 c_p T_3 f_0}$$

REFERENCES

Ananthakrishnan, R., and A.R. Ramakrishnan, 1963: Perturbations of the general circulation over India and neighborhood. Symposium on Trop. Met., New Zealand., pp. 144-159

Arakawa, A., and W.H. Schubert, 1974: Interaction of a cumulus cloud ensemble with the large-scale environment, Part I. J. Atmos. Sci., 31, pp. 674-701.

Arakawa, A., and Y. Mintz, 1974: The UCLA general circulation model. Notes distributed at the workshop, 25 March- 4 April 1974, Dept. of Meteorology, UCLA.

Arakawa, A., and W. Chao, 1975: Study of Conditional Instability of second kind with Arakawa-Scubert cumulus parameterization theory. (unpublished manuscript)

Betts, A.K., F.J. Dugan and R.W. Grover, 1974: Residual errors of the VIZ radiosonde hygristor as deduced from observations of sub-cloud layer structure. Bull. Amer. Meteor. Soc., 55, pp. 1123-1125.

Brown, J.A., 1969: A numerical investigation of hydrodynamic instability and energy conversions in the quasi-geostrophic atmosphere. J. Atmos. Sci., 26, pp 352-365.

Chang, C.P., 1971: On the stability of low-latitude quasi-geostrophic flow in a conditionally unstable atmosphere. J. Atmos. Sci., 28, pp. 270-274.

Chang, C.P., and R.T. Williams, 1974: On the short-wave cutoff of CISK. J. Atmos. Sci., 31, pp. 830-833.

Charney, J.G., and M.E. Stern, 1962: On the stability of internal baroclinic jets in a rotating atmosphere. J. Atmos. Sci., 19, pp. 159-172.

Charney, J.G., and A. Eliassen, 1964: On the growth of the hurricane depression. J. Atmos. Sci., 21, pp. 68-75.

Charney, J.G., 1971: Tropical cyclogenesis and the formation of the ITCZ. Lectures in App. Math., American Math. Soc., Providence, R.I., 13, pp. 355-368.

Charney, J.G., 1973: Movable CISK. J. Atmos. Sci., 30, pp. 50-52.

Colton, D.E., 1973: Barotropic scale interactions in the tropical upper troposhere during the northern summer. J. Atmos. Sci, 30, pp.1287-1302

'Forecasting Manual', 1971: Published by India Meteorological Department, Poona-5, India.

Hayashi, Y., 1970: A theory of large-scale equatorial waves generated by condesation heat and accelerating the zonal wind. J. Meteorol. Sco., Japan, 48, pp. 140-160.

Hayashi, Y., 1971: Instability of large-scale equatorial waves with a frequency-dependent CISK parameter. J. Meteor. Soc. Japan, 49,pp.59-62

India Meteorological Department, 1964: Tracks of storms and depressions in the Bay of Bengal and the Arabian sea, 1870-1960.

Israeli, M., and E.S. Sarachik, 1973: Cumulus parameterization and CISK. J. Atmos. Sci., 30, pp.582-589.

Klein, W.D., 1974: Ozone Kinematics and transports in unstable waves. Ph.D. thesis, Dept. Of Meteorology, M.I.T.

Koss, W.J., 1975: Linear stability analysis of CISK induced low latitude disturbances. Paper presented at the ninth technical conference on hurricanes and tropical meteorology, May 27-30, Key Biscayne, Miami, Florida.

Koteswaram,P., 1974: Regional monsoon experiments. Paper presented at the MONEX planning meeting, 28 October- 1 November, Singapore.

Krishnamurti, T.N., 1971: Observational study of the tropical upper tropospheric motion field during the northern hemisphere summer. J. Appl. Meteor., 10, pp. 1066-1096.

Krishnamurti, T.N., M.Kanamitsu, R. Godbole, C.B. Chang, F. Carr and J.H. Chow, 1975: Study of a monsoon depression. Report No. 75-3, Dept. of Meteorology, Florida State University.

Lindzen, R.S., 1974: Wave-CISK in the tropics. J. Atmos. Sci., 31,pp.156-179.

Ramage, C.S., and C.R.V. Raman, 1972: International Indian Ocean Meteorological atlas, vo.2, Upper Air, National Science Foundation, Washingtion, D.C.

Ramanamurty, Bh.V., K.R. Biswas, and B.K.G. Dastidar, 1960: Incidence of 'warm' and 'cold' rain in and around Delhi, and their contributions to season's rainfall, Indian Jour. of Meteor. and Geoph., 11, p.331-346

Ramanna, G.R., 1967: Relationship between depressions of Bay of Bengal and tropical storms of the China sea. Indian Journal of Meteorology and Geophysics., 18, pp. 148-150.

Richtmyer, R.D., and K.W. Morton, 1967: Difference methods for initial-value problems. Interscience publishers.

Saha, K.R., and S.S. Singh, 1972: On the distribution of mean static stability and mean Richardson number in tropical atmosphere. J. Meteor. Soc. Japan, 50, pp. 312-323.

Yamasaki, M., 1969: Large scale disturbances in the conditionally unstable atmosphere in low latitudes. Papers in Meteorology and Geophysics, 20, pp. 289-336.

Yanai, M., S. Esbensen, and J.H. Chu, 1973: Determination of bulk properties of tropical cloud clusters from large-scale heat and moisture budgets. J. Atmos. Sci., 30, pp. 611-627.

BIOGRAPHICAL NOTE

I was born during July, 1944 (precise date of birth is not known), at Mirdha, a small and beautiful village in the Ballia district of Uttar Pradesh, India. Due to the unavailability of a secondary school with science education, I studied economics, geography and Sanskrit in high school. I then received a merit scholarship and studied science. I received the degree of B.Sc. with honors (1962) and M.Sc. (1964) with specialization in exploration geophysics from Banaras Hindu University. After working for a few months at an oil well, I realized that it was not the most suitable place for the academic pursuits in which I was interested.

During 1965, I happened to get a job at the Institute of Tropical Meteorology (Poona). With the help of a glossary of meteorology (to find the meaning of words like barotropic and baroclinic) and available textbooks on meteorology, I started studying meteorology. During 1967, I had the opportunity to visit the National Meteorological Center, Washington; the National Hurricane Research Lab, Miami; the Japanese Meteorological Agency; and other meteorological centers of Japan. In 1968, I attended the NWP symposium in Tokyo. My meeting with Professor J.G. Charney at this symposium inspired me to come to MIT to learn meteorology.

Before coming to MIT in September, 1971, I had published a few papers and done some research in Numerical Weather Prediction which I submitted as my thesis to Banaras Hindu University. In 1972, I was awarded the degree of Doctor of Philosophy by the Department of Geophysics of Banaras Hindu University.

During the four and one-half years at MIT, I spent an academic year in the Geophysical Fluid Dynamics Program at Princeton University, and during the summers of 1973 and 1974, I worked with the stratospheric modelling project at MIT.

During my fruitful stay at MIT, I published a few papers, attended several conferences and meetings, and gave seminars (at Chicago, Harvard, Princeton, Erevan, Singapore, Tallahassee, New Delhi and Poona), but most importantly, I realized that the ultimate purpose of Meteorology, like any other science, should be to serve humanity.

List of Publications (1972-1975)

1. Effect of Arabian Sea-Surface Temperature Anomaly on Indian Summer Monsoon: A Numerical Experiment with GFDL Model. J. Atmos. Sciences, Vol. 32, March, 1975.

2. Computation of Non-Divergent Streamfunctions and Irrotational Velocity Potential from the Observed Winds (J. Shukla and K.R. Saha). Monthly Weather Review, Vol. 102, No. 6, pp. 419-425, 1974.

3. On the Strategy of Combining Coarse and Fine Grid Meshes in Numerical Weather Prediction. (N.A. Phillips and J. Shukla). Journal of Applied Meteorology, Vol. 12, No. 5, pp. 763-770, 1973.

4. Relationships Between Sea-Surface Temperatures, Wind Speeds over the Arabian Sea and Monsoon Rainfall over India (J. Shukla and B.M. Misra) (prepublication).